Investigation of new Ti-based metallic glasses with improved mechanical properties and corrosion resistance for implant applications

Dissertation

zur Erlangung des akademischen Grades

Doktoringenieur (Dr.-Ing.)

vorgelegt

der Fakultät Maschinenwesen

der Technischen Universität Dresden

von

Somayeh Abdi

geboren am 6 September 1980

in Tehran (Iran)

1. Gutachter: Prof. Dr. Ludwig Schultz
2. Gutachter: Prof. Dr. Livio Battezzati

Contents

Abstract

The glass-forming $Ti_{75}Zr_{10}Si_{15}$ alloy is regarded as a potential new material for implant applications due to its composition of non-toxic, biocompatible elements and many interesting mechanical properties. The effects of partial substitution of 15 at.-% Ti by Nb on the microstructure and mechanical behavior of the alloy have been investigated. The limited glass-forming ability (GFA) of the $Ti_{75}Zr_{10}Si_{15}$ alloy results for melt-spun ribbons mainly in nanocomposite structures with β-type nanocrystals being embedded in a glassy matrix. Addition of Nb increases the glass-forming ability. Raising the overheating temperature of the melt prior to melt-spinning from 1923 K to 2053 K yields a higher amorphous phase fraction for both alloys. A decrease of hardness (H), ultimate stress and reduced Young's modulus (E_r) is observed for $Ti_{60}Zr_{10}Nb_{15}Si_{15}$ rods as compared to $Ti_{75}Zr_{10}Si_{15}$ ones. This is attributed to an increase of the fraction of the β-type phase. The melt-spun ribbons show an interesting combination of very high hardness values (H) and moderate reduced elastic modulus values (E_r). This results in comparatively very high H/E_r ratios of >0.075 which suggests these new materials for applications demanding high wear resistance. The corrosion and passivation behavior of these alloys in their homogenized melt-spun states have been investigated in Ringer solution at 37°C in comparison to their cast multiphase crystalline counterparts and to cp-Ti and β-type Ti-40Nb. All tested materials showed very low corrosion rates. Electrochemical and surface analytical studies revealed a high stability of their passive states in a wide potential range. The addition of Nb does not only improve the glass-forming ability and the mechanical properties but also supports a high pitting resistance even at extreme anodic polarization. With regard to the corrosion properties, the Nb-containing nearly single-phase glassy alloy can compete with the β-type Ti-40Nb alloy.

In addition, it has been demonstrated that thermal oxidation could be well applied to $Ti_{75}Zr_{10}Si_{15}$ and $Ti_{60}Zr_{10}Nb_{15}Si_{15}$ melt-spun ribbons. Thermal oxidation treatment is one of the simple and cost-effective surface modification methods to improve the surface characteristics of these alloys. In the first tests, ribbon samples of the ternary and the quaternary alloy which were oxidized at 550°C in synthetic air showed suitable fundamental properties for implant applications, i.e. high hardness, good wettability and hydroxyapatite-forming ability after 10 days. All these properties recommend

the new glass-forming alloys for application as wear- and corrosion-resistant coating materials for implants.

Kurzfassung

Die glasbildende Legierung $Ti_{75}Zr_{10}Si_{15}$ wird wegen ihrer biokompatiblen Zusammensetzung ohne toxische Elemente und auf Grund interessanter mechanischer Eigenschaften als potentielles neues Implantatmaterial betrachtet. Es wurden 15 at.-% Ti durch Nb partiell substituiert und die Effekte auf die Mikrostruktur und die mechanischen Eigenschaften der Legierung untersucht. Auf Grund der eingeschränkten Glasbildungsfähigkeit von $Ti_{75}Zr_{10}Si_{15}$ bestehen die schmelzgeschleuderten Bänder dieser Legierung hauptsächlich aus Nanokomposit-Strukturen mit β-phasigen Nanokristallen in einer glasartigen Matrix. Die Zugabe von Nb steigert die Glasbildungsfähigkeit. Das Anheben der Überhitzungstemperatur der Schmelze vor dem Schmelzschleudern von 1923 auf 2053 K führt für beide Legierungen zu einem höheren Anteil amorpher Phase. Es wird bei der Legierung $Ti_{60}Zr_{10}Nb_{15}Si_{15}$ im Vergleich zur $Ti_{75}Zr_{10}Si_{15}$-Legierung eine Abnahme der Härte (H), Bruchfestigkeit und ein reduzierter E-Modul (E_r) beobachtet. Dies wird mit dem Anstieg des beta-Phasenanteils erklärt. Die schmelzgeschleuderten Bänder zeigen eine interessante Kombination aus sehr hoher Härte und moderaten E-Modul Werten (Er). Dies führt zu vergleichsweise sehr hohen H/E_r-Verhältnissen von >0,075, wodurch diese Materialien für Anwendungen mit hohen Verschleißanforderungen geeignet sind. Das Korrosions- und Passivierungsverhalten dieser Legierungen in ihrem homogenisierten schmelzgeschleuderten Zustand wurde in Ringer-Lösung bei 37°C untersucht und mit dem gegossenen vielphasigen kristallinen Zustand dieser Legierungen sowie mit cpTi und beta-Typ Ti-40Nb verglichen. Alle untersuchten Materialien zeigten sehr niedrige Korrosionsraten. Elektrochemische Studien und Oberflächenanalysen belegen eine hohe Stabilität der Passivfilme in einem weiten Potentialbereich. Die Zugabe von Niob verbessert nicht nur die Glasbildungsfähigkeit und die mechanischen Eigenschaften, sondern erhöht weiterhin die Lochfraßbeständigkeit, selbst bei stark anodischer Polarisation. Bezüglich der Korrosionseigenschaften konkurriert die Nb-haltige fast einphasige glasartige Legierung mit β-phasigem Ti-40Nb. Weiterhin wurde gezeigt, dass an schmelzgeschleuderten Bändern der Legierung $Ti_{75}Zr_{10}Si_{15}$ und $Ti_{60}Zr_{10}Nb_{15}Si_{15}$ eine thermische Oxidation erfolgreich durchgeführt werden konnte. Die thermische Oxidation ist eine der einfachsten und kosteneffektivsten Möglichkeiten der Oberflächenmodifikation um die Eigenschaften der Oberflächen dieser Legierungen zu verbessern. In den ersten Tests zeigten die Bänder-Proben der ternären und der quaternären Legierung, die bei 550°C in synthetischer Luft oxidiert wurden, entsprechende

Eigenschaften für Implantat-Anwendungen, d.h. hohe Härte, gute Benetzbarkeit und die Fähigkeit nach 10 Tagen Hydroxylapatit auf der Oberfläche zu bilden. Alle zuvor genannten Eigenschaften machen diese neuen glasbildenden Legierungen zu geeigneten Materialien für die Anwendung als verschleiß- und korrosionsbeständige Beschichtung für Implantate.

1 Introduction

Titanium (α) and (α+β)- or β-type Ti-based alloys are well-known materials for implant applications due to their relatively low density, superior mechanical properties and good corrosion behavior compared to conventional stainless steel or Co-Cr-based alloys. The spontaneously forming barrier-type oxide film (mainly TiO_2) at the surface of these materials insulates the inner material from the external environment, resulting in high corrosion resistance [1,2].

Nevertheless, there are still some significant problems with the biomechanical compatibility of conventional Ti-based materials arising from their high stiffness and the concomitant mismatch between Young's modulus values of bone (E = 10-30 GPa) and the implant material (E = 110-120 GPa for cp-Ti and Ti-6Al-4V). These results in stress shielding effects causing implant loosening with the consequence of re-surgery [3,4]. Another major problem is the limited strength and hardness of these alloys, which can cause implant fracture. Limited wear resistance can also create an incidence of allergy and inflammatory cascades because of a release of particles and/or toxic metallic ions [1,3,5]. Consequently, the development of new materials with improved properties, i.e. lower Young's modulus, higher strength and hardness combined with excellent corrosion resistance and cell biological compatibility is an urgent, but challenging demand. In this regard, a new generation of cast low modulus β-type Ti-based alloys, such as Ti-(40-45)Nb is in the focus of fundamental studies. They exhibit very high corrosion resistance explained by a significant fraction of Nb oxides in the spontaneously forming passive film [6,7]. However, their limited strength causes the need for complex thermo-mechanical post-processing [6].

Recently, Ti-based metallic glass-forming alloys are also attracting increasing interest as potential biomaterials as they exhibit superior mechanical properties relative to their crystalline counterparts and to conventional Ti-based materials such as very high strength, relatively low Young's modulus values, low density and higher wear resistance [8-11]. These very promising mechanical performance data result from the lack of long-range order and the simultaneous absence of microstructural defects such as grain boundaries and dislocations in the single-phase material [12-14].

However, up to date, most of the Ti-based alloys with bulk glass-forming ability contain cytotoxic or allergic elements such as Al, Be, Cu and/or Ni which could be released as ions or metal particles from metal implants into the body tissue and restrict the biomedical application of these alloys

[15,16]. This release could take place through processes such as corrosion (stress corrosion, fatigue corrosion) or wear [5]. Therefore, not only the life-time of an implant depends on the corrosion resistance of the metallic material but also the corrosion products releasing to the surrounding tissues may result in biocompatibility problems, i.e. affect cell metabolism [17-19]. Consequently, with regard to corrosion stability and related metal ion release, the use of non-toxic elements which support stable passivity must have priority in the development of new glass-forming biomaterials. The aim of this work was to develop new glass-forming Ti-Zr-(Nb)-Si alloys which are completely free of cytotoxic elements. These alloys are considered to have a promising potential for implant applications. The study has been started by exploring the Ti-Zr-Si system and to analyze the effect of substitution of up to 15 at.-% Ti by Nb leading to the development of $Ti_{75}Zr_{10}Si_{15}$ and $Ti_{60}Zr_{10}Nb_{15}Si_{15}$ alloys and detailed investigations regarding microstructural and mechanical aspects have been done. In addition, corrosion properties have been explored in comparison to other potential implant materials, i.e. single phase α-Ti or β-Ti-40Nb as it is essential for long-term use in the human body.

The oxide film on the surface of Ti and its alloys (mainly TiO_2) are defined as bioinert and, therefore, a Ti-based surface cannot easily bond to bone tissue. A consequence may be loosening of the implant after long-term resorption of bone tissue. Therefore, surface modifications are applied to improve the bone-bonding capability by inducing bioactivity while preserving the properties of the bulk material. In this study, thermal oxidation has been applied as a surface modification method in order to improve the bone cell growth. Finally, a SBF (simulated body fluid) test has been performed to evaluate the effectiveness of our modification method. This test assesses the ability to form bone-like hydroxyapatite on the nearly glassy melt-spun alloy surfaces.

2 Theoretical background

2.1 Bulk metallic glasses (BMGs)

Despite of crystalline alloys in which constituent atoms are posed in a regular and periodic arrangement in three dimensions (long-range order), metallic glasses possess only atomic medium range and short range order (lack of any long-range order). They are formed by continuous cooling from the melt which must be rapid enough to freeze the liquid state. When a liquid is above the melting temperature, it is in an equilibrium state. By cooling the liquid, it will crystallize if the required atomic mobility (diffusion) and hence, a certain necessary time window is provided. When the cooling rate is very high (10^2-10^4 K/s for BMGs), the atoms cannot arrange into the most stable equilibrium configuration (crystal), the liquid will be retained in a supercooled condition which deviates from the equilibrium. If the temperature is further decreased, the supercooled or undercooled liquid is frozen-in and a glass is formed [20]. The temperature at which the liquid becomes homogeneously frozen is the so-called glass transition temperature T_g.

Metallic glasses are in a metastable non-equilibrium state. In Fig. 2.1, schematic Gibbs free energy (G) in dependence of the arrangement of atoms in a considered system is shown. The energy curve has two minima. The absolute minimum is described by G minimal and $\Delta G = 0$. It corresponds to a system with the lowest energy and, therefore the most stable energetic state called equilibrium state. A perfect crystal of a solid material represents it. The second minimum is a local minimum and at higher level of energy than the absolute minimum. At this point G is not minimal, but $\Delta G = 0$. This state, which has certain stability, is not the most stable state and is, therefore, named metastable equilibrium state. An undercooled liquid state denotes this minimum.

Metallic glasses are in non-equilibrium state close to metastable equilibrium with certain higher energy due to the free volume formation which is frozen into the amorphous solid state during quenching of the liquid. Consequently, the glassy state is not stable and has a tendency for structural relaxation over a certain time period as a trend to release free volume and to transfer into the metastable undercooled liquid state. This process is too slow at room temperature but by applying a thermal treatment for some minutes or even seconds it can be achieved (e.g. heating up to T_g, see section 2.1.4).
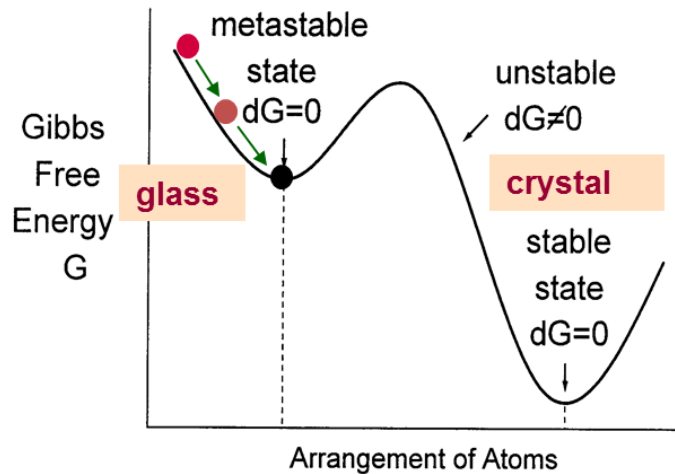
Figure 2.1: Schematic representation of the Gibbs free energy in dependence of the atomic arrangement of a considered system.

Crystallization of a glassy system takes place by transfer from a (non-equilibrium) metastable state into a lower energetic stable equilibrium crystalline state via overcoming the activation barrier (G maximum; unstable state; Fig. 2.1) e.g. by heating the system.

2.1.1 Structure of metallic glasses

Metallic glasses exhibit different atomic configurations as compared to crystalline solids. Despite of crystals in which constituent atoms are arranged in a periodic manner (long-range translational periodicity), their atomic arrangement is not in a periodic order (no long-range order) but represent only local ordering. They contain short- to medium-range structural order as the atoms interchange to establish configurations with the lowest energy. Short range order (SRO) develops above the first couple of coordination shells (typically <0.5 nm) while medium range order (MRO) refers to over-next neighbor arrangements and may extend to beyond ~1nm [21,22]. For a monolithic glass, properties such as initiation of plastic flow are considered to be controlled by SRO and MRO states [22].

In the early structure models, arrangements of atoms were described by Bernal [23] as dense random packing of spheres mainly for binary metal-metal alloys. Later, Gaskell [24] developed a model based on trigonal prism units for rebuilding the structure of amorphous metal-metalloid alloys. These models were not able to explain SRO and MRO besides the effect of the large atomic size difference required for metallic glasses. In the present more complex models, a cluster-packed structure is considered and solute-centered clusters are representative structural elements such as the ones proposed by Miracle [21,25] and Sheng [26].
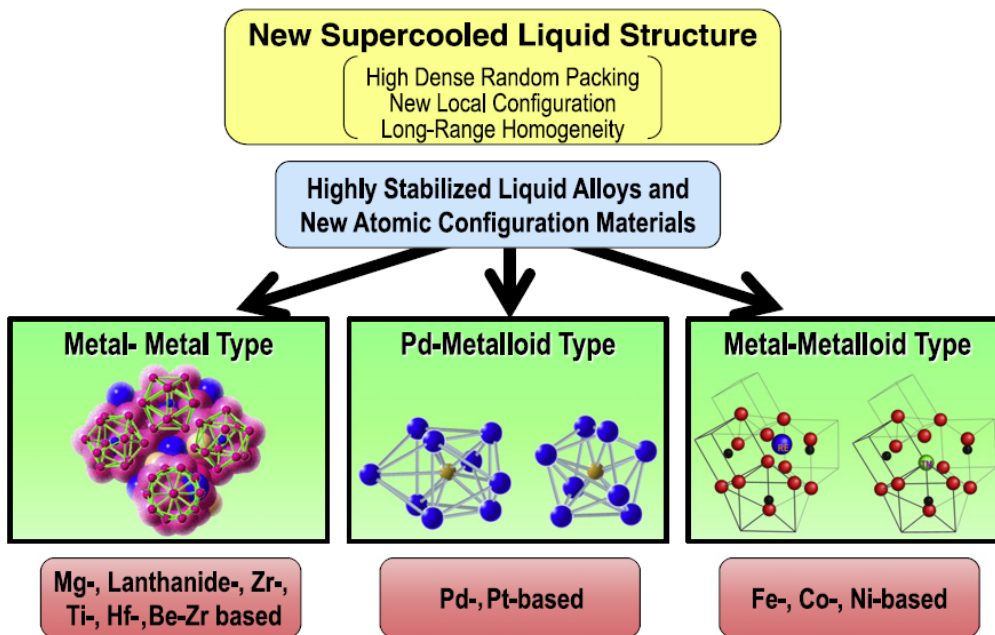
Figure 2.2: Schematic illustrations of the structural features metal-metal, Pd-metalloid and metal-metalloid types of glassy alloys [12].

Another classification of atomic configurations has been proposed by Inoue et al. [12], categorized as metal-metal-type, Pd-transition metal-metalloid-type and metal-metalloid type (shown in Fig. 2.2). Metal-metal type includes Zr-, Ti-, Hf-, Mg- based alloy systems which exhibit atomic configurations with icosahedral-like order. The glassy structure of Pd-metalloid type such as Pd- or Pt- based alloy systems is composed of highly dense packed arrangements of two types of polyhedral of Pd-Cu-P and Pd-Ni-P atomic pairs. The metal-metalloid-type comprises Fe-, Co-, Ni- based systems having network-like atomic configurations which consist of trigonal prisms. These proposed structures can well suppress the long-range order of the constituent elements and prevent the crystallization reaction. From a structural point of view, although a complete agreement on the type of packing is still one of the main remaining challenges, present models can support the clarification of unusual properties observed for metallic glasses.

2.1.2 Glass forming ability

Glass forming ability (GFA) defines the ability of a metallic alloy to transform into the glassy state during undercooling of its melt. The more the undercooled liquid is stabilized against crystallization, the higher is the GFA of the system. Key parameters to understand this concept are thermodynamic and kinetic aspects as well as structural effects which will be briefly discussed in the following. Furthermore, some common GFA criteria reported in the literature are named [20].

- Thermodynamics aspects: The thermodynamic stability of a system is determined by its Gibbs free energy. In order to increase the stability of a glass, the thermodynamic driving force for crystallization ΔG must be low which is defined as: $\Delta G = \Delta H_f - T\Delta S_f$, where ΔH_f is the enthalpy of fusion and ΔS_f is the entropy of fusion. This ΔG is in principle the energy difference between the higher energetic undercooled liquid state (non-equilibrium) and that of the corresponding crystalline state at certain temperature $T<T_m$. To obtain a low ΔG, the alloy melt should have a low enthalpy and high entropy. A low ΔH_f is achieved for systems with low melting temperature such as for alloys with a deep eutectic, i.e. alloys which exhibit an eutectic temperature significantly lower than the melting temperatures of the individual components. Compositions at and close to deep eutectics are therefore suited for glass-formation. ΔS_f is higher for alloy systems with a large number of components.

- Kinetic aspects: Glass formation is achieved, if the liquid could be cooled fast enough to suppress the formation of a crystalline phase. Hence, the problem of glass formation is under this consideration mainly of kinetic nature. Turnbull [27] expressed the kinetics of crystallization by the following equation:

$$I(T) = \frac{K}{\eta(T)} \; e^{-\frac{b\alpha^3\beta}{T_r(\Delta T_r)^2}} \qquad \text{(Eq. 2.1)}$$

in which, I(T) states the homogeneous nucleation rate of crystalline nuclei formation. The lower I(T), the higher is the glass forming ability. In Eq. 2.1, K is a kinetic constant, $\eta(T)$ is the viscosity of the undercooled liquid, b is a shape factor (= $16\pi/3$ for a spherical nucleus), $T_r = T/T_m$ refers to the reduced temperature, $\Delta T_r = 1-T_r$ is the reduced undercooling (or supercooling) and α and β are dimensionless parameters related to the liquid-solid interfacial energy (σ) and to the molar entropy of fusion (ΔS_f), respectively [20]. As it can be derived from eq. 2.1, the viscosity $\eta(T)$ is the kinetic parameter which influences the glass formation ability. The higher the viscosity of the undercooled liquid, the lower is the nucleation rate and, as a consequence, the higher is the GFA. $\alpha^3\beta$ is a

thermodynamic term. When it increases (increase in σ and ΔS_f and/or decrease in ΔH_f) the nucleation rate decreases sharply.

Another kinetic criterion is the critical cooling rate R_c, which represents the cooling rate above which glass formation occurs during solidification of the liquid. Constructing time-temperature-transformation (T-T-T) or continuous-cooling-transformation (C-C-T) diagrams is the best way to determine R_c experimentally. The T-T-T diagrams are computed by calculation of the time needed for the liquid-to-solid transformation at each temperature (isothermally), while (C-C-T) diagrams refer to continuously reducing the melt temperature down to room temperature. There is a slight difference between these two with regard to both the transformations temperatures and times. A schematic (C-C-T) diagram is shown in Fig. 2.3. The transformation curve has a nose-shape. If a liquid is cooled very slowly, solidification will take a long time and a crystalline solid will be produced. Curve "1" represents a little faster solidification at T_1 and t_1, but the product is still a crystalline solid. If the liquid alloy is solidified faster than the cooling rate represented by curve "2", crystallization will not occur. The nose of the diagram exhibits the shortest time needed for the formation of a crystalline phase and the critical cooling rate is calculated from the nose coordinates:

$$R_c \approx \frac{T_l - T_n}{t_n}$$

(Eq. 2.2)

So if the liquid alloy is cooled at a rate faster than R_c (curve "2"), it will be retained in the supercooled condition and, by further decreasing the temperature below T_g, a glass phase forms.
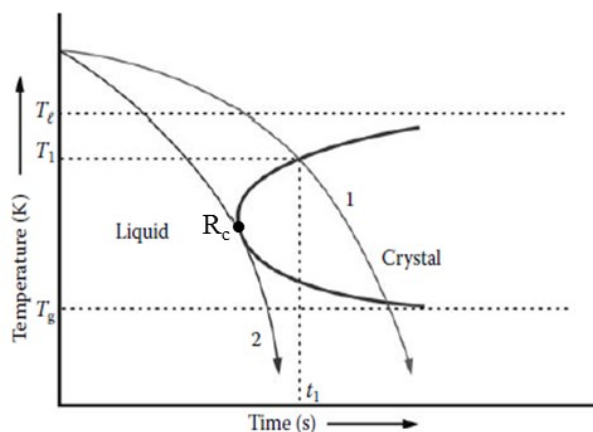

Figure 2.3: Schematic C-C-T diagram for a hypothetical alloy system [20].

The value of the critical cooling rate for glass formation R_c differs for different alloy systems and different compositions. Besides, different melt-metallurgical methods provide

different cooling rates. The solidification rates achieved by rapid quenching techniques such as melt-spinning are about 10^4-10^8 K/sec. In the melt-spinning process, the melt ejected through an orifice is solidified on a chill (substrate) to produce fine fibers. The wheel is used to extract the heat from the ribbon as quickly as possible. The ribbons have typical dimensions of 2-5 mm in width and 20-50 μm in thickness. A slow cooling process such as Cu mold casting provides cooling rates in the range of 10^3 to1 K/sec. This is used to produce bulk metallic glasses. In this method the molten alloy is poured into a copper mold which conducts the heat rapidly and the steep temperature gradients result in solidification. Molds with different internal diameters can be used which produce samples with different diameters [20].

• Structural aspects: Atomic size mismatch of the constituent atoms over certain values was the first structure-based criterion of GFA. In 1967, Mader et al. [28] found that a critical radius difference of ~15% is necessary to allow glass formation. This difference prevents an atomic rearrangement to form an ordered crystalline structure. Egami et al. [29,30] developed another concept in which the ratio of solvent and solute radii plays the critical role. In their theory, size differences between solute and solvent elements generate local atomic strains. When this local stress attains a critical level (beyond critical solute concentration) the solvent lattice becomes topologically instable and a glassy alloy is more favorable than the corresponding crystalline one. Miracle et al. [31] modified Egami's model and provided new analyses to predict density and packing fraction by the efficient cluster packing model. The idea is to provide rules which lead to a densely packed melt preventing structural rearrangement during cooling.

• Empirical rules: Considering all the above mentioned aspects, Inoue et al. [20] have formulated three basic empirical rules for BMG formation, the so-called "Inoue rules":
(i) the alloy must contain at least three components or more to increase the complexity and size of the crystal unit cell and to avoid favorability of a crystalline phase, (ii) an atomic size difference ~12% among the main constituent elements must exist and (iii) heats of mixing among the three main constituent elements should be negative.

• GFA criteria: Several criteria have been proposed, considering different aspects of the GFA, to predict the ability of glass formation of alloy systems. As discussed above, the critical cooling rate R_c is an effective indicator of the GFA. Two of the early criteria were the reduced glass transition temperature T_{rg} and the supercooled liquid region ΔT_x, which are designated as $T_{rg} = T_g/T_l$ and $\Delta T_x = T_x-T_g$, where T_g , T_l and T_x are the glass transition

temperature, the liquidus temperature and the onset of crystallization temperature, respectively. Turnbull [27] proposed T_{rg} as a good criterion of the GFA based on kinetics aspects. The higher the value of T_{rg}, the higher is the GFA. The reported values of T_{rg} for many metallic glasses are between 0.4-0.7 [20]. Inoue [20] has proposed the supercooled liquid region as an indicator of the GFA. The larger ΔT_x, the higher is the GFA. By finding some exceptions to this criterion, it was suggested that ΔT_x is only suitable to evaluate the thermal stability of the supercooled liquid. Later, Lu and Liu [32] have proposed a new criterion which involves both the glass formation conditions and the thermal stability of the glass, the so-called γ-parameter, which was defined as $\gamma = T_x/ T_g + T_l$. This parameter can be determined by one single Differential Scanning Calorimetry (DSC) measurement (see section 2.1.4).

2.1.3 Metallic glass matrix composites

In recent years, there has been a lot of interest and activity on synthesizing and characterizing glass-matrix composites as they exhibit enhanced plasticity in comparison with monolithic metallic glasses. The second phase in these composites is a crystalline phase, and due to its fraction and (grain) size, it introduces different properties into the system. They have been designated as *in situ* or *ex situ* composites depending on how they are obtained. Figure 2.4 demonstrates a schematic in which BMG composites are categorized [33].

- <u>In situ composites:</u> In these composites, the second phase precipitates from the melt during solidification. They are produced either when the glass-forming ability of an alloy system is not high enough to form a fully glassy state or by tentatively choosing an alloy composition far from the actual glass-forming composition. The participating crystalline phases will not be homogeneously distributed in the matrix phase but will show a gradient in their distribution corresponding to the cooling rate gradients in the bulk sample.
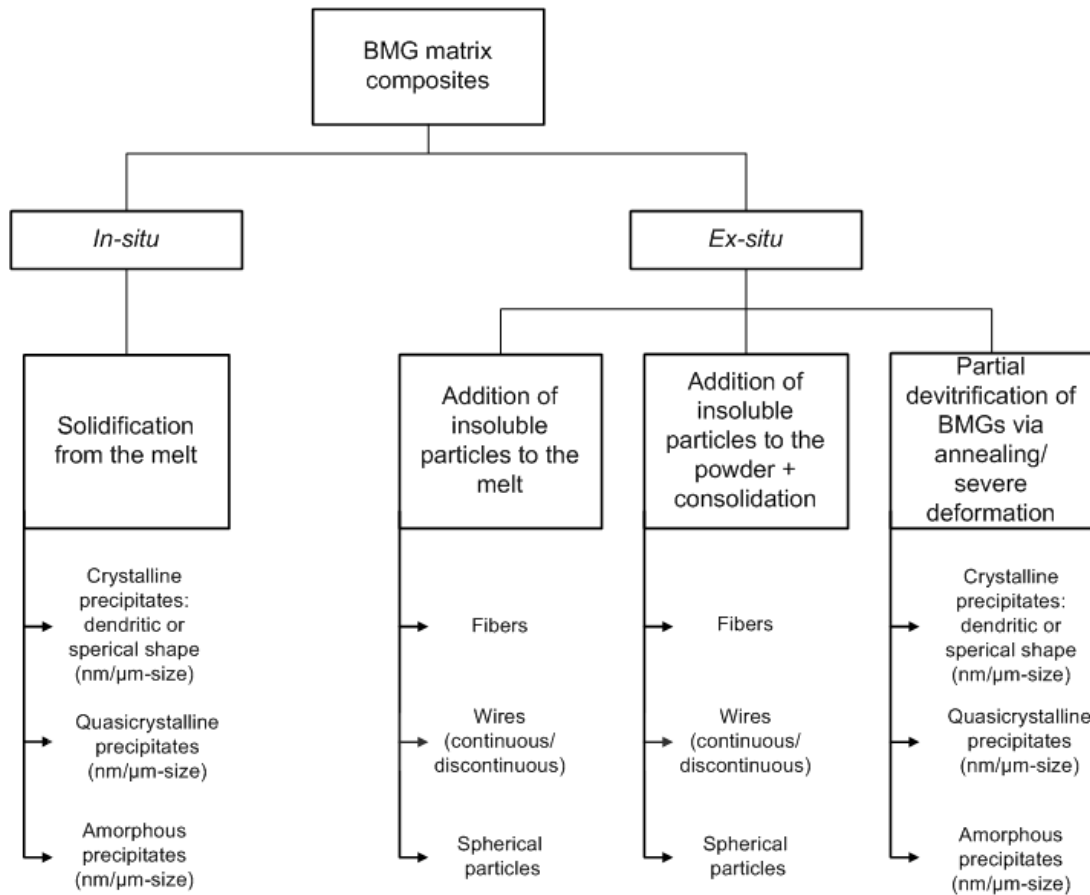
Figure 2.4: Schematic illustration of the different process routs for BMG composites [33].

Kühn et al. [34] demonstrated that by coupling the glassy phase with an in situ formed ductile dendritic bcc β-Zr/Ti-type phase for a Ti-based and a Zr-based alloy excellent mechanical properties for both alloys can be achieved.

- Ex situ composites: These composites are produced by adding a reinforcement phase separately during the casting or powder metallurgical processing of the alloy. Choi-Yim et al. [35] reinforced the Zr57Nb5Al10Cu15.4Ni12.6 bulk metallic glass forming liquid with up to 50 Volume-percent (% V-f) Ta, Nb, or Mo particles. This resulted in increasing compressive strain-to-failure values up to a factor of 12. In these alloys, the interaction between matrix and crystalline phase (interphase bonding) is much weaker than that of the in situ composites.

The other way is subsequent processing of the glassy as-cast alloy such as annealing. In this case, the microstructure can be controlled, i.e. by annealing at low temperature a nanocrystalline phase might be formed in the glassy matrix.

Metallic glass composites exhibit often better mechanical properties than metallic glasses, as they combine the high strength of the glass matrix with the ductility of the second phase. But from the aspect of corrosion behavior, which is very important in a case where they are intended for biomedical or decorative applications, such microstructures can be challenging. The presence of heterogeneities in the glass-matrix can act as nucleation sites for pit initiation and reduce the corrosion resistance of the alloy [36].

2.1.4 Thermal behavior of glassy alloys

Metallic glasses exhibit a characteristic thermal behavior upon heating. *Differential Scanning Calorimetry (DSC)* is the most commonly used method to study thermal transitions (technical details are described in section 3.2). It is conducted under inert atmosphere to identify phase transitions and reactions. In Fig. 2.5 the DSC curve of glassy $Zr_{55}Al_{10}Cu_{30}Ni_5$ can be seen reflecting the typical thermal features of an alloy with bulk glass-forming ability. The analysis of the exothermic/endothermic heat flow during heating with a constant rate leads to a determination of thermal characteristics such as transition temperatures (melting/boiling points; not shown in Fig. 2.5) and crystallization temperature. The appearance of different consecutive phenomena depends on different parameters, i.e. heating/cooling rate, purity level of the material. These phenomena are:

- Structural relaxation: By increasing the temperature a moderate change of metallic glass properties is usually observed at short times as an exothermic transition (heat is released), the so-called structural relaxation. It is particularly visible for rapidly cooled samples. Through structural relaxation the metallic glass slowly transforms towards a more stable or ideal glass of lower energy (annihilation of free volume).

- Glass transition temperature T_g: It is a characteristic temperature considered as onset temperature of an endothermic (heat is absorbed) event at which the relaxed glass will transform into an undercooled melt. Accurate determination of T_g can be done after a complete pre-relaxation of the sample.

- Crystallization temperature T_x: On further heating the undercooled liquid may directly transform into a crystalline phase. The onset temperature is called T_x and the crystallization is marked by an exothermic event. If sequential crystallization occurs, several exothermic peaks may be present, although, even a single peak might be attributed to the formation of more than one crystalline phase.

- Undercooled liquid region ΔTx: It is related to the temperature range between Tg and Tx, in which the undercooled liquid state is present. As mentioned in section 2.1.2, ΔTx is a criterion of GFA. The larger the ΔTx, the higher is the resistance to crystallization and, as a consequence, the more improved is the GFA of the system.
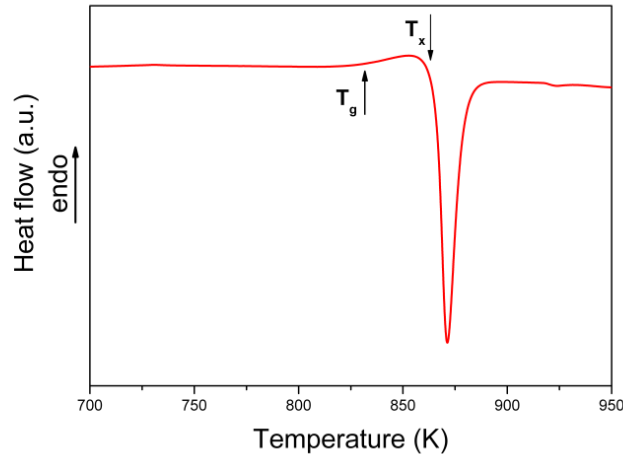

Figure 2.5: Typical DSC curve of a metallic glass alloy

Information obtained from heat treatment measurements can be used to find the methodology to obtain a glass with nanocrystals dispersed throughout, an ultrafine grained composite, or a completely crystalline material of different grain sizes by controlling the time and the temperature of the annealing treatment.

2.1.4.1 Thermal behavior in oxidative atmosphere

If a thermal treatment is carried out under air atmosphere, oxidation will occur besides crystallization by increasing the temperature. Therefore, two different changes can occur at the bulk as well as the surface of the sample. By increasing the temperature the metal-based phase can change and go through phase transitions while on the surface of the material chemical reactions of the metallic constituents with oxygen (from the environment) can take place. The metal-base changes are not related with a mass change and only consist of a reordering of the metal atoms. On the other hand, the chemical reactions on the surface are associated with a mass change (mass gain) due to the solid oxide formation.

A typical technique that can be used for analyzing temperature-dependent mass change is thermogravimetry TG (technical details in section 3.6). This procedure may be combined with

DSC to investigate the oxidation behavior of materials at high temperatures. Recently, the oxidation behavior of some Zr-based metallic glasses has been studied by Lim et al. [37].
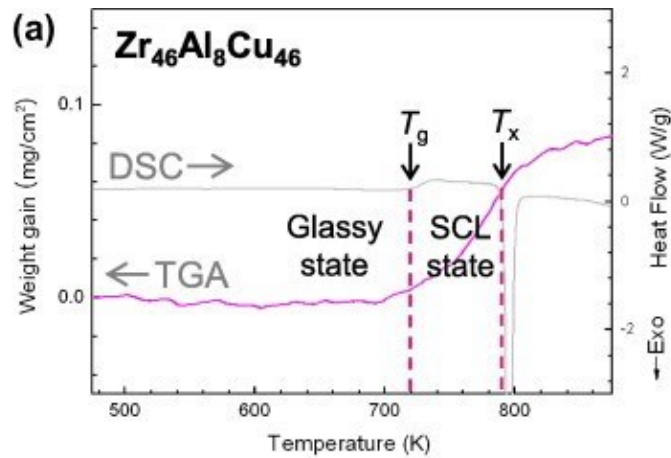

Figure 2.6: Temperature-weight gain plot of melt-spun $Zr_{46}Al_8Cu_{46}$ [37].

They have superimposed TG curves of samples to their DSC curves as shown in Fig. 2.6 in order to investigate the thermal stability and the oxidation resistance of alloy systems before T_g, in the supercooled liquid region and after T_x in detail.

Both DSC and TG measurements with constant heating rate are often combined with annealing studies, i.e. heating to a selected temperature and keeping the temperature constant (isothermal) to analyze phase reactions in a time resolved mode.

2.1.5 Mechanical properties of metallic glasses (at room temperature)

Mechanical properties of materials have great importance due to their role for applications. Therefore, their characterization has been critical to the exploitation of these materials. Metallic glasses are considered to have superior mechanical properties, higher strength (in the order of 1800 to 2500 MPa) and lower Young's modulus values (in the order of 80 to 100 GPa) in comparison with their crystalline counterparts [12]. However, their main drawback is their lack of macroscopic plasticity at room temperature. Different to crystalline alloys in which deformation occurs through slip systems and dislocation modes, in case of metallic glasses deformation takes place due to the formation of shear bands and their propagation. When applying further strain, a sudden fracture of the sample occurs. This deformation at low temperatures (lower than about 0.5 T_g) and low strain rates is an inhomogeneous deformation. It has been shown that an increase in strain makes the metallic glasses softer, allows them to

13

be deformed at lower stresses and as a consequence of this strain softening, shear band formation or shear localization occurs [20,38].

Inhomogeneous deformation is mostly concentrated in a few very thin shear bands that form on the planes of maximum resolved shear stress which are tending close to 45° to the loading axis [20].

There are two hypotheses for the mechanism of inhomogeneous deformation. The first one is the "free-volume model" [39], which states that during deformation the viscosity in shear bands decreases as free volume creation takes place. Decrease of viscosity results in a reduction of the resistance to deformation. According to the second hypothesis, local adiabatic heating occurs in shear bands, which leads to a decrease in the viscosity and a considerable rise of the temperature in shear bands [40].
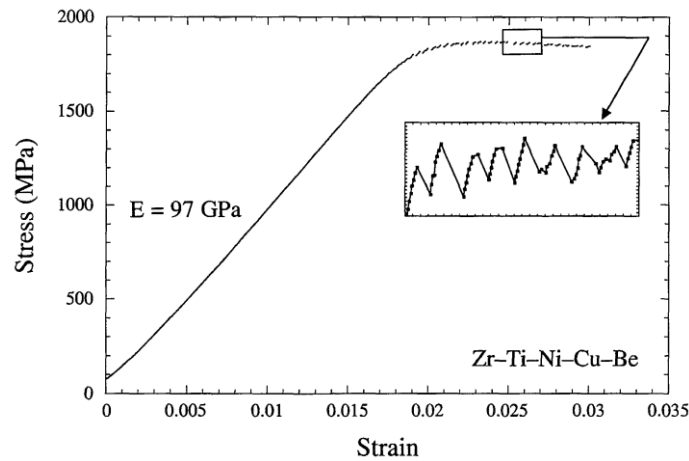

Figure 2.7: Compressive stress-strain curve for $Zr_{40}Ti_{14}Ni_{10}Cu_{12}Be_{24}$ BMG alloy tested at a strain rate of $1 * 10^{-4}$ s^{-1} [41].

Figure 2.7 shows the compressive stress-strain curve for a $Zr_{40}Ti_{14}Ni_{10}Cu_{12}Be_{24}$ BMG alloy [41]. As it can be seen the sample loads elastically to the yield stress and, at that point, serrated plastic flow begins. By shear band forming and propagation, a sudden load drop is noticed which is followed by an elastic recovering of the surrounding material. The repeating cycles of these events result in a serrated flow. Wright et al. [41] have studied the serrated flow to better understand deformation. They found that the free volume theory of deformation gives the primary cause of flow localization in metallic glasses and not the local adiabatic heating although significant heating is predicted for the final failure event. On the other hand, Yang et al. [42] state that a sudden temperature rise within a shear band (local adiabatic heating) causes the failure of bulk metallic glasses. At the fracture strength, it is shown that the shear band

temperature is very close to T_g for a number of BMG systems and reveals the fact that the catastrophic failure of BMG is caused by the sudden drop in viscosity inside the shear band at T_g. In addition, Guo et al. [43] show that a large amount of heat generated will necessarily transfer from the shear band into the surrounding matrix, resulting in the formation of a heat-affected zone (HAZ). Their HRTEM studies reveal that structural disorders and rearrangements on the scale of a few nanometers occur around the shear bands.

A strategy for enhancing the plasticity of metallic glasses is the development of in situ composites (see section 2.1.3). In metallic glass composites, a second phase is introduced to the glassy matrix to promote shear band initiation (to distribute the plastic strain more broadly to avoid the catastrophic localization) and to delay shear band propagation. The deformation behavior of in situ composites mainly depends on the volume fraction of the crystalline phase and their nature, size and shape [20].

Besides composite formation, mechanical pre-treatments can also be applied effectively to improve the plastic deformation of a metallic glass. Scudino et al. [44] investigate the effect of cold rolling on mechanical properties of the $Zr_{52.5}Ti_5Cu_{18}Ni_{14.5}Al_{10}$ bulk metallic glass. The results reveal that it is possible to improve the room temperature plastic strain of the glass by inducing a small plastic deformation. It is suggested that cold rolling introduces a heterogeneous microstructure consisting of hard and soft regions and, as shear band formation and propagation preferably occurs at the soft regions, the hard regions may prevent shear band propagation.

2.1.6 Corrosion behavior of metallic glasses

The study of the corrosion behavior of metallic glasses is of great importance to understand their chemical and environmental stability. Corrosion processes in humid environment are mostly based on electrochemical reactions. First of all, the corrosion rate of multicomponent glass-forming alloys is determined by the electrochemical reactivity of the main alloying elements. Nevertheless, in more detail, aspects of thermodynamic metastability, unusual atomic structure and chemical homogeneity due to the ideally single-phase nature are decisive as well.

Structure and metastability: It has been often stated that metallic glasses exhibit a higher corrosion resistance than their crystalline counterparts due to their homogeneous, single-phase glassy nature [45,46]. Multiphase structures in crystalline materials, besides crystal defects such as grain boundaries, dislocations and second-phase precipitates are associated with

galvanic effects which can result in the initiation of localized corrosion. However, it is believed that the general corrosion kinetics of metallic glasses is affected in a similar way as for crystalline alloys by their ability for passive film formation.

To investigate the corrosion behavior, we need first to understand the formal basis that can be described in terms of the mixed potential theory [47] which holds only for "open circuit conditions". The theory consists of two simple hypotheses: (1) any electrochemical reaction can be divided into two or more partial oxidation and reduction reactions and (2) the total rate of oxidation must equal the total rate of reduction.
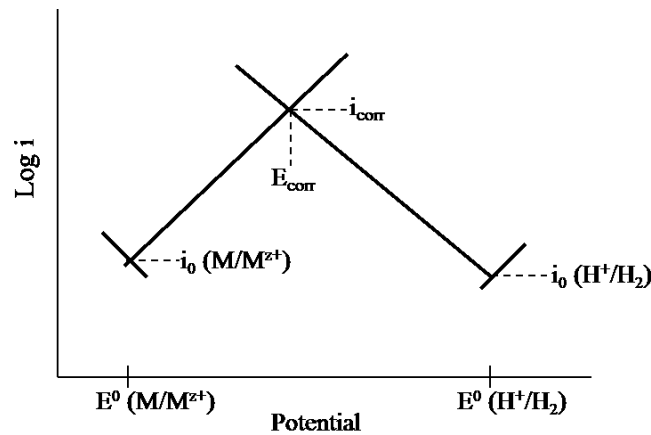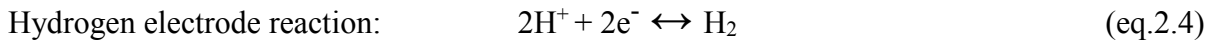

Figure 2.8: Schematic i-E curves for partial reactions of the charge transfer type for an unnoble metal in an acid electrolyte (quasi-static conditions).

For example, for a case of an unnoble metal, M, in an acid electrolyte, the schematic of this theory is shown in Fig. 2.8. The oxidation and reduction reactions are considered as follows:

Metal electrode reaction: $\qquad M \leftrightarrow M^{n+} + ne^-$ $\qquad$ (eq.2.3)

Hydrogen electrode reaction: $\qquad 2H^+ + 2e^- \leftrightarrow H_2$ $\qquad$ (eq.2.4)

the reaction will be expressed as $M + 2H^+ \rightarrow M^{2+} + H_2$. The corresponding equilibrium potentials are $E_{eq,M}$ and $E_{eq,H2}$ at which the rate of each half cell reactions at metal electrode and hydrogen electrode are equal, namely the exchange current density of metal $i_{o,M}$ and the exchange current density of hydrogen $i_{o,H2,}$ respectively. At a considered electrode surface, hydrogen reduction and metal oxidation partial reactions will occur "delocalized". In total, a mixed potential state, the corrosion potential E_{corr} will establish itself in between $E_{eq,M}$ and $E_{eq,H2}$. The metal oxidation rate will exceed the metal reduction rate and the hydrogen reduction rate will surpass its oxidation rate. Considering the second hypothesis, the potential E_{corr} will

be the potential at the intersection of partial oxidation and reduction branches, where the rate of metal oxidation and hydrogen reduction are equal, this is defined as $i_{corr} = i_{anodic} = i_{cathodic}$. When the potential of the metal is shifted by an overpotential (η) and the anodic reaction is promoted, an activated dissolution will take place and the rate of dissolution reaction is given by the Tafel law:

$$i_{anodic} = i_0 \cdot exp\frac{\beta.z.F.\eta}{R.T} \qquad (eq.2.5)$$

i_o is the exchange current density, β is the symmetry factor, z is the valence of the metal ion, F represents the Faraday constant and η is the overpotential. It can be seen that the dissolution rate (i_{anodic}) is a function of the exchange current density which itself is described as [47]:

$$i_0 = z \cdot F \cdot \left(\frac{KT}{h}\right) \cdot \left(\frac{\alpha Ns}{NA}\right) \cdot exp\left(-\frac{\Delta G^*}{RT}\right) \qquad (eq.2.6)$$

which includes the frequency factor $(\frac{KT}{h})$, α is the fraction of the total number of surface atoms considered to be electrochemically active sites for removal during the dissolution, N_s is the number of atoms per unit area of surface, N_A is Avogadro's number and ΔG^* is the electrochemical free energy of activation [47].

It can be concluded from the above descriptions that the dissolution rate can be affected by many factors. The reactivity of metallic glasses and their crystalline counterparts can be compared considering the above parameters. The factor α is a function of the crystallographic orientation, the dislocation density and the grain size. It may be considered to be much higher for a crystalline alloy state. ΔG^* may be lower for the glassy alloy state with the same composition [47]. As described in section 2.1, glasses are in a metastable state and as a consequence, their surface atoms are at higher energy levels (nonequilibrium configurations) than the surface atoms of crystalline states. As a result, glassy alloys can have a lower free energy of activation than their crystalline counterparts.

Chemical composition: To investigate the parameters affecting the corrosion rate, cathodic kinetics as well as anodic kinetics has to be considered. Although the cathodic kinetics may be affected by structure factors in the same way as the anodic kinetics, which is described above, the presence of metalloid elements (B, P, Si, C, etc.) in the composition of many alloy systems is more significant. For example, the exchange current density for the hydrogen reaction on metalloid surfaces ($\sim 10^{-13}$ A/cm^2) is much smaller than that on noble metal or transition metal surfaces ($\sim 10^{-3}$-10^{-6} A/cm^2), which can result in an increase of the corrosion resistance of glassy alloys with high fractions of a metalloid in their composition [47].

Homogeneity: It is assumed that due to their single phase nature metallic glasses exhibit high chemical homogeneity and therefore, superior corrosion resistance. However, in commercial production of BMGs, the presence of heterogeneities cannot be completely avoided. Some examples include gas pockets formed by an entrapment of gas bubbles during production [48], small crystallites formed due to the presence of oxygen in the melt [49], or a gradient of medium range order (MRO) in the cross-section of a rod sample [50] or phase separation [51]. Furthermore, during application of devices made from BMGs under high mechanical load defects like shear bands can be created. In particular for Zr-based bulk metallic glasses, it is meanwhile quite comprehensively demonstrated, that those defects in the as cast and processed samples are very critical for the initiation of local corrosion [52,53].

2.1.5.1 Corrosion behavior of the component elements

An investigation of the corrosion behavior of the constituent elements of an alloy may be a good assistance for approximately predicting the corrosion of the alloy. In this regard, Pourbaix diagrams are considered as beneficial tools [54]. These diagrams are based on the equilibrium potentials of the electrochemical reactions of a considered Me-H_2O system which are calculated from thermodynamic relations as a function of the pH value by means of the Nernst equation. They can be used to estimate the corrosion behavior of metals in aqueous solutions, but these diagrams are just based on thermodynamic equilibrium data. Although valuable information on the stability range of different metal species relative to the stability range of water can be extracted, kinetics data are necessary to make a ccomprehensive conclusion on the rate of corrosion reactions.

Ti: Figure 2.9 shows the Pourbaix diagram for the system Ti-H_2O at 25°C, considering the oxides Ti_2O_3 and TiO_2 in the anhydrous state. The diagram exhibits the thermodynamic stability of titanium and the derivatives, which can exist in the presence of water. But it cannot represent exactly the equilibrium conditions of the system in the regions marked with question marks. Obviously, Ti is not a noble metal as its thermodynamic stability domain does not have any portion in common with that of water.

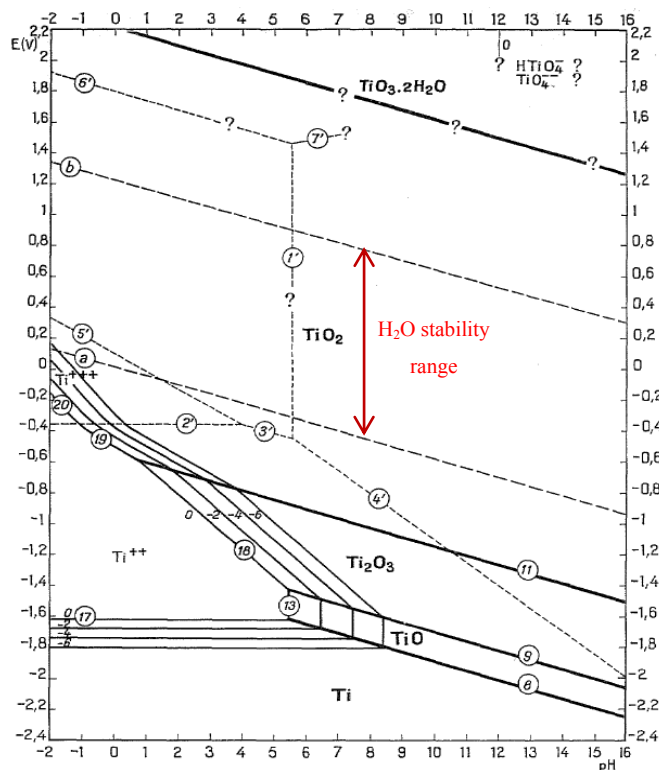Figure 2.9: Potential-pH equilibrium diagram for the system Ti-H$_2$O, at 25°C (considering the oxides Ti$_2$O$_3$ and TiO$_2$ in the anhydrous state) [54].

The equilibrium potential for the Ti/Ti^{2+} transition is very negative (E_{eq} (Ti/Ti^{2+}) = -1.630 V vs. SHE), i.e. very negative relative to the stability range of water.

Therefore, in the water stability region, i.e. up on immersion in water, a spontaneous formation of a stable passive film of the oxides on the surface of the metal results in a protection of the metal from dissolution in a wide range of pH values (TiO$_2$ is practically insoluble in acid and alkaline media) [54]. Generally, Ti is stable in the presence of the majority of non-fluorinated aqueous solutions, besides moderate oxidizing solutions. Nevertheless, in very oxidizing solutions such as H$_2$O$_2$ solutions, Ti will be corroded as well as at very high electrode potentials.

Zr: As can be seen in Fig. 2.10, the domain of thermodynamic stability of metallic Zr lies well below that of water, so it is defined as a very base metal. The equilibrium potential of the Zr/Zr^{4+} transition is similarly negative as that for Ti, i.e. E_{eq} (Zr/Zr^{4+}) = -1.539 V vs. SHE. In very acid solutions, it has a great tendency to decompose water with a hydrogen evolution, dissolving as Zr^{4+} and ZrO^{2+} ions. In moderately acid, neutral and moderately alkaline solutions, it is covered with a protective film of the oxide ZrO$_2$. 2H$_2$O and in very alkaline

solutions it is not protected but dissolves as HZrO$_3^-$. The only well-defined oxide of Zr is zirconia, ZrO$_2$, which is stable at normal temperatures [54].
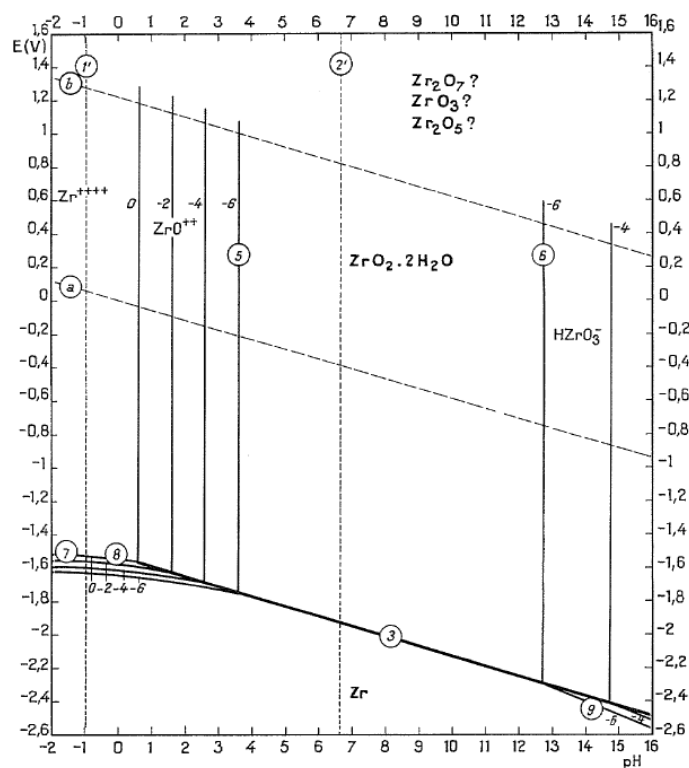

Figure 2.10: Potential-pH equilibrium diagram for the system Zr-H$_2$O, at 25°C [54].

Nb: From the Pourbaix diagram (Fig. 2.11) it is clear that Nb is a base metal, as its stability domain lies well below that of water. At all pH values, in the range of water stability, Nb tends to be covered by an oxide layer. Subsequently, its corrosion resistance depends on the intrinsic properties of the formed oxide layer such as its stability in the solution medium considered and the quality of the layer such as density, continuity, etc. Nb is not attacked by common acids and their mixtures. Fused caustic alkalis or alkaline carbonates or complexing substances may overcome its unreactivity [54]. The only stable oxide form of Nb in the presence of water is Nb$_2$O$_5$.
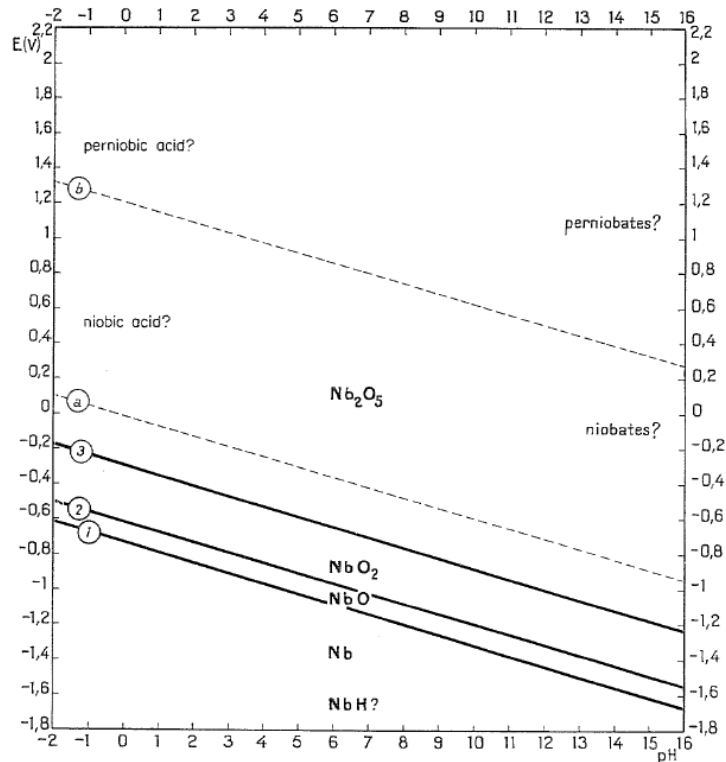
Figure 2.11: Potential-pH equilibrium diagram for the system Nb-H$_2$O, at 25°C [54].

Si: It is obvious from the Pourbaix diagram (Fig. 2.12) that Si is a strong reducing agent which tends to decompose water with the evolution of hydrogen and gaseous SiH$_4$, and the formation of silica or silicates.

In the range, where water is stabilized, Si is passivated by a film of silica SiO$_2$ at pH values below 10. Silica is very stable in the presence of water and aqueous solutions while alkaline solutions lead to dissolution of silica as SiO$_3^{2-}$ [54].

Considering the pH value of 7.4 for a simulated body fluid, which is important from the biomaterials aspect, it can be concluded from the above Pourbaix diagrams that all mentioned elements, constituting the glass-forming alloys and which are in the focus of the present study, will contribute to a stable passive layer formation on the alloy surfaces. However, at this point nothing can be derived regarding the effect of the high concentration of anions, in particular that of chloride ions. To investigate more accurately the corrosion behavior of the glass-forming alloy systems consisting of these elements, detailed electrochemical studies are required in which the kinetics of the reactions are considered as well.
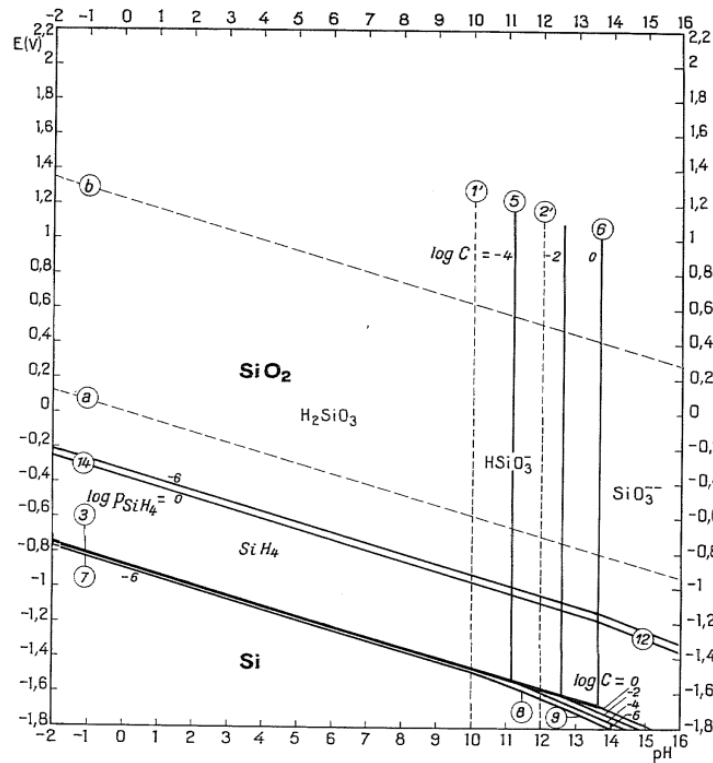
Figure 2.12: Potential-pH equilibrium diagram for the system Si-H$_2$O, at 25°C [54].

2.2 Ti-based crystalline alloys for load-bearing implants

2.2.1 Principal requirements of load-bearing implants

The field of biomaterials receives substantial attention due to their help in improving the quality and long life of people. The demand for artificial biomaterials which are used as implants to replace injured hard tissues increases rapidly by the growth of an aging population. Among all different kinds, the request for replacement implants is extremely high [55]. The proper materials are selected due to their mechanical properties and more specifically their biomechanical compatibility which is defined as adequate strength or mechanical properties adjustment between the bone and the implant. While hardness and tensile strength are required to be high enough, the Young's modulus of the material is desired to be as low as that of bone (~30 GPa) [56]. A low strength could result in the fracture of the implant and a high Young's modulus (high stiffness) could cause loosening of the implant due to the stress shielding effect and raise the revision surgery [3,55].

Biocompatibility of the selected materials has a great importance as well. It is described as the ability of the material to exist in contact with tissues of the human body without causing a non-acceptable degree of harm. That depends on numerous factors. Firstly, it concerns the human body response to it or the cell-biological activity of the implant. The higher the bioactivity, the higher is the osseointegration with surrounding bone. And the second main factor is the material degradation in the body environment as a consequence of low wear and corrosion resistance. This could result in a release of the constituent metal ions or particles of the implant alloy system into the body causing several reactions including allergic and toxic ones. Hence, choosing materials with high wear and corrosion resistance as well as including non-toxic and non-allergenic elements is of high significance [5,57,58].

Another essential concept is osseointegration which is in connection with the bioactive surfaces of the materials. This term is also defined as: "the formation of a direct interface between an implant and bone, without intervening soft tissue" [59]. A bioactive surface has the ability to integrate with the adjacent bone and other tissues and to increase the osseointegration. Many material surfaces lack a bioactivity and require an application of different treatment methods to modify surface chemistry, surface topography and roughness [55,60].

2.2.2 Titanium and its crystalline alloys

The material list for load-bearing implants mainly includes stainless steel, Co-Cr alloys and Ti or Ti-based alloys. Although stainless steel was the first used implant in the early 1930s and Vitallium (Co-based alloy) was the next applied implant [1], they did not remain as popular as the later metallic biomaterials - Ti and Ti-based alloys - due to several difficulties. Both systems, stainless steel and Co-Cr alloys, exhibit lower wear and corrosion resistance than Ti alloys, which results in significant metal species release including Ni, Cr and Co into the body environment [5]. These elements have been shown to expose toxic and allergenic problems in the human body [15,61,62]. Furthermore, they both possess very high Young's modulus values of about 210 GPa for stainless steel and about 240 GPa for Co-Cr alloys which leads to an insufficient stress transfer to the bone tissue and to loosening of the implant [63].

Since the middle of the 20th century, Ti and Ti-based alloys have been considered as non-degradable implant materials for load-bearing applications, such as hard tissue replacements implants in shoulders, knees, hips, etc. and bone fracture healing. Titanium (α) and (α+β)- or β-type Ti alloys attract higher attention due to their very good biomechanical properties, relatively low density, appropriate corrosion resistance and biocompatibility compared to

conventional stainless steel or Co-Cr-based alloys. Pure α-Ti and (α+β)-Ti-6Al-4V, which are still the most widely used materials among the Ti alloys for biomedical applications, have been developed in the early stage. Nevertheless, during the long-term implant use of Ti-6Al-4V, the problem of Al and V ions release into the body and subsequent related health problems raised [64]. Therefore, V has been replaced by Nb as Ti-6Al-7Nb [1] or Fe as Ti-5Al-2.5Fe [65]. The next generation of Ti alloys, which has been developed after 1990, is the class of β-type alloys such as Ti-13Nb-13Zr, Ti-12Mo-6Zr-2Fe. Both generations of materials are listed in Table 2.1, referring to their strength and Young's modulus. The second generation exhibits high strength besides a lower Young's modulus which makes them more appropriate for implant applications.

Table 2.1: Mechanical properties of biomedical Ti alloys [55].

Material	Standard	Modulus (GPa)	Tensile strength (Mpa)	Alloy type
First generation biomaterials (1950–1990)				
Commercially pure Ti (Cp grade 1–4)	ASTM 1341	100	240–550	α
Ti–6Al–4V ELI wrought	ASTM F136	110	860–965	α + β
Ti–6Al–4V ELI Standard grade	ASTM F1472	112	895–930	α + β
Ti–6Al–7Nb Wrought	ASTM F1295	110	900–1050	α + β
Ti–5Al–2.5Fe	–	110	1020	α + β
Second generation biomaterials (1990-till date)				
Ti–13Nb–13Zr Wrought	ASTM F1713	79–84	973–1037	Metastabe β
Ti–12Mo–6Zr–2Fe (TMZF)	ASTM F1813	74–85	1060–1100	β
Ti–35Nb–7Zr–5Ta (TNZT)		**55**	596	β
Ti–29Nb–13Ta–4.6Zr	–	65	911	β
Ti–35Nb–5Ta–7Zr–0.40 (TNZTO)		66	1010	β
Ti–15Mo–5Zr–3Al		82		β
Ti–Mo	ASTM F2066			β

More recently, Hanada et al. [6] produced several binary Ti-Nb alloys with different compositions by casting and solution treatments. At the content of 40-45 wt% of Nb, they exhibit a minimum of Young's modulus of about 62-65 GPa and by suitable thermo-mechanical processing and micro-alloying of cast samples, a further modulus reduction to 40–50 GPa and a high tensile strength of about 1 GPa can be achieved [7].

Mainly, β-type Ti alloys exhibit improved fatigue resistance and a superior wear and corrosion resistance than (α+β)-type ones which makes them preferable and also promising alloys for implant applications [66].

2.2.3 Surface modification of Ti and its alloys for bioactivation

In addition to biomechanical properties, surface properties are of high importance for long-term performance of implants as insufficient early osseointegration and afterwards particle release due to wear and corrosion processes could result in the failure of the implants. Consequently, the establishment of a proper surface state in order to stimulate bone cell growth and to improve the osseointegration of bone tissues is desired [2,61,67]. Surface modification is defined as any process that changes the characteristics of a material surface such as surface composition, structure and morphology to add biofunction to the alloy while bulk mechanical properties are maintained.

The natural surface of Ti and Ti-based alloys is covered by a spontaneously forming barrier-type oxide film (mainly TiO_2) which insulates the inner material from the external environment, resulting in high corrosion resistance [2]. This film is defined as bioinert and, therefore, Ti-based surfaces cannot easily bond to bone tissue. They are encapsulated after implantation by fibrous tissues which isolate them from the surrounding bone. As a consequence, this may result in a loosening of the implant after long-term resorption of bone tissue. Surface modifications are applied not only to improve the bone-bonding capability by inducing bioactivity while preserving the properties of the bulk material, but also to increase the wear and corrosion resistance of the implants [68,69].

Current methods of surface modification for implant devices for long-term application are applied to enhance the bone formation which can be chemical bonding or mechanical anchoring [70]. The chemical bonding of metals and bone is not expected naturally but performing some methods which form a layer on the surface capable of bonding with it, makes it possible. Changing the surface morphology into rough and/or porous surface is expected to improve the ingrowth of bone into modified material surface. Figure 2.13 shows the evaluation of surface modification techniques for improving the hard tissue compatibility at the research level. They are categorized into four generations: (i) mechanical surface: grind machining, (ii) morphological surface: grooving, blast, acid etching, and anodic oxidation (TiO_2 nanotubes), (iii) physicochemical active surface: chemical treatment and hydroxyapatite (HA) coating, (iv) biochemical active surface: immobilization of biofunctional molecules such as collagen and peptide [67,70].

Most of the commercial modified Ti and Ti-based alloys are included in the second generation. Those methods are applied in order to enhance TiO_2-based coatings, porosity, thickness of the oxide film and forming anatas vs. rutile structure. Furthermore, a few belong to the third

generation to deposit a bone-like osteoconductive coating by methods such as HA formation or ion implantation of Ca ions.

The fourth generation is still far from commercializing due to the necessity of controlling safety, quality of maintaining during storage and dry-conditioned durability of the immobilized layer.

It is suggested that above established methods are applicable for new alloy systems of β-type Ti alloys and Ti-based metallic glasses considering the necessity of adapting them. Nano-scale surface modifications are in the focus of interest as it has been shown that they better match with cell functions [67].

Thermal oxidation of the materials forming an oxide layer on the surface is considered as a surface modification process which can be categorized as a second generation method.
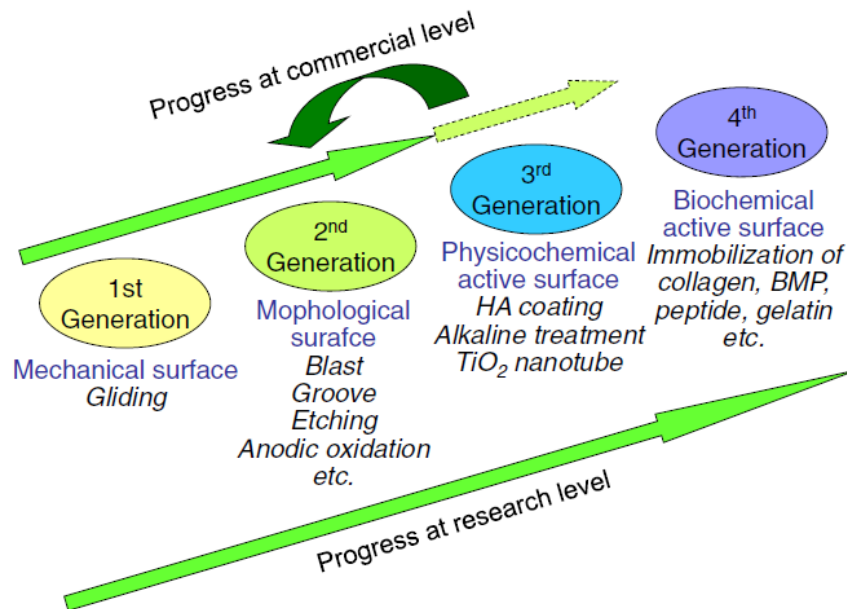

Figure 2.13: History of surface modification techniques to improve hard-tissue compatibility regarding the commercial and research level [70].

Thermal oxidation of cp-Ti and some of the Ti-based alloys such as Ti-6Al-4V, Ti-10Ta-10Nb, Ti-13Nb-13Zr and Ti-15Zr-4Nb has been investigated considering the morphological features, structural characteristics, microhardness and corrosion resistance in comparison with untreated samples [71-75]. The optimized samples (regarding applied temperature and exposure time) exhibit more promising properties as bio-implant materials.

2.3 Ti-based glass-forming alloys for load-bearing implants

Recently, glassy Ti-based alloys have attracted increasing interest as advanced materials for biomedical applications, especially for load-bearing implants, because of their very high strength (in the order of 1800 to 2500 MPa) and low Young's modulus values (in the order of 80 to 100 GPa; it can be much lower than the one of crystalline (α+β)-type Ti alloys), their low density and high wear resistance [8,9,11,46]. This can be seen in Fig. 2.14.

Mainly, the Ti-based BMGs with good glass-forming ability which were developed at the early stage, contain Ni. Some typical alloy systems are Ti-Cu-Zr-Ni with maximum strip thickness of 4 mm [76], Ti-Ni-Cu-Sn with maximum cast rod diameter of 5 mm [77], Ti-Cu-Ni-Si-B with maximum cast rod diameter of 2 mm [78], Ti-Cu-Ni-Sn-Be with maximum cast rod diameter of 2 mm [79], Ti-Cu-Ni-Al-Zr-Si-B rods with diameters up to 2.5 mm [80].

However, elements like Ni and Be are considered to be highly toxic and/or carcinogenic which makes Ni and Be-containing alloys not suitable for implant applications [3,55,81]. Typical developed Ni-free Ti-based glassy alloys and their characteristics are summarized in Table 2.2. Mostly, they contain large amounts of Cu which is a highly cytotoxic element [15,81]. Besides, it is critical for the initiation of pronounced pitting events [82,83]. Lin et al. [84] have compared the electrochemical behavior of different metallic glasses on Zr-, Ti- and Ta-base in Hanks solution and found out that Cu has a critical role for the pitting susceptibility of metallic glasses. Recently, only a very limited number of Ti-based glassy alloys without harmful elements have been developed, e.g. the systems Ti-Zr-(Ta/Pd)-Si [11,85], Ti-Si, Ti-Zr-Si and Ti-Nb-Si [86-89]. The main characteristics of the Ti-Zr-(Ta/Pd)-Si alloys are included in Table 2.2.
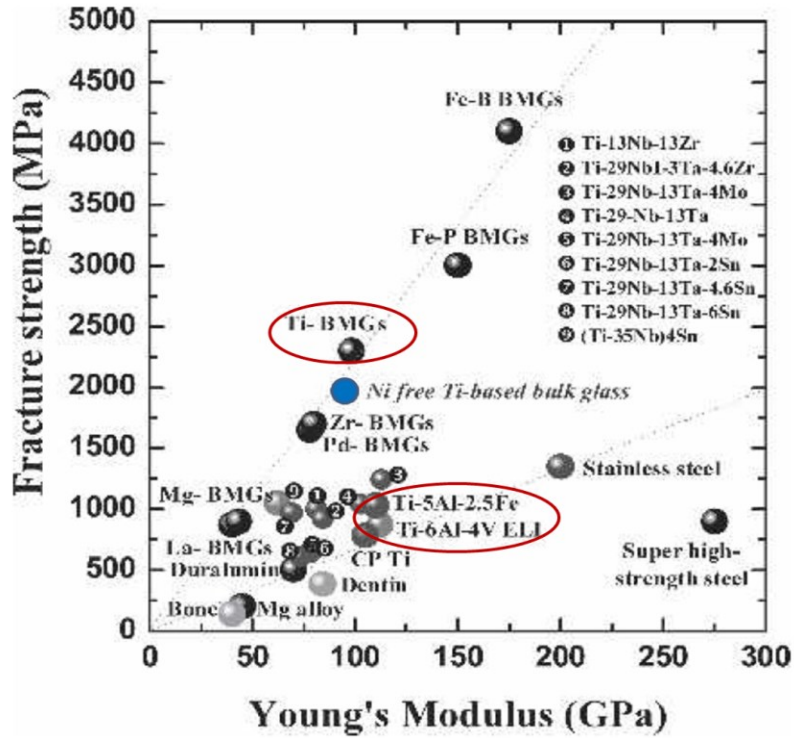
Figure 2.14: Relationship between tensile strength and Young's modulus for some typical BMGs [9].

Table 2.2: Recent Ni-free Ti-based glassy alloys

System	Other characteristics	Mechanical Properties	Ref.
$Ti_{40}Zr_{10}Cu_{40-x}Pd_{10+x}$ (x = 0, 2, 4, 6, 8, 10)	rod φ 6 mm: amorph.	E(GPa): 82	Zhu S.L. , Inoue A 2007 [10]
$Ti_{40}Zr_{10}Cu_{36}Pd_{14}$	rod φ 7 mm: amorph.	E(GPa): 55	Zhu S.L. , Inoue A 2008 [90]
$Ti_{40}Zr_{10}Cu_{36-x}Pd_{14}Sn_x$	rod φ 10 mm: amorph.	———	Zhu S.L., Inoue A 2008 [91]
$Ti_{45}Zr_{10}Pd_{10}Cu_{31}Sn_4$	rod φ 4 mm: amorph.	E(GPa): 95 σ_{f-comp}(MPa): 1970	Oak J, Inoue A 2007 [9]
$Ti_{40}Zr_{10}Cu_{40-x}Pd_{10}Si_x$ (x = 0, 1, 2)	rod φ 5 mm: amorph. ribbon: amorph.	E(GPa)< 85 σ_{f-comp}(Mpa)>1900	Zhu S.L. , Inoue A 2007 [92]
$(Ti_{40}Zr_{10}Cu_{36}Pd_{14})_{100-x}Si_x$ (x = 0, 1,2,3,4,5)	rod φ 6 mm: amorph.+ nanocrystals	———	Zhu S.L. , Inoue A 2008 [14]
$(Ti_{40}Zr_{10}Cu_{36}Pd_{14})_{100-x}Nb_x$ (x = 1, 3, 5)	rod φ 2 mm: amorph.+ nanocrystals	E(GPa): 80 σ_{f-comp}(MPa): 2050	Qin F. X., Inoue A 2008 [93]
$(Ti_{40}Zr_{10}Cu_{36}Pd_{14})_{100-x}Ta_x$ (x = 0, 1, 3, 5)	rod φ 2 mm: amorph.+ nanocrystals	———	Qin F. X., Inoue A 2007 [94]
$(Ti_xZr_yTa_z)_{85}Si_{15}$	ribbon: amorph.	E(GPa): 88 σ_{f-comp}(MPa): 2390	Oak J, Inoue A 2007 [85]
$Ti_{45}Zr_{50-x}Pd_xSi_5$ (x = 35, 40, 45)	ribbon: amorph.	E(MPa): 73	Oak J, Inoue A 2008 [11]

28

2.3.1 Development of Ti-based glassy alloy systems for implant applications

The main problem in developing metallic glasses for biomedical applications is the achievement of a high glass formation ability of the alloys without using harmful alloying elements. The toxicity of metals depends on their chemical state and on the concentration of the metallic ions released by an implant into the body environment [15,56,95].

Metallic ions are released by different mechanisms comprising corrosion, wear and electrochemical processes which are mechanically accelerated such as stress and fretting corrosion [5,95]. Laing et al. [96] identified that Ni, Co, Cr, Fe, Mo, V and Mn cause severe adverse tissue reactions and Wapner [97] has indicated that Ni, Co, Cr, Al and V have a cytotoxic effect. Later studies on the cytotoxicity of metallic elements revealed that Cr, Cu and Ag are toxic, Ni, Zn and Co are highly toxic while Pt, Sn, In, Ti, Au and Pd did not exhibit any toxic effect and are therefore considered as vital elements [15,62,81,95]. The cytotoxicity of Cu has been revealed even for alloys with a low amount of Cu (~17 wt.-% Cu in a prosthodontics material: Type IV gold alloy) [15]. To develop a suitable Ti-based glassy alloy system for implant application, it is essential to consider the glass-formation parameters according to the empirical rules (see section 2.1.2) and the biological safety of the alloying elements. These parameters were summarized by Calin et al. [16] and are illustrated in Fig. 2.15. Good glass-former elements which satisfy the empirical rules (negative ΔH of mixing and large atomic size mismatch of >12%) are B, Si, P, In, Be, Fe, Co, Ni and Cu. Among these elements Si, In, P and B are biocompatible.

In Ti-based alloy systems, depending on the influence of the alloying elements on the β-transus temperature of Ti, either the α-Ti (hcp) or β-Ti (bcc) crystal structures are stabilized or the alloying elements are called α-stabilizer or β-stabilizer, respectively [98]. In the group of β-stabilizer elements, the β-isomorphous ones show much higher solid solubility in Ti while the β-eutectoid stabilizers have a reduced solid solubility in Ti and result in a formation of intermetallic compounds with large negative heat of mixing [99]. Therefore, the β-eutectoid elements such as Fe, Mn, Cr, Co, Ni, Cu and Si are considered to promote the glass formation ability under non-equilibrium processing (solidification) conditions [16].
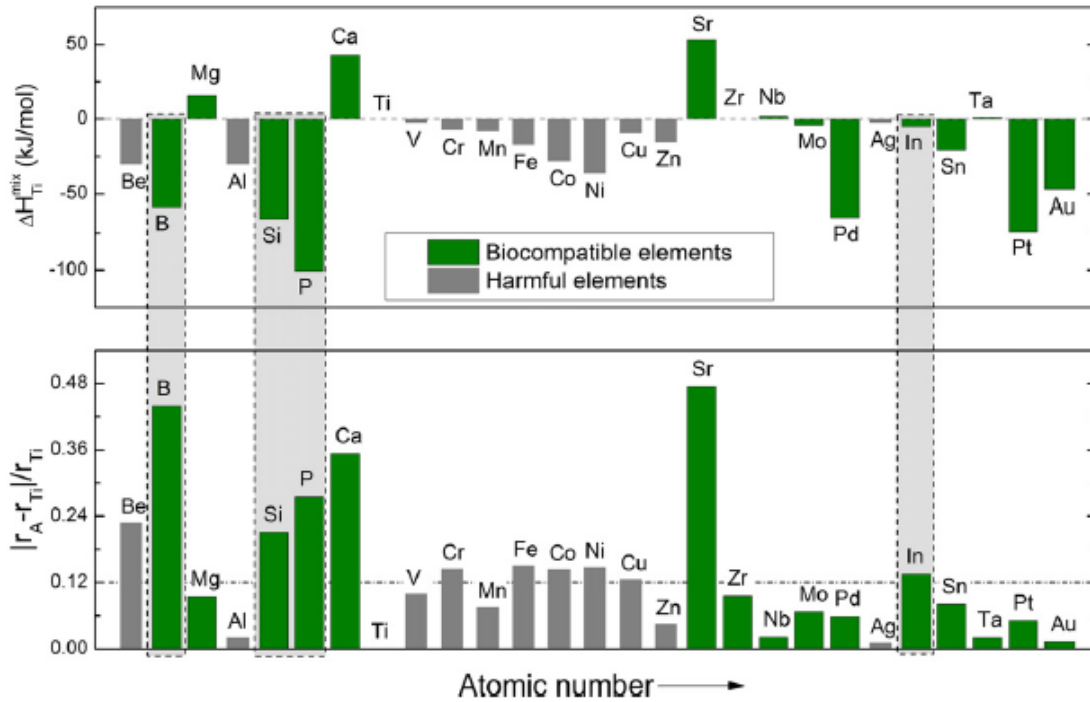
Figure 2.15: Correlation between the GFA and the biological safety of alloying elements in Ti [16].

According to the above approach, new glassy Ti-based compositions based on Ti-Zr-Si and Ti-Zr-Nb-Si have been developed [16]. Si has been selected due to its role in promoting the glass formation of the system as it has a large negative ΔH^{mix} with Ti, Zr and Nb [11,99]. Furthermore, it is relatively cheap, has low density and good biocompatibility [100] and it is beneficial to bone and connective tissue health [101]. Zr is expected to improve the GFA because of its larger atomic size than that of Ti and Si although its heat of mixing with Ti is almost zero [102]. Studies on the binary systems of Ti-Si and Zr-Si revealed a deep eutectic at a Si content below 20 at.-%, which is expected as glass forming composition [20,103]. As a result, also in the ternary system the desirable glass forming composition should be found around or at a deep eutectic at the Ti-rich corner. From the known melting diagram of Ti-Zr-Si, the defined eutectic composition is $Ti_{78}Zr_{11}Si_{11}$ which has been identified as a crystalline alloy by XRD [16,104]. Therefore, for this work a composition close to the eutectic by increasing the amount of Si from 11 at.-% to 15 at.-%, leading to $Ti_{75}Zr_{10}Si_{15}$ was chosen.

The addition of a further element to a ternary alloy is expected to further promote the GFA of the system, according to the empirical rules, by more confusing the system. As mentioned above, the GFA of the Ti-Zr-Ta-Si system has already been investigated [85]. In this work, Ta was replaced by Nb ($Ti_{60}Nb_{15}Zr_{10}Si_{15}$), since Nb is very similar to Ta with regard to the

empirical rules (see Fig. 2.9). In addition, Nb has a Young's modulus of 105 GPa which is much lower than that of Ta (186 GPa) and is therefore more suitable for implant applications. Furthermore, Nb has a lower density (ρNb = 8.5 g/cm^3, ρTa = 16.6 g/cm^3), lower melting point ($T_{m,Nb}$ = 2750 K, $T_{m,Ta}$ = 3270 K) and lower cost (7 times cheaper than Ta), which makes it preferable for large scale production [103].

These considerations based on thermodynamic and structural aspects of glass formation should lead to new metallic glassy alloys. However, due to the demand to omit toxic late transition metal elements (Ni, Cu), the glass-forming ability of these new alloys is expected to be quite limited. Thus, kinetic aspects of glass formation are of critical importance in the present study. This refers in particular to the specific cooling rate conditions that are realized during melt-spinning and which are controlled for example by the overheating temperature of the melt and by the sample geometry (thickness).

2.3.2 GFA, thermal and mechanical properties of selected Ti-based glassy alloys

As it was mentioned in section 2.1.5, the BMGs exhibit typical strength that are about 2-3 times higher than those of their crystalline counterparts, lower Young's modulus values and large elastic limits of ~2% (close to those of polymer materials). Nevertheless, they show low plasticity which is caused by an inhomogeneous plastic deformation, for example by severe shear localization [105].

Ti-based BMGs are expected to be applied as implant biomaterials due to the above stated properties. The mechanical properties of the Ni-free Ti-based alloys in the system Ti-Zr-Cu-Pd are promoted in comparison with the commercial crystalline (α+β)-type Ti-6Al-4V alloy (strength: 1720 MPa, Young's modulus: 120 GPa) with a strength of 2000 MPa and a Young's modulus of 90 GPa. However, as discussed in section 2.3.1, even Cu is considered as harmful element for the human body and is tried to be avoided in the newly designed systems.

A new Ni and Cu-free glassy alloy system is Ti-Zr-Ta-Si developed by Oak et al. [85]. Mechanical and chemical properties of the produced glassy ribbons were investigated and it was revealed that changing the composition according to the Ti and Ta ratio affected the properties significantly. Thermal studies of $Ti_{60}Zr_{10}Ta_{15}Si_{15}$ displayed that it crystallizes through two exothermic reactions at about 810 K and 950 K. Thus, those glassy alloys will be stable not only during application in the body (37°C = 310 K), but also during handling, e.g. sterilization (>100°C = 373 K). It exhibits a good bending ductility, a high strength of 2390 MPa and a Young's modulus of 88 GPa, and therefore, it shows good potential for bone fixation

device application. The other glassy alloy system is $Ti_{45}Zr_{50-x}Pd_xSi_5$, which was developed in the same group [11]. Addition of 10% and more of Pd results in the formation of ribbons with a single glass phase. For 35-45% of Pd, the T_g can be recognized in the corresponding DSC curves. $Ti_{45}Zr_{10}Pd_{40}Si_5$ exhibits the largest supercooled liquid region of 36 K, a Vickers's hardness of 747 H_v and a dynamic Young's modulus of about 73 GPa. It also shows good bending ductility and is therefore considered as a potential candidate to be applied as a bone fixation device.

2.3.3 Corrosion properties of Ti-based glassy alloy systems

As it has been discussed in section 2.1.5, different features are affecting the corrosion behavior of alloys in crystalline and glassy states and have to be carefully considered in order to improve or reduce the corrosion resistance. This makes it impossible to provide a certain rule for the comparison of the corrosion behavior of the glassy alloys and their crystalline counterparts.

The Ni-free glass-forming Ti-based alloys which have been investigated regarding their corrosion resistance include cylindrical rods of $Ti_{45}Zr_{10}Pd_{10}Cu_{31}Sn_4$ [106], $Ti_{47.5}Zr_{2.5+x}Cu_{37.5-x}Pd_{7.5}Sn_5$ [46], glassy ribbons of $Ti_{47.5}Zr_{15}Cu_{30}Pd_{7.5}Sn_5$ [45] and porous Ti-based BMGs of $Ti_{45}Zr_{10}Cu_{31}Pd_{10}Sn_4$ prepared by spark plasma sintering [107]. Experiments were typically performed in simulated body fluids and at body temperature (37°C). The corrosion behavior investigations of bulk glassy $Ti_{47.5}Zr_{2.5+x}Cu_{37.5-x}Pd_{7.5}Sn_5$ (x = 0, 5, 7.5) samples revealed that although they exhibit lower passive current densities than those of pure Ti and Ti-6Al-4V, pitting corrosion is a critical issue. As it can be seen in Fig. 2.16, the pitting potential of these Cu-containing alloys is shifted to lower values with increasing Cu content. Therefore, the Cu-containing glassy alloys not only show cytotoxic effects in the human body environment (see section 2.3.1), but also their limited corrosion resistance in synthetic body fluids was identified as a critical issue in life-time prediction [46].

As mentioned in section 2.3.1, only a very limited number of Ti-based glassy alloys without harmful elements has been developed so far, i.e. Ti-Zr-Pd-Si and Ti-Zr-Ta-Si.

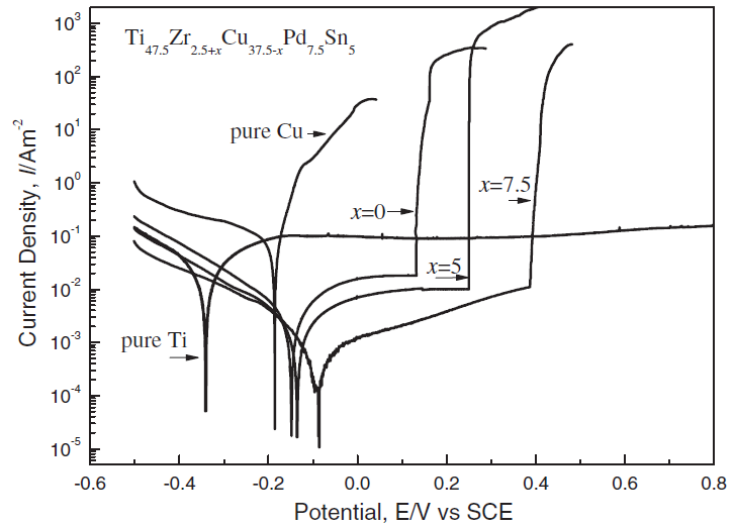Figure 2.16: Anodic polarization curves of $Ti_{47.5}Zr_{2.5+x}Cu_{37.5-x}Pd_{7.5}Sn_5$ bulk glassy alloys in Hanks' solution at 37°C [46].

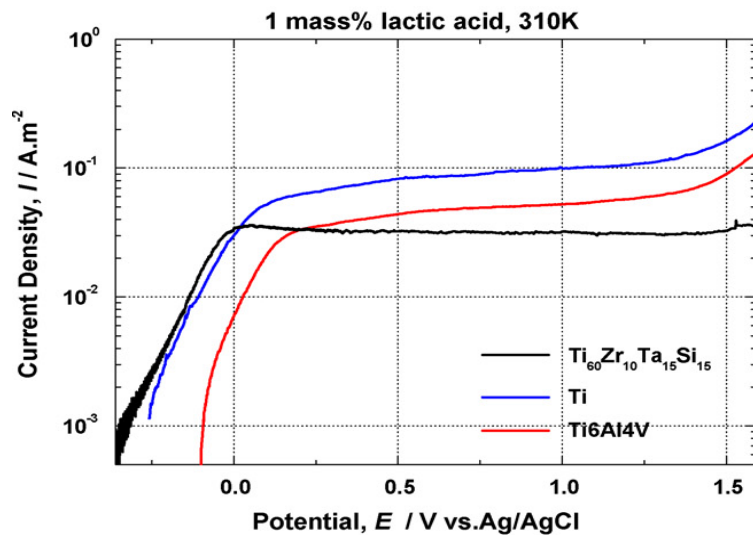

Figure 2.17: Anodic polarization curves of $Ti_{60}Zr_{10}Ta_{15}Si_{15}$ glassy ribbons in 1 mass% lactic acid at 37°C, compared to those of Ti and Ti6Al4V [85].

The first corrosion studies revealed that glassy ribbons of $Ti_{45}Zr_{10}Pd_{40}Si_5$ show lower current density values and therefore a better passivity up to 1V (vs. Ag/AgCl) than Ti and Ti-6Al-4V. Also for $Ti_{60}Zr_{10}Ta_{15}Si_{15}$ glassy ribbons (see Fig. 2.17) an enhanced corrosion resistance in 1 mass% lactic acid and PBS at 37°C was confirmed [11,85].

2.3.4 Surface modification of Ti-based glassy alloy systems

The general aspects of surface modification methods for Ti-based alloys have been described in section 2.2.3. Although many different surface modification methods are well-developed for commercial Ti-based alloys, there have not been many investigations to transfer those available methods to new Ti-based metallic glassy alloys.

One of the aims of applying surface modification methods is to increase the bioactivity of the implants. The bioactivity of metallic implants can be evaluated for example by the formation of hydroxyapatite (HA) in body fluid and the growth rate of the apatite layer. In order to improve the apatite-forming ability of Ti-based BMGs, some methods such as Ti coating on Ti-based BMG substrates by physical vapor deposition (PVD) [108,109], or a two-step method consisting of hydro-thermal-electrochemical treatment followed by a pre-calcification treatment have been developed. After applying the last method to the surface of a $Ti_{40}Zr_{10}Cu_{36}Pd_{14}$ metallic glass and immersion in Hanks' solution (simulated body fluid) for six days, a porous apatite layer formed which is strongly bonded to the surface of the metallic glass [110]. Hydrothermal, electrochemical and hydrothermal-electrochemical processes in NaOH solution have been applied to the surface of glassy $Ti_{40}Zr_{10}Cu_{36}Pd_{14}$ to enable formation of low cytotoxic bioactive titanate nano-mesh structures on their surfaces. The results showed that among the three methods, the hydrothermal-electrochemical process was the best to fabricate this layer which enabled to induce a hydroxyapatite layer formation with strong adhesion (shown in Fig. 2.18) [111].
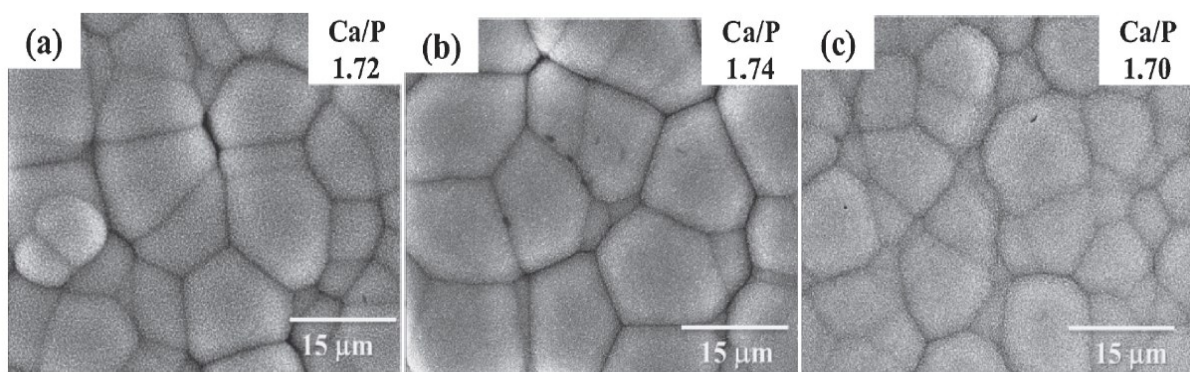

Figure 2.18: SEM images of the surface of samples treated by a) hydrothermal, b) electrochemical and c) hydrothermal-electrochemical process after immersion in simulated body fluid for 12 days [111].

Hydrothermal hot-pressing treatment was also successfully used with the purpose of making $Ti_{40}Zr_{10}Cu_{36}Pd_{14}$ and $(Ti_{0.40}Zr_{0.10}Cu_{0.36}Pd_{0.14})_{99}Ca_1$ bulk metallic glass surfaces bioactive [112]. For coating or surface modification of BMGs, low-temperature processes such as chemical treatment are more desirable as such processes maintain their structural state and their excellent mechanical properties. A chemical treatment method was also employed for the bulk glassy $Ti_{40}Zr_{10}Cu_{34}Pd_{14}Sn_2$ alloy to produce a bioactive layer and resulted in a dense and uniform calcium phosphate layer on the surface of the alloy [113].

In the present study, thermal oxidation was applied as a surface modification technique on nearly glassy composition ribbons in order to increase the bioactivity of the surface of the alloys. This method is considered as a new approach for the metallic glassy alloys. Finally, simulated body fluid (SBF) tests were performed to evaluate the bioactivity of the modified sample surfaces.

Summary: Based on a literature survey on Ti-based metallic glasses, in this study the following key questions will be addressed:

1) Effect of processing conditions (cooling rate) and of alloy composition (Nb content) on microstructure evolution upon rapid solidification of glass-forming $Ti_{75}Zr_{10}Si_{15}$ and $Ti_{60}Zr_{10}Nb_{15}Si_{15}$ alloys

2) Relation between microstructural state and mechanical properties at room temperature

3) Corrosion behavior of $Ti_{75}Zr_{10}Si_{15}$ and $Ti_{60}Zr_{10}Nb_{15}Si_{15}$ in comparison with known commercial cp-Ti and Ti-40Nb (a β-type Ti-based alloy) in simulated body fluid

4) Assessment of possibilities for surface activation of glassy $Ti_{75}Zr_{10}Si_{15}$ and $Ti_{60}Zr_{10}Nb_{15}Si_{15}$ alloys by thermal oxidation and evaluation of their bioactivity by performing SBF tests

3 Experimental

3.1 Material

Master alloys with nominal compositions $Ti_{75}Zr_{10}Si_{15}$ and $Ti_{60}Zr_{10}Nb_{15}Si_{15}$ were prepared by arc-melting a mixture of the constituent elements with high purity (99.9%) and subsequent copper mold casting and melt-spinning. The appropriate amounts of each element were weighted and alloyed in an arc melter (Edmund Bühler GmbH; device number: 2414048) in highly purified argon atmosphere. The ingots were re-melted 5 times to insure good mixing and to achieve good chemical homogeneity. Crystalline rods with dimensions of 4 mm in diameter and 50 mm in length were prepared by copper mold casting under argon atmosphere. A single Cu-roller melt-spinning device was employed to produce melt-spun ribbons with ~50 μm thickness and 3-4 mm width in an Ar atmosphere (Edmund Bühler GmbH; device number: 2416031). Pieces of the master alloy of approximately 4-8 g and a graphite crucible were used. The melting temperatures of the $Ti_{75}Zr_{10}Si_{15}$ and $Ti_{60}Zr_{10}Nb_{15}Si_{15}$ alloys, as determined from DSC measurements (not shown here) as liquidus temperatures of the endothermic event, are 1620 ± 2 K and 1715 ± 2 K, respectively. Therefore, overheating temperatures of the melt (1900-2053 K) were employed to obtain a single-phase molten state without any residual high melting phases that could act as heterogeneous nuclei during solidification. The typical melt-spinning parameters were: wheel speed: 35 m/s, distance between wheel and nozzle: 0.4 mm. Sample preparation was conducted by M. Frey and S. Donath. The chemical analysis has been performed by A. Voß and the result was in good approximation. The oxygen content was measured to be about 0.073 % by H. Bußkamp.

3.2 Microstructural characterization

Several techniques were used to characterize the microstructure of the samples: (1) X-ray diffraction (XRD) with different X-ray radiations in reflection configurations, (2) scanning electron microscopy (SEM), (3) transmission electron microscopy (TEM), and (4) differential scanning calorimetry (DSC). The details of each characterization technique and employed analytical methods are reported in the following.

Exprimental

X-ray diffraction: X-ray diffraction (XRD) is a versatile, non-destructive technique that reveals detailed information about the chemical composition, physical properties and crystallographic structure of natural and manufactured materials. X-ray diffraction is based on observing the scattered intensity of an X-ray beam hitting a sample as a function of incident and scattered angle, polarization, and wavelength or energy. In case of a crystalline sample, this was explained by W. L. Bragg [114] considering the crystal as a set of discrete parallel planes separated by a constant parameter d. It was proposed that the incident X-ray radiation would produce a Bragg peak if their reflections of the various planes interfered constructively. The interference is constructive when the phase shift is a multiple of 2π. This condition can be expressed by Bragg's law:

$$n \cdot \lambda = 2 \cdot D \cdot \sin \theta \qquad \text{(eq. 3.1)}$$

where *n* is the reflection order and *d* is the interplanar distance of one family of crystallographic planes [114]. If the chemistry of the sample is known then the measured diffraction peaks are identified with the help of the specialized database by comparing them with the existing patterns. In the case of multiphase samples, where peaks may shift and overlap, Rietveld refinements can be used [115]. In contrast, the XRD patterns of a glassy alloy exhibit broad and shallow peaks corresponding to the specific SRO/MRO structure of the metallic glasses (see section 2.1.1).

In this work, XRD patterns in reflection mode were obtained using a Philips PW1050 diffractometer with Co-Kα radiation ($\lambda = 0.17889$ nm) operating at 40 kV. The diffraction patterns were recorded using a 2D detector. Subsequently the intensity of the 2D XRD patterns was integrated using the Fit2D software [116] in order to have the intensity as a function of 2θ. Samples were stick to an amourphous silica holder and the measurements were done from 20° to 120° for ribbons and from 20° to 140° for crystalline rod samples in step mode with a step size of 0.05° and 42 sec per step.

High resolution scanning electron microscopy (HRSEM): HRSEM investigations were performed for the crystalline samples to characterize their microstructure. In the present work, they were carried out using a high-resolution scanning electron microscope (Zeiss, Gemini 1530). An electron beam arrives at the surface of a sample and several kinds of signals are emitted as a result, which are then collected in suitable detectors. It is equipped with secondary, back-scattered, in-lens secondary, and EDX detectors. Secondary electrons give information about the surface topography, while back-scattered electrons deliver contrasts according to the

atomic number of the elements on the surface besides topography. Images were done in the secondary and back-scattered electron mode, using an acceleration voltage of 1-20 kV.

Energy dispersive X-ray analysis (EDX) was also conducted for the analysis of the composition of the alloys. The Si (Li) EDX detector was linked to the QUANTAX software (Bruker AXS) in order to quantify the EDX patterns. The principle of the EDX is based on the fact that each element with its unique atomic structure provides its characteristic X-rays which are used for the element's identification. X-ray mapping was used to obtain the distribution of constituent elements of samples at the surface. In this technique some regions of the sample are scanned by a selected part of the x-ray spectra corresponding to each of the elements in the sample.

Before imaging, the rod samples were embedded into an epoxy conductive resin, then mechanically polished to mirror-like appearance and finally polished by 0.04 μm SiO_2 suspensions (OP-U, Struers). Finally, to enhance microstructural features, the samples were chemically etched (with a solution of 50 ml distilled water, 2.5 ml H_2O_2, 1 ml HF) for 5 seconds. The ribbons were used without any treatment.

Transmission electron microscopy (TEM): Transmission electron microscopy was conducted for high-resolution structural analysis of melt-spun ribbons. Dark- and bright-field images were taken together with selected area electron diffraction (SAED) patterns in order to investigate whether the structure is fully amorphous or is a mixture of glassy phase and nanocrystals. This was further assisted using high-resolution TEM investigations, which is capable to identify the presence of very small nanocrystals (<10 nm). For samples prepared by the thermogravimetry method (section 4.4), EDX spectra were acquired on the cross-section of samples besides dark- and bright-field images.

TEM studies were carried out using a Philips Teknai F30 microscope operating at 300 kV. For preparing melt-spun ribbon samples, at first samples with a thickness of 30-50 μm were dimple ground using a GATAN dimple grinding machine to thin the center of the sample down to 15-20 μm. Then ion milling (GATAN-PIPS ion milling machine) was used to make samples thin enough to be studied in the TEM. Focused ion beam (FIB) milling was used in order to prepare TEM specimens from samples produced by thermogravimetry. This was done using a FIB 1540XB device manufactured by Zeiss. TEM sample preparations were conducted by A. Pöhl and D. Lohse and TEM investigations were performed by M. Samadi Khoshkhoo.

Differential scanning calorimetry (DSC): DSC is the most widely used thermal analysis technique for the study of physical or chemical changes of a sample which occur as the

temperature is increased or decreased. The sample, positioned in an appropriate crucible (depending on the nature of the alloy that will be analyzed), is placed in a furnace and subjected to the desired temperature program including isochronal and/or isothermal steps. In this technique it is mandatory that the sample and the reference sample (second crucible) are maintained at the same temperature at any time during the experiment. This is achieved by compensating independently the supplies of power to the sample and to the reference. A typical isochronal DSC curve for a metallic glass has been described in section 2.1.4.

DSC experiments were performed with a Perkin Elmer DSC-7 at a heating rate of 10 K/min. An alumina crucible was used as a reference holder as well as a sample holder. The reference material in all the DSC experiments was simply the empty alumina holder. For each experiment, two consecutive scans were made: the first one to let the sample crystallize and measure its thermal properties; the second one (in the same sample) was made for baseline correction.

3.3 Mechanical characterization

Mechanical characterization helps to define the range of load-bearing applicability of a material and to establish the service life of a device made from this material that can be expected. Measuring the properties such as strength, hardness, toughness, elasticity, plasticity, brittleness, and ductility reveals how metals behave under an applied load in terms of the type of forces or stress that the metal must withstand and the way they resist. Different tests corresponding to different types of stress such as compression, tension, shear, torsion, impact can be performed and many materials show marked differences. Therefore, the mechanical properties of a material are not constant and can change as a function of temperature, type of stress, rate of loading, and other conditions.

In this work, compression tests, acoustic measurements and nanoindentation were carried out to study the mechanical properties of crystalline rods and nanocomposite ribbon samples. Compression test were used to determine the yield strength, Young's modulus and the plasticity. However, to determine more accurately Young's modulus, acoustic measurements were also carried out. Nanoindentation studies were performed with the aim to measure the hardness, which on its turn can be related to the yield stress and the reduced Young's modulus. This technique is especially useful to measure the hardness of thin films or small areas, besides it also allows the determination of parameters related to the wear resistance.

Nanoindentation: The nanoindentation technique is based on contacting a material (the surface of the sample), whose mechanical properties such as hardness and Young's modulus are unknown, with another material, whose properties are known (the indenter tip). It is an indentation test at which the length scale of the penetration of the indenter tip is measured in nanometers and the applied load is in the order of μN and mN. It is considered as a depth-sensing indentation technique, as the penetration depth is continuously monitored as a function of the load during the test.

The test consists of a loading sequence and afterwards an unloading. By loading, the load placed on the indenter tip is increased as the tip penetrates further into the specimen and soon reaches a user-defined value. At this point, the load may be held constant for a period or removed. While indenting, various parameters such as load and depth of penetration can be measured. A record of these values can be plotted on a graph to create a load-displacement curve (such as the one shown in Fig. 3.1). These curves can be used to extract mechanical properties of the material [117].

The hardness H is evaluated as the maximum load, P_{max}, divided by the residual indentation area, A:

$$H = \frac{P_{max}}{A} \qquad \text{(Eq. 3.2)}$$

and the reduced Young's modulus E_r can be calculated using the stiffness of the contact. The slope of the curve, dP/dh, upon unloading is indicative of the stiffness S of the contact. This value generally includes a contribution from both the material being tested and the response of the test device itself. The reduced modulus is defined as:

$$E_r = S \frac{\sqrt{\pi}}{2\beta\sqrt{A}} \qquad \text{(Eq. 3.3)}$$

where β is a correction factor which depends on the geometry of the indenter, i.e. 1.034 for a Berkovick type.
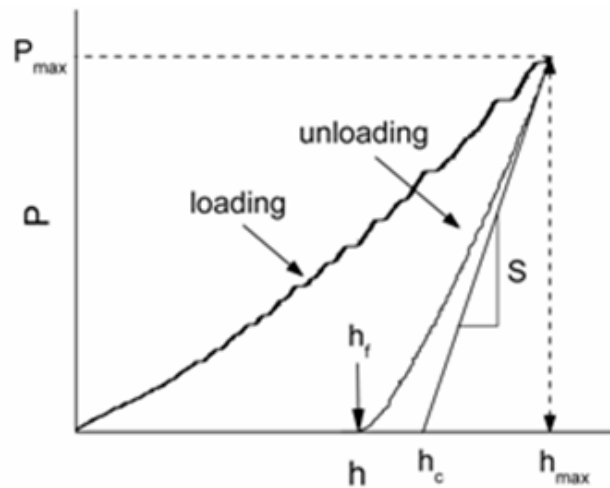
Figure 3.1: A typical load-displacement nanoindentation curve [118].

Different types of tips, depending on the material to be tested or the data which are required can be chosen. Usually spherical or pyramidal indenters are used; for instance, the Berkovich indenter, the most widely used in nanoindentation and also the one used in this work, has the advantage that the edges of the pyramid are more easily constructed to meet a single point. It is generally employed in small-scale studies.

Prior to nanoindentation, the samples were prepared by embedding them in polyester resin and subsequent polishing to a mirror finishing state using 1 μm diamond paste. Indentation was implemented along the cross-section of ribbons. The indentation function consisted of a loading segment of 40 s to a maximum force of 30 mN, followed by a load holding segment of 20 s, and an unloading segment of 40 s. The results represent the average of a total of at least 40 indentations for rod samples and 20 for ribbons. An UMIS device from Fischer-Cripps Laboratories equipped with a Berkovich pyramidal-shaped diamond tip was employed. The set-up is equipped with an optical microscope which permits to select a suitable site for indentation and even observe the indentations for intermediate applied loads. Nanoindentation studies were conducted at the University Autònoma Barcelona (UAB) in collaboration with Prof. M.D. Baro and Prof. J. Sort.

Compression tests: A compression test determines the behavior of a material in a defined shape under a continuous compressive force. The specimen is compressed and the displacement and the applied force are recorded. Compressive stress (the force acting per unit area (F/A_0) and strain (the change in dimensions per unit length ((l_0-l)/l_0)) are calculated and plotted as a stress-strain diagram which is used to determine the elastic modulus and the yield strength.

Exprimental

In a compression test, there is a linear region where the material follows Hooke's Law. Hence the Young's modulus (*E*) is the slope of the stress-strain curve in the elastic region σ = *E* · ε. In this region, the material deforms elastically and returns to its original length when the stress is removed. This linear region terminates at a point known as the yield point. Above this point the material behaves plastically and will not return to its original length once the load is removed. The yield strength is defined as the stress which will produce a small amount of permanent deformation, generally equal to 0.002 or 0.2%. A typical compression test curve of a BMG sample is discussed in section 2.1.5.

Macroscopic compression tests were carried out using an Instron 8562 testing machine with a maximum load of 100 kN under quasistatic loading conditions at room temperature. The compression test samples were prepared from the lateral area of the extruded rods with an aspect ratio of 2:1. Both ends of the specimens were polished to make them parallel to each other prior to the compression test. All the given features are averaged values of at least three samples. Tests were performed by H. Klauss.

Ultrasonic spectroscopy tests: This technique is based on the propagation of ultrasonic waves in the object or material tested. Ultrasonic spectroscopy uses high-frequency sound waves (higher than 20 kHz, the limit of human hearing). In this work, the pulse-echo ultrasonic testing technique was used, in which a signal pulse propagates through a sample due to the vibrations or oscillatory motions of particles within a material.

The sound travels at different speeds in different materials. This is because the mass of the atomic particles and the spring constants are different for different materials. The mass of the particles is related to the density of the material, and the spring constant is related to the elastic constants of a material. The general relationship between the speed of sound V in a solid and its density ρ and elastic constants C_{ij} is given by:

$$V = \sqrt{\frac{c_{ij}}{\rho}}$$ (Eq. 3.4)

This equation may take a number of different forms depending on the type of wave (longitudinal or shear) and on the elastic constants that are used.

This test has been carried out at the University Autònoma Barcelona (UAB) in collaboration with Prof. J. Sort. A normal incidence shear wave transducer (V222-BB-RM from Olympus) with a frequency of 20 MHz was used to generate transverse waves. The longitudinal waves were produced with a Delay line transducer (V208-RM from Olympus) also with a frequency of 20 MHz. The transducers were employed with a panametric pulser- receiver (5072 PR from Olympus) and a digital oscilloscope (model TDS 2022B Textronix) as shown in Fig. 3.2. The

pulser produces an electrical pulse to excite a transducer that converts the electrical input to mechanical energy creating an ultrasonic wave. To provide acoustic coupling between the transducer and the material to be tested, a couplant is almost always necessary to facilitate the transmission of sound energy between the transducer and the test piece. Finally, the transversal and longitudinal signals were recorded and treated using a home-made Labview program. Subsequently, the elastic constants were automatically calculated. The standard formalism for isotropic solids, based on Aleksandrov's method, was employed. The total error of measuring elastic constants is about 5% which include the error of the acoustic measurements (error of the oscilloscope delay time), the error of the sample thickness measurements (normally ± 1 or 2 microns) and the error in density measurements (Archimedes' method) (± 0.02 g/cc).
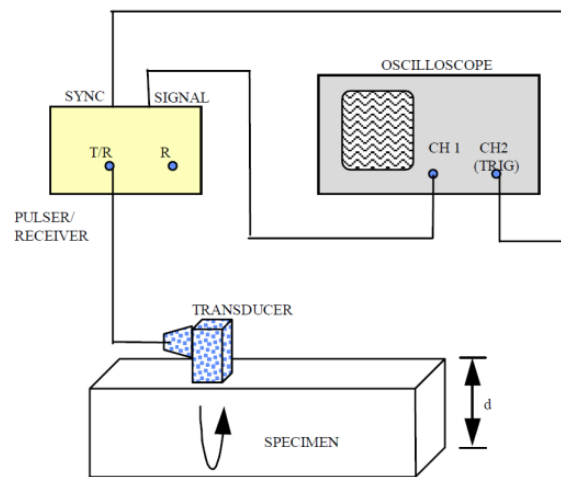

Figure 3.2: Schematic diagram of the components of the ultrasonic testing device.

In this work, samples of 2 mm in diameter and about 2 mm on length were tested, after polishing them to perfect orthogonal geometry. Their densities have been determined by the Archimedes method and the sample dimensions were measured with a digital caliper.

3.4 Corrosion analysis methods

Different electrochemical polarization methods were applied for fundamental corrosion behavior characterization of the $Ti_{75}Zr_{10}Si_{15}$ and $Ti_{60}Zr_{10}Nb_{15}Si_{15}$ alloys in simulated body fluid environment. All measurements were conducted in Ringer solution (8 g/L NaCl, 0.2 g/L KCl,

0.2 g/L CaCl$_2$ and 1 g/L NaHCO$_3$) with pH = 7.4 at 310 K. The electrolyte was purged with N$_2$ for 1 hour before each test.

Potentiodynamic polarization: This technique can provide useful information regarding corrosion rate and susceptibility of specific materials to corrosion in designated environments. It is based on scanning the potential of the working electrode with a defined rate relative to the open circuit potential and monitoring the corresponding current density which is a measure for the total electrode reaction rate at the exposed sample surface (often geometric surface area). The features that can be found on a typical anodic polarization curve are illustrated in Fig. 3.3. It should be stressed that this Figure is an idealized representation of features typically observed in practice. A given polarization curve may have some, but not necessarily all, of the features described below.

As the electrode potential is positively shifted relative to the corrosion potential E$_{corr}$, the current density increases according to active dissolution until a critical value (i$_{crit}$) is reached. In this region, metal oxidation and dissolution is the dominant reaction taking place. This critical point also defines the beginning of the formation of passive films, which occurs at potentials higher than E$_{pass}$ (primary passive potential).

Beyond this point, the current density can decrease by several orders of magnitude to a residual, low, passive current density (i$_{pass}$). At higher potentials breakdown of the passive film might occur with an increase in anodic activity. This increase can be due to a number of phenomena, depending on the alloy/environment combination. For some systems (e.g., aluminum alloys in salt water) this sudden increase in current density may be due to pitting (localized breakdown of passivity), while for others it may be a transpassive dissolution. For metals that form conductive passive layers, passivity breakdown is related with oxygen evolution as conductive film realizes electron-transfer that is needed for water decomposition when the potential of the water stability is reached.
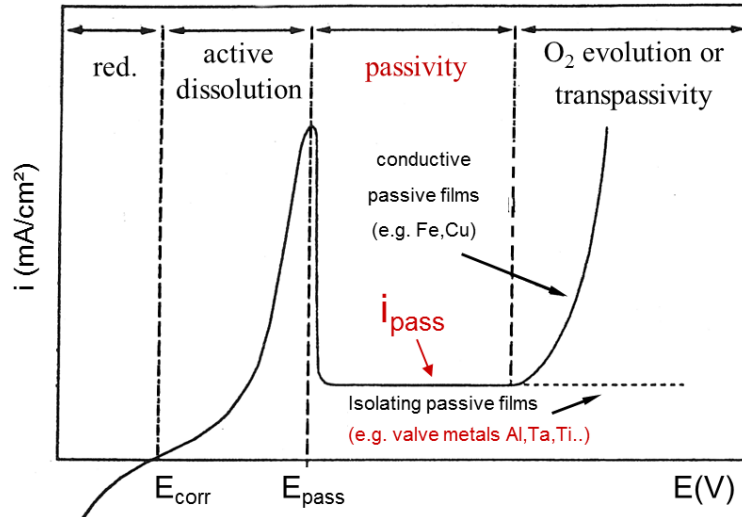
Figure 3.3: Schematic polarization diagram for a passivating electrode, displaying transitions from active corrosion to passive behaviour and to the transpassive state [119].

For metals that form non-conductive barrier-type passive films (like valve metals Al, Ta, Ti, etc.), oxygen evolution or transpassive reactivity is completely suppressed when the film structure is defect-free. The current density remains very low and the passive film further grows.

Potentiostatic polarization (current transient measurements): This method is used to study the anodic passive film growth mechanism in more detail [120]. Valve metals are usually covered by oxide films of the barrier-type which possess electronic and ionic conductivity in dependence on high electric field strength, where equation 3.7 is valid:

$$i = i_0 \exp(\beta \cdot E) \qquad\qquad \text{(Eq. 3.5)}$$

In this case, the mobile ions move only in one direction and every ion which escapes from the metal/oxide interface migrates through the film based on the hopping mechanism and forms additional layers at the oxide/electrolyte interface. Also, oxygen ions (O^{2-}) may be generate and accumulate at the oxide/electrolyte interface and then migrate towards the metal/oxide interface under high field control. The transport number is a measure for the relative migration activity in both directions.

In this mechanism, by assuming that the determining rate is the movement of ions within the oxide and the oxide is considered homogeneous, the field strength E can be calculated from the potential drop ΔU across the oxide and the layer thickness d:

$$E = \frac{\Delta U}{d} \tag{Eq. 3.6}$$

$$i = i_0 \exp(\beta \cdot E) = i_0 \exp(\beta \frac{\Delta U}{d}) \tag{Eq. 3.7}$$

Considering the relation between the thickness of the oxide film and time:

$$\frac{1}{d} = A - B \ln t \tag{Eq. 3.8}$$

under potentiostatic condition, the dependency between current i and time is extracted as:

$$i \sim t^n \tag{Eq. 3.9}$$

where the power of t is obtained from the slope of the potentiostatic current transient measurements curve (a double logarithmic representation) and shown in Table 3.1:

Table 3.1: Different mechanisms of anodic passive film growth

n	Mechanism
-1	High field mechanism (migration)
-0.5	Diffusion
0	Corrosion

Potentiodynamic and potentiostatic polarization tests: They have been performed by means of a Solartron SI 1287 electrochemical interface which was connected to a three-electrode cell with SCE reference electrode (E = 0.241 V vs. NHE) and a Pt net as counter electrode. Measurements were started after 30 min of immersion in the Ringer solution at 37°C under open circuit potential (OCP) conditions and the OCP potential has been recorded vs. time until steady state condition. The dynamic polarization was started from the cathodic regime (-1 V vs. SCE) and linearly swept in the anodic direction at a rate of 0.5 mV/s up to 4V. Anodic current transient measurements were performed by implementing potential steps from the OCP to selected anodic potentials, which were chosen from the potentiodynamic polarization curves.

Cyclic voltammetry: CV is one of the most widely used electroanalytical methods because of its impact for characterizing redox systems. It can be used to analyze any chemical species that can be electrochemically oxidized or reduced. The potential of the electrode which causes the chemical species oxidized or reduced is the controlling parameter. In this method, potential scans run from the starting potential to the end potential at a specific sweep rate (in Volts/sec)

and then reverse from the end potential back to the starting potential and measures the resulting current vs. time curve and can be used for corrosion studies due to their higher scan rates (>>1mV/sec) than linear (quasi-static) polarization, to analyze fast oxide formation and transformation reactions. The measurement starts from OCP or from cathodic pre-reduction potential by scanning the potential with a constant scan rate in the anodic direction and then the reverse scanning towards the starting potential.

For *Cyclic voltammetric measurements*, the alloy samples have been used as rotating disc electrodes implemented in an EG&G Parc Model 616 device which realized a rotation speed of 2000 rpm. After immersion of samples under open circuit potential (OCP) conditions for 30 min and holding at an initial potential of -1.5 V for 60 sec, the potential was swept up to 4 V vs. SCE at a rate of 20 mV/sec in anodic direction and then reversed in cathodic direction up to the initial potential.

Each electrochemical measurement was repeated at least 3 times to ensure a high level of reproducibility.

3.5 Surface analysis methods

A surface analysis of $Ti_{75}Zr_{10}Si_{15}$ and $Ti_{60}Zr_{10}Nb_{15}Si_{15}$ melt-spun ribbons has been firstly done by means of the XPS method in order to determine elemental compositions and oxidation states of the elements in the passive films. Then, for further detailed characterization, depth-profiling was conducted by means of the AES method because of higher sputtering rates and of better defined measuring area selection in comparison with the XPS method.

Both methods are known as surface analysis methods because both, detected electrons which are emitted after the interaction between primary X-rays (XPS) or electrons (AES) and a sample, have relatively low energy. This is giving rise to comparable depth and sensitivity values, which are respectively in the order of nanometers and of about 0.1% atomic concentration. The main difference between the two methods consists in the source of the primary radiation, which is necessary to activate the atoms. In AES an electron gun is used while XPS relies on soft X-rays. As a consequence of that, one of the main differences is the lateral resolution of the two methods. Since there is a continuous evolution in the design of the equipment and the performance of the techniques, it is difficult to express an absolute value for it. But for AES the lateral resolution is typically in the range from 10 to 100 nm, while by means of XPS only a lateral resolution of a few to 100 μm can be reached.

Exprimental

X-ray photoelectron spectroscopy (XPS): The XPS method is a chemical analysis technique that can be used to analyze the surface chemistry of a material. In this technique, the surface of the material is irradiated with a beam of X-rays and the kinetic energy and the number of electrons which escape are simultaneously measured, analyzed and the electron binding energy of each of the emitted electrons can be determined. A typical XPS spectrum is a plot of the number of electrons detected versus the binding energy of the electrons detected. Constituent elements can be determined because each element produces a characteristic set of XPS peaks at characteristic binding energy values. These characteristic peaks correspond to the electron configuration of the electrons within the atoms, e.g., 1s, 2s, 2p, 3s, etc. However, the number of detected electrons in each of the characteristic peaks is directly related to the amount of element within the XPS sampling volume. In principle XPS detects all elements except hydrogen and helium. Detection limits for most of the elements (on a modern instrument) are in the parts per thousand ranges while detection limits of parts per million (ppm) are possible in case of high concentration at top surface or very long collection time [121].

X-ray photoelectron spectroscopy (XPS) measurements has been done at a PHI 5600 CI (Physical Electronics) spectrometer using non-monochromatic Mg-Kα X-rays (350 W) for excitation. A hemispherical analyzer working at pass energy of 29 eV was applied to record the spectra. The analysis area was around 800 μm in diameter. Residual binding energy (BE) shifts from surface charging was corrected by shifting the BE values with respect to the Ti2p peak at 458.8 eV according to TiO_2 [121]. Peak fitting was performed using the PHI-MultiPak software (version 9.3, 2011). XPS analyses were conducted by Dr. S. Oswald.

Auger electron spectroscopy (AES): This method is based on the Auger effect. If an inner shell electron is removed from an atom, an electron from a higher level will quickly make the transition downward to fill the vacancy. If the energy released by the downward transition is given to one of the outer electrons, the electron is then ejected from the atom. The ejected atom's kinetic energy is equal to the energy lost by the electron which made the downward transition minus the binding energy of the electron that is ejected from the atom. In AES the atomic core levels are ionized by the incident electron beam and the resulting Auger electrons are detected with an electron spectrometer. The Auger electron energies and spectrum are characteristic and unique to an atom of a specific element and independent of the incident beam energy [122].

For *Auger electron spectroscopy (AES)* depth profiling measurements a JAMP 9500 F Field Emission Microprobe (JEOL) equipped with a hemispherical analyzer with electron beam

conditions of 10 keV and 10 nA was used. A scanned beam of Ar^+ ions of 1 KeV with the scan size of 1 mm x 1 mm has been used which results in a determined sputtering rate of 4.7 nm/min in silicon oxide. In case of thermally oxidized samples, A scanned beam of Ar^+ ions of 2 keV with the scan size of around 1 mm × 1 mm has been used which results in a sputtering rate of 6.6 nm/min (17 nm/min) determined for silicon oxide.

This sputtering time has been used as a reference for measuring the thickness of oxide films. In such oxide and multicomponent materials oxide reduction and preferential sputtering lead to changes of the surface composition during sputter depth profiling which have to be considered. We used a semi-quantitative correction for this in the depth profiles using internal surface and bulk reference information. Because of peak shape changes this correction procedure was used the non-differentiated Auger; details are described by Oswald et al. [123]. AES analyses were performed by Dr. S. Oswald.

3.6 Thermogravimetric analysis (TGA)

Thermal oxidation which results in the formation of an oxide layer on the surface of a metallic material is used in this work as a surface modification method (see section 2.2.3). One of the common methods used to characterize thermal oxidation processes is the thermogravimetric analysis (TGA).

In this technique the weight (the mass) of a sample is measured by a thermobalance as a function of sample temperature (isochronal) or time (isothermal). Typically, there are two kinds of measurements, dynamic and isothermal measuring in which the sample is heated at a constant heating rate and held at a constant temperature respectively.

A TGA curve comprises data of mass or the percent mass change recorded in dependence on temperature and/or time. The first derivative of this curve presents the rate of the mass change. According to the different reactions during the thermal test such as drying, desorption, adsorption, decomposition and oxidation which may cause loss or gain of the mass, the shape of the curve will change (see Fig. 3.4).

There are different parameters which can affect the TGA data. To produce comparable TGA results, it is necessary to use consistent sample masses and reproducible sample preparation methods. The atmosphere has an important role and can be reactive, oxidizing or inert. Furthermore, the heating rate is essential as the difference between the true sample temperature and the measured one is heating rate dependent. In case of chemical reactions, higher heating

rates cause the onset of chemical reactions to shift to higher temperatures and it is possible that the reaction steps may overlap. Ordinarily, this can be avoided by choosing lower heating rates. The basic model for oxidation was developed in 1965 by Deal and Grove. The Deal–Grove model mathematically describes the growth of an oxide layer on the surface of silicon by thermal oxidation [124].
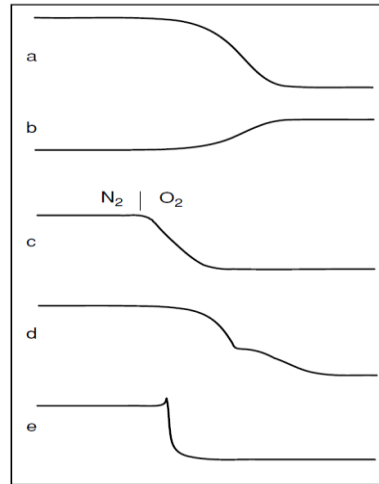

Figure 3.4: TGA curves of different chemical reactions; a) thermal decomposition with the formation of volatile reaction products, b) corrosion, oxidation, c) combustion of carbon black on switching from N_2 to O_2, d) multi-step decomposition, e) explosive decomposition with recoil effect [125].

It has been assumed that an oxide of some thickness x_0 is already present on the Si surface. It has also been assumed that transported species have to go through three steps which are necessary for oxidation on the silicon surface.

1) The flux of the oxidizing gas at the oxide outer surface can be written as:

$$F_1 = h \, (C^* - C_0) \qquad\qquad \text{(Eq. 3.10)}$$

Where h is a gas-phase transport coefficient, C_0 is the oxidant concentration at then surface of oxide and C^* is the oxidant equilibrium concentration in the oxide.

2) Similarly, the flux F_2 representing the diffusion of the oxidant through the oxide to the Si/SiO$_2$ interface can be expressed by using Fick's law as:

$$F_2 = D_{eff} \, (C_0 - C_i)/x_0 \qquad\qquad \text{(Eq. 3.11)}$$

Where C_i is the oxidant concentration near the oxide/Si interface and D_{eff} is the effective diffusion coefficient

3) The third part of the oxidation process is the reaction at the Si/SiO2 interface. It can be represented with a third flux given by:

$$F_3 = kC_i \qquad\qquad \text{(Eq. 3.12)}$$

Under steady-state condition $F_1 = F_2$ and $F_2 = F_3$, as a result the flux F is given by:

$F = F_1 = F_2 = F_3$. Considering N_1 as the number of oxidant molecules in a unit volume of the oxide layer, the growth rate of the oxide layer is described by:

$$dx_0/dt = F/N_1 = kC^*/(1 + k/h + kx_0 + D_{eff})N_1 \qquad\qquad \text{(Eq. 3.13)}$$

By using boundary (at time = 0, $x_i = x_0$) conditions the solution of the above differential equation is written as:

$$x_0{}^2 + Ax_0 = B\,(t + \tau) \qquad\qquad \text{(Eq. 3.14)}$$

The parameters A and B are proportional to the diffusivity and follow an Arrhenius function and τ is the shift in time to account for the initial oxide thickness.

There are two limiting forms of the linear parabolic growth law:

a) For very short oxidation time (thin oxide layer), the rate equation reduced to the linear form: $\qquad\qquad x_0 \approx B/A\,(t + \tau) \qquad\qquad \text{(Eq. 3.15)}$

b) when $t \gg \tau$, the oxide is sufficiently thick, the rate equation reduced to the simple parabolic expression: $\qquad x_0{}^2 \approx B\,(t + \tau) \approx Bt \qquad\qquad \text{(Eq. 3.16)}$

B/A and B are often termed the linear and parabolic rate coefficients respectively, because of the x_0 and $x_0{}^2$ terms in which they appear. Physically, they represent the contribution of fluxes F_3 (interface reaction) and F_2 (oxidant diffusion), respectively. SiO_2 growth on a bare Si wafer usually starts with a linear t_x versus t, which becomes parabolic as the oxide thickens.

Later on, the relationship of the classical linear - parabolic growth law was generalized to the logarithmic growth law [126]. The representative curves can be seen in Fig. 3.5. The linear rate law is applicable to the formation and development of non-protective oxide layers at high temperature while the parabolic rate law assumes that the diffusion of metal cations or oxygen anions is the controlling rate. This law is applicable to uniform, continuous and protective oxide scale layers. A logarithmic growth can be observed for thin oxide scales mainly at low temperatures in which oxidation is fast at the start, and then the rate decreases to a very low value. The slowest process at a given temperature will control the rate of oxidation.
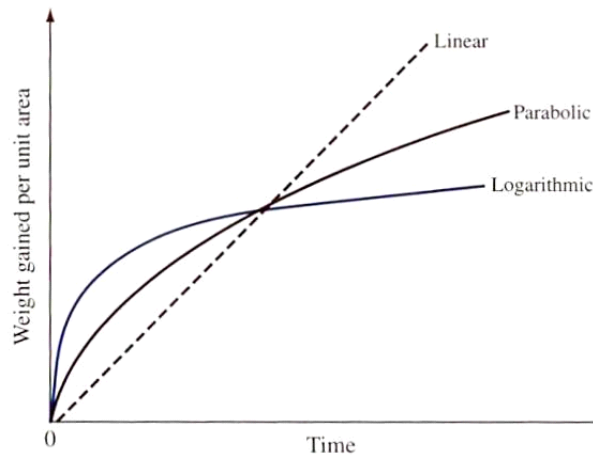
Figure 3.5: Different oxide film growth formation rate curves [125].

Those fundamental oxide scale growth laws have been so far in detail derived for oxidation of crystalline substrates (mainly pure metals). So far, there are no specific studies on the question, to which extend these growth laws are valid for amorphous multicomponent metallic substrates. However, in empirical approaches for characterizing the oxidation behavior of metallic glasses, the fundamental oxide growth laws are employed for the discussion.

In this work, a top loading thermobalance has been used which allows constant positioning of the sample in the furnace during the thermally induced mass changes and their recording. Two crucibles (alumina) are used, one with the sample and the other without it in order to correct the effect of the density changes of the gas during the temperature changes. The blank curve (related to the empty crucible) will be subtracted from the sample curve. The samples (ribbons) were cut in equal sizes (2-3 mm width and 2 cm length) and were cleaned in once in EtOH and twice in de-ionized water for 10 min each in ultrasonic bath (VWR International, Leuven). Finally, it was placed in the crucible with a 45° angle from the bottom of the container.

Thermogravimetric analysis has been done by means of a Netzsch device model STA 449C Jupires. For all experiments, the melt-spun ribbons of $Ti_{75}Zr_{10}Si_{15}$ and $Ti_{60}Zr_{10}Nb_{15}Si_{15}$ produced at overheating temperature of 1993 K have been used. For dynamic TG the samples were continuously heated in the TGA furnace with a heating rate of 10 K/min. The atmosphere was high-purity dry air with a constant net flow rate of 50 ml/min. The oxidized surfaces were characterized with XRD, SEM, TEM, AFM and microhardness methods. The wettability and SBF tests have been performed as a preliminary assessment of the in vivo bone bioactivity of that material. Measurements were conducted by Cornelia Geringswald and the analysis was done with great support from Dr. W. Gruner.

Atomic force microscopy (AFM): In order to investigate the surface topography and roughness, atomic force microscopy (AFM) has been applied. AFM is a high resolution type of scanning probe microscopy (on the order of fractions of a nanometer), in which a sharp tip such as SiN mounted on a cantilever spring at the end of the AFM probe sweeps the surface and monitors its topography [127]. There are several operation modes such as contact mode, non-contact mode and tapping mode. In contact-mode, when the tip is very close to the sample surface (<0.5 nm), the tip deflects back from the surface, due to repulsive force interaction of the electron clouds of the tip and sample atoms. While, in non-contact mode, the tip is attracted towards the sample, at larger tip-sample distances due to long-range Van der Waals forces. In tapping mode (which is used in this work), the cantilever is driven to oscillate up and down near its resonance frequency by a small piezoelectric element mounted in the AFM tip holder similar to the non-contact mode. The interaction of forces acting on the cantilever, when the tip comes close to the surface, Van der Waals forces, dipole-dipole interactions, electrostatic forces, etc. cause the amplitude of this oscillation to decrease as the tip gets closer to the sample. A tapping AFM image is therefore produced by imaging the force of the intermittent contacts of the tip with the sample surface.

In Fig. 3.6, a simplified block diagram of an AFM device is shown. A laser source is used for detection of the cantilever deflection in which the mechanical deflection can be detected by using a 4-quadrant laser photo detector, which usually is covered by a reflective coating such as aluminum or gold. Using piezoelectric movement as a feedback, the distance between the sample and the tip will be controlled by adjusting the amount of deflection due to the interaction force between them [128].
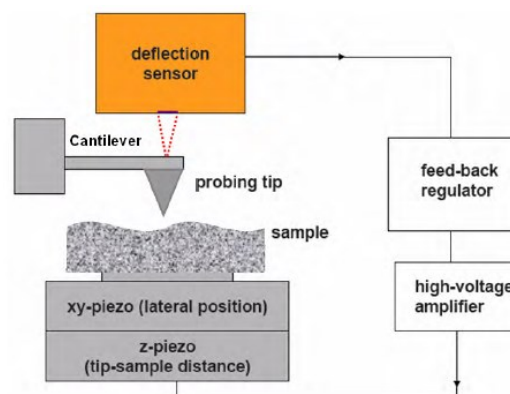

Figure 3.6: Schematic block diagram of AFM [128].

In this work, a Dimension 3100 from Veeco Instrument is used for AFM measurements on the $Ti_{75}Zr_{10}Si_{15}$ and $Ti_{60}Zr_{10}Nb_{15}Si_{15}$ as-spun and thermally treated ribbons. AFM experiments were conducted by Dr. Ulrike Wolff (IFW Dresden).

Microhardness measurements: The Vickers microhardness test has been used to measure the hardness of ribbons before and after thermal oxidation treatment. The basic principle, as with all common measures of hardness, is to observe the desired material's ability to resist plastic deformation. In the Vickers test, the load is applied smoothly, without impact, forcing the indenter (diamond: a 4-sided pyramid) into the test piece. The indenter is held in place for typically 10 or 15 seconds. The physical quality of the indenter and the accuracy of the applied load must be controlled in order to get the correct results. After the load is removed, due to the geometry of the indenter tip, two impression diagonals (*d*) are observed which are measured and averaged. The H_V number is then determined by the ratio *F/A*, where *F* is the force applied to the diamond in kilograms-force and *A* is the surface area of the resulting indentation in square millimeters. *A* can be determined by:

$$A = \frac{d^2}{2\sin(\frac{136°}{2})} \qquad \text{(Eq. 3.17)}$$

which can be approximated by evaluating the sin(136°/2) term to give

$$A \approx \frac{d^2}{1.8544} \qquad \text{(Eq. 3.18)}$$

where d is the average length of the diagonal left by the indenter in millimeters. Hence,

$$H_V = \frac{F}{A} \approx \frac{1.8544F}{d^2} \qquad \text{(Eq. 3.19)}$$

where F is in Kgf and d is in millimeters.

Vickers microhardness was measured on the surface of as-spun and thermally oxidized ribbons using a Shimadzu HVM – 2000 microhardness tester, 30 indents with a constant applied load of 10 g and holding time of 10 s were placed randomly across the sample surface and the mean value and standard deviation were calculated.

Wettability test (Contact angle measurements): The wettability which is defined as the ability of a liquid to maintain contact with a solid surface is evaluated by surface contact angle measurements. The contact angle (θ), as seen in Fig. 3.7, is the angle at which the liquid–vapor interface meets the solid–liquid interface.

As the contact angle decreases, it means the tendency of a drop to spread out over a solid surface raises, the wettability increases. A wettable surface (contact angle <90°) may also be termed hydrophilic and a non-wettable surface (contact angle >90°) hydrophobic [129].

Exprimental

There are different methods of contact angle measurements such as static contact angle, dynamic contact angle and tilting plate method. Static contact angle is perhaps the most common type of measurement, it is a single reading on a static sessile drop shortly after its creation. A static contact angle is captured when a thermodynamic equilibrium is reached between the three phases: solid, liquid, and gas.
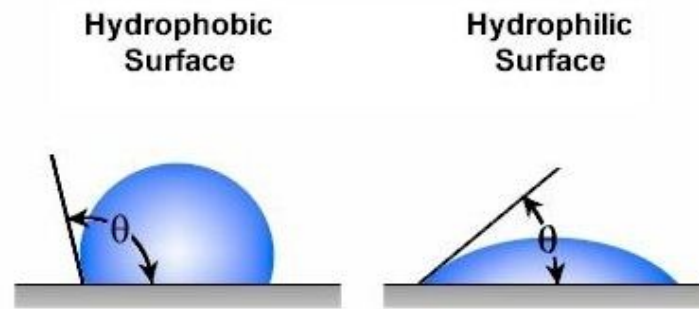

Figure 3.7: Schematic representation of a hydrophobic and a hydrophilic surface.

The water wettability of each sample was determined by sessile drop contact angle (CA) measurements of the advancing water contact angle (θ) using a Theta Lite T101 optical tensiometer (Attension, Biolin Scientific, Finland). The basic elements of an optical tensiometer (also called contact angle meter) include light source, sample stage, lens and image capture. The images are analyzed with a computer software. Four droplets of distilled water were placed at different positions on each sample and the average value is taken as contact angle measure and is presented as mean ± standard deviation.

SBF test: The apatite-forming ability on surfaces of $Ti_{75}Zr_{10}Si_{15}$ and $Ti_{60}Zr_{10}Nb_{15}Si_{15}$ ribbons (as-spun samples and thermally treated ones) was tested in a simulated body fluid (SBF). Its composition which was prepared according to Kokubo and Takadama [130] consisted of NaCl (7.92 g/L), $NaHCO_3$ (0.356 g/L), KCl (0.376 g/L), $Na_2HPO_4.3H_2O$ (0.147 g/L), $MgCl_2.6H_2O$ (0.309 g/L), 1M HCl (15 mL), $CaCl_2$ (0.375 g/L), Na_2SO_4 (0.162 g/L), Tris (6.12 g/L). Firstly, samples were cleaned ultrasonically in ethanol for 15 min and dried at 100°C. Then, they were treated in 10 M NaOH at 60°C for 24 hours to increase their bioactivity. Subsequently, the samples were cleaned with bi-distilled water for a short time and dried in a laminar flow box for 24 hours at room temperature [30]. At the end, they were immersed in SBF solution at 37°C for 10, 20 and 30 days, cleaned three times with bi-distilled water and then dried in a laminar

flow box for 24 hours at room temperature. After this treatment, the surface of samples was investigated with SEM and energy-dispersive X-ray spectroscopy (EDX).

4 Results and discussion

$Ti_{75}Zr_{10}Si_{15}$ and $Ti_{60}Zr_{10}Nb_{15}Si_{15}$ alloys with glass-forming ability have been investigated as promising biomaterials for implant applications from the viewpoint of microstructure, mechanical performance, corrosion and passivation behavior in a synthetic physiological solution. The main focus was on nearly glassy melt-spun ribbons, nevertheless crystalline counterpart samples as well as cp-Ti and Ti40Nb as reference materials have been examined for comparison. In order to increase the bioactivity of the surface of the alloys, thermal oxidation has been applied and the characteristics of the oxidized surfaces have been studied by different methods. Finally, the bioactivity of the modified surfaces has been evaluated by SBF testing.

4.1 Microstructure characterization

4.1.1 Cast crystalline $Ti_{75}Zr_{10}Si_{15}$ and $Ti_{60}Zr_{10}Nb_{15}Si_{15}$ alloys

$Ti_{75}Zr_{10}Si_{15}$ and $Ti_{60}Zr_{10}Nb_{15}Si_{15}$ crystalline rods with 4 mm diameter were produced by copper mold casting and their microstructural state was characterized in detail [131]. The XRD pattern of the cross-sectional area of the $Ti_{75}Zr_{10}Si_{15}$ sample reveals a multi-phase system (Fig. 4.1(a)). This pattern can be indexed by assuming two phases: the hexagonal $(Ti,Zr)_5Si_3$ intermetallic phase and the hexagonal α-Ti phase including also traces of additional non-identified phases. On the other hand, it has been reported for arc-melted Ti-Zr-Si alloys that within the composition range of interest two silicide phases, hexagonal $(Ti,Zr)_5Si_3$ (S1) and $(Ti,Zr)_2Si$ (S2), can form during solidification along with the high temperature β-Ti phase with bcc structure. Upon cooling the latter transforms to a hexagonal α-Ti via solid-state reaction [104,132]. It appears that the formation of the S2 phase is suppressed under the present conditions, which is certainly due to a higher cooling rate realized during Cu mold casting compared to that of arc melting.

A back-scattered SEM image of the cross-sectional area of the $Ti_{75}Zr_{10}Si_{15}$ rod is shown in Fig. 4.1(b). A faceted intermetallic phase is observed as a primary phase surrounded by a disperse eutectic region consisting of α-Ti and S1 in its microstructure. To clarify the composition of each phase, EXD analysis was performed.
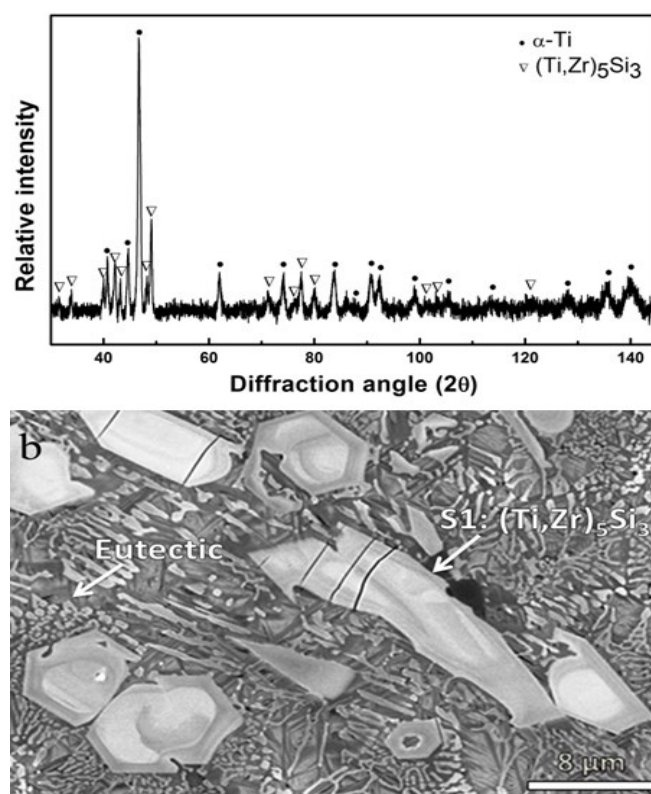
Figure 4.1: X-ray diffraction pattern (a) and back-scattered SEM image (b) taken from a cross-section of a cast $Ti_{75}Zr_{10}Si_{15}$ rod (4mm diameter)

It shows that the average chemical composition of the intermetallic regions is 46 at.-% Ti, 15 at.-%-Zr and 39 at.-%-Si which fits well with the chemical composition of the S1 phase. Figure 4.2(a) represents the XRD pattern taken from the cross-section of the $Ti_{60}Zr_{10}Nb_{15}Si_{15}$ 4 mm rod. In spite of traces of α-Ti, the addition of Nb results in the stabilization of a β-Ti phase at room temperature. In addition, the S1-type phase ($(Ti,Zr,Nb)_5Si_3$) is indexed. Figure 4.2(b) illustrates a SEM image of the microstructure of the $Ti_{60}Zr_{10}Nb_{15}Si_{15}$ rod. Similar to the ternary alloy, the microstructure is composed of an eutectic and an intermetallic S1 phase. The β-phase nucleates on the primary intermetallic phase. Due to the fast growth kinetics (typical for solid solution phases), the β-phase spreads around the primary S1 phase and even starts to develop dendrites (a cellular morphology was found in the microstructure). The residual melt transfers to an eutectic composed of S1- and β-phase.

An EDX analysis revealed that the mean values of element concentrations in the intermetallic phase are 41 at.-% Ti, 13 at.-% Zr, 8 at.-% Nb and 38 at.-% Si which are in good agreement with those of the S1 phase. Elemental EDX mapping is also performed to evaluate the element distribution within the sample.

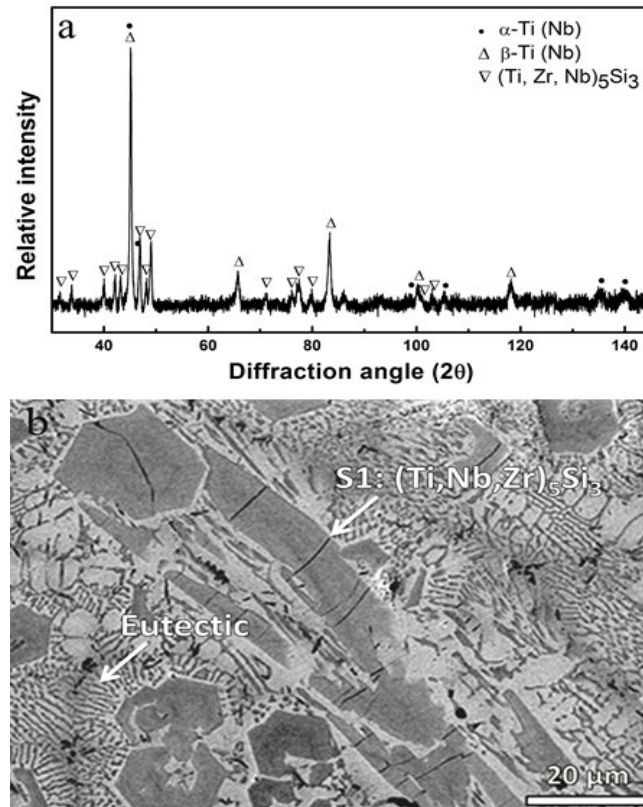Figure 4.2: XRD pattern (a) and back-scattered SEM micrograph (b) taken from a cross-section of a cast $Ti_{60}Zr_{10}Nb_{15}Si_{15}$ rod (4mm diameter).
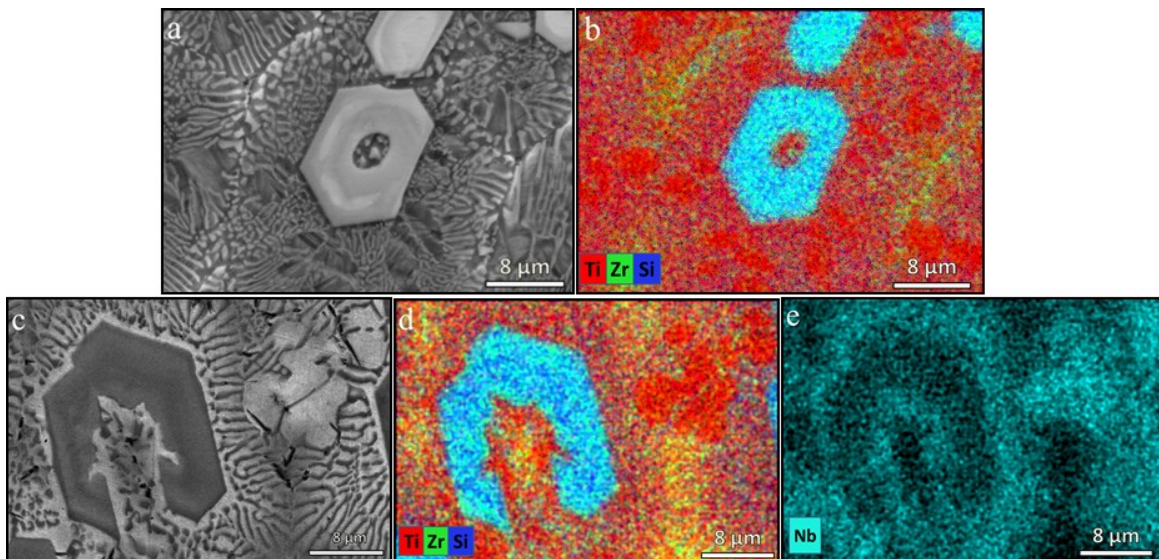

Figure 4.3: SEM/EDX mapping results for rod microstructures of $Ti_{75}Zr_{10}Si_{15}$ (a) secondary electron image (b) elemental (Ti, Zr, Si) map and of $Ti_{60}Zr_{10}Nb_{15}Si_{15}$ (c) secondary electron image (d) elemental (Ti, Zr, Si) map (e) element (Nb) map.

The results which are shown in Fig. 4.3 expose that the addition of Nb increases the inhomogeneity of the element distribution. During solidification Nb is accumulated at the S1-

liquid interface, which is due to its limited solubility in the intermetallic phase. Apparently, the residual liquid does not have sufficient time for homogenization, resulting in a concentration gradient through the eutectic which can be seen in Fig. 4.3(e).

4.1.2 Melt-spun Ti$_{75}$Zr$_{10}$Si$_{15}$ and Ti$_{60}$Zr$_{10}$Nb$_{15}$Si$_{15}$ ribbons

The effect of overheating the melt on the microstructure of melt-spun ribbons has been investigated. In this regard, the cooling rate gradient across the ribbon cross-section has been considered and separately the two different sides of the ribbons have been analyzed.

One is the "air-side" which has a lower cooling rate compared to the other side which is called "wheel-side" and has been in contact with the quenching wheel. Considering the liquidus temperatures of Ti$_{75}$Zr$_{10}$Si$_{15}$ and Ti$_{60}$Zr$_{10}$Nb$_{15}$Si$_{15}$, which are 1620 ± 2 K and 1715 ± 2 K (as determined from DSC analysis), the selected overheating temperatures vary from 1923 K to 2053 K (2053 K was the maximum temperature that could be realized with the experimental set up that was available for melt-spinning).

X-ray diffraction patterns of melt-spun Ti$_{75}$Zr$_{10}$Si$_{15}$ ribbons prepared at different overheating temperatures are shown in Fig. 4.4(a). For each overheating temperature, diffraction patterns were recorded for both the air- and the wheel-side. As a general observation, XRD patterns are composed of sharp peaks superimposed on a diffuse halo indicating the presence of a nanocrystalline phase, identified as bcc β-Ti, dispersed within a glassy matrix phase.

It was also observed that the relative intensities of the β-Ti reflections are stronger in the patterns of the air-side compared to those in the patterns of the wheel-side. The higher cooling rate at the wheel-side of the ribbons obviously retards the β-phase formation and supports vitrification. As the overheating temperature increases from 1923 K to 2053 K, the crystalline reflections reduce in intensity for both ribbon sides, indicating that the volume fraction of the nanocrystalline β-Ti phase is reduced.

According to the XRD patterns, the Ti$_{75}$Zr$_{10}$Si$_{15}$ sample that was quenched from the maximum overheating temperature of 2053 K has a fully amorphous structure on the wheel-side. However, reflections corresponding to nanocrystalline β-Ti are still present in the XRD pattern of the air-side of the ribbon.
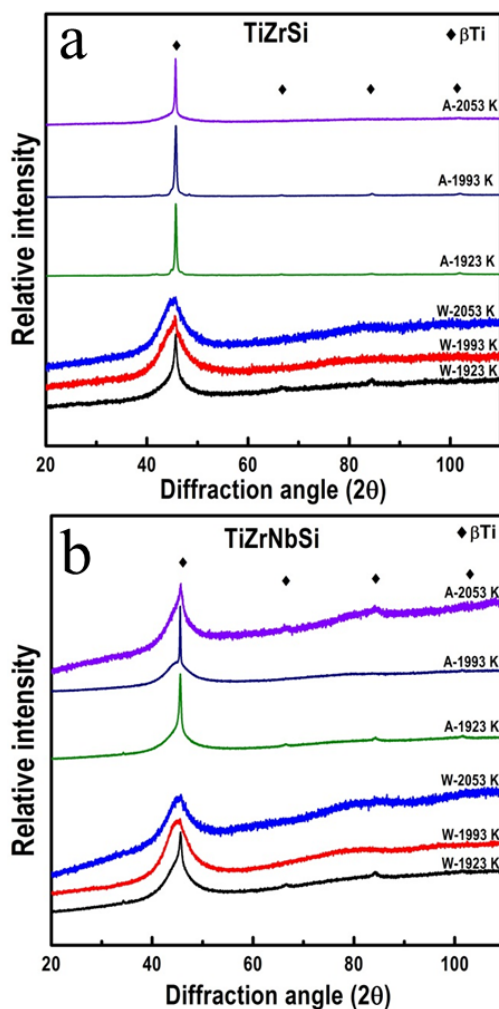
Figure 4.4: XRD patterns corresponding to the air- (A) and wheel- (W) sides of (a) $Ti_{75}Zr_{10}Si_{15}$ and (b) $Ti_{60}Zr_{10}Nb_{15}Si_{15}$ melt spun ribbons prepared by using different overheating temperatures of the melt.

Similar trends in the phase evolution were observed for melt-spun $Ti_{60}Zr_{10}Nb_{15}Si_{15}$ ribbons (Fig. 4.4(b)). When increasing the overheating temperature, a decrease of the intensities of the XRD reflections of the crystalline phase was detected for both sides of the ribbons. Apparently, the addition of Nb increases the fraction of the glassy phase and consequently, the XRD patterns taken from the wheel-side of the ribbons that were melt-spun at 1993 K and 2053 K, show completely amorphous features. However, even at the highest melting temperature (2053 K), a minor volume fraction of bcc β-Ti nanocrystals may exist in the glassy matrix, which is not detectable by XRD.

TEM studies have been conducted in order to more accurately investigate the phase evolution. Figure 4.5 illustrates TEM results of the air- and wheel-side of ternary alloy samples produced by melt-spinning at an overheating temperature of 1993 K.
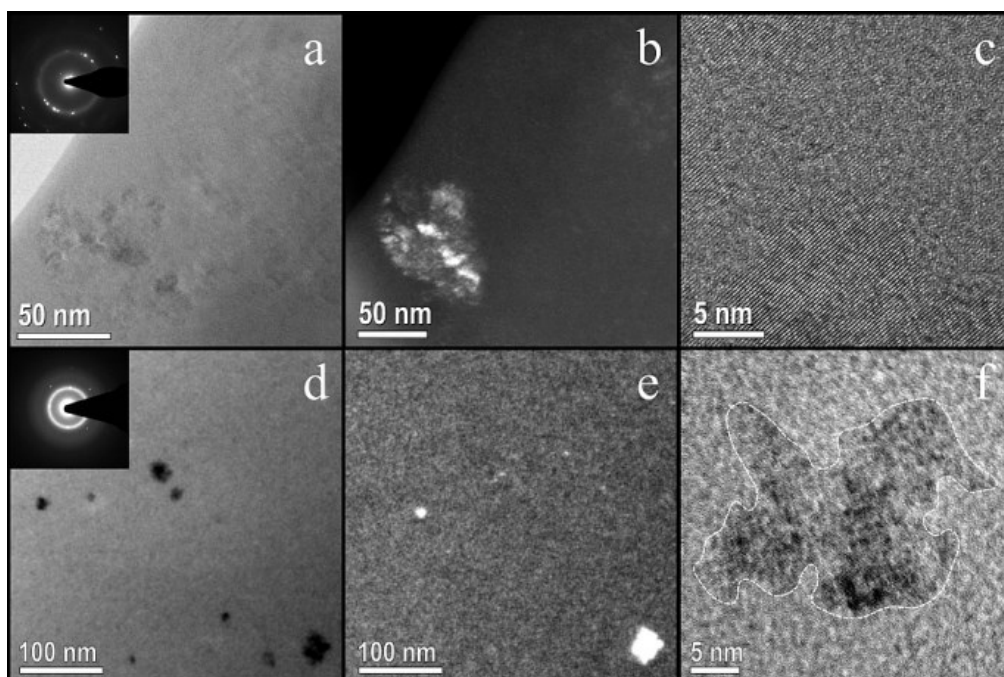

Figure 4.5: (a) Bright field, (b) dark field and (c) high resolution TEM micrograph of the wheel-side, (d) bright field, (e) dark field and (f) high resolution TEM micrograph of the air-side of a $Ti_{75}Zr_{10}Si_{15}$ ribbon; the ribbon is quenched from 1993 K.

According to the bright-field (BF) images displayed in Fig. 4.5(a, d), the structural state of the wheel- and air-sides of the $Ti_{75}Zr_{10}Si_{15}$ alloy is a mixture of nanocrystals embedded in an amorphous matrix. The two-phase nature is confirmed by the SAED patterns displayed as an inset in the BF image which shows the diffuse rings of an amorphous phase together with Bragg reflections corresponding to crystalline precipitates. Indexation of the Bragg reflections showed that their position matches well with the ring pattern of β-Ti. The interface between amorphous matrix and β-Ti nanocrystalline regions is illustrated well in the high-resolution image (Fig. 4.5(f)). TEM studies reveal that the air-side contains a higher fraction of nanocrystals in comparison with the wheel-side which is in agreement with the results from XRD analysis. The distribution of the size of the nanocrystals is from about 10 to 50 nm.
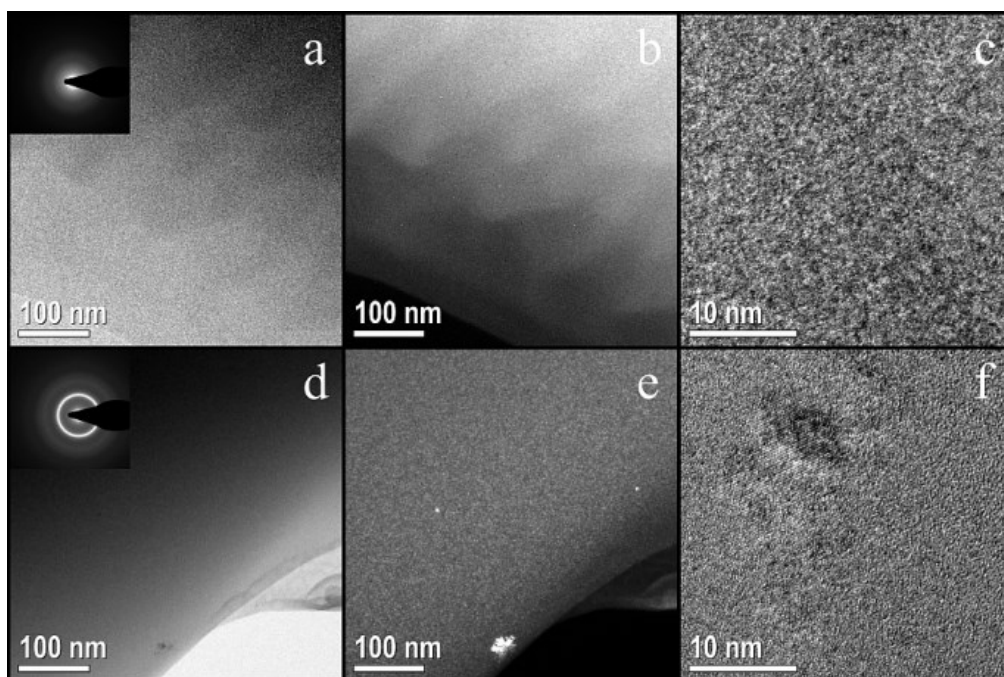
Figure 4.6: (a) Bright field, (b) dark field and (c) high resolution TEM micrograph of the wheel-side, (d) bright field, (e) dark field and (f) high resolution TEM micrograph of the air-side of a $Ti_{60}Zr_{10}Nb_{15}Si_{15}$ ribbon; the ribbon is quenched from 1993 K.

Figure 4.6 shows the TEM results of the air- and wheel-side of quaternary alloy. No crystalline precipitates were found in the wheel-side of $Ti_{60}Zr_{10}Nb_{15}Si_{15}$ ribbons produced at the same overheating temperature of 1993 K (Fig. 4.6(a-c)). According to the BF and high-resolution TEM micrographs (Fig. 4.6(a) and 4.6(c), respectively), as well as confirmed by the SAED diffraction pattern (inset of Fig. 4.6(a)), the wheel-side of the ribbon is fully amorphous. Nevertheless, some traces of β-Ti nanocrystals can be found on the air-side of the ribbon. These results clearly show that the substitution of 15 at.-% Ti with Nb improves the GFA of the $Ti_{75}Zr_{10}Si_{15}$ alloy.

The effect of the overheating temperature on the structure evolution of melt-spun ribbons can be discussed considering different aspects. Increasing this temperature results in a better homogenization of the melt, including a complete melting of high temperature phases present in the multi-phase crystalline pre-alloy, which could act as nucleation agents during rapid cooling. Also, the overheating temperature affects the cooling rate within the ribbon.

It has been reported that by increasing this temperature, the cooling rate is decreased and hence, causes an increase of the crystalline volume fraction [133]. Tkatch et al. [134] reported the same trend in $Fe_{40}Ni_{40}P_{14}B_6$ ribbons and it was attributed to an increase of the roughness at the wheel-side of the ribbon [134,135]. Increasing the surface roughness of $Fe_{64}Co_{21}B_{15}$ by

increasing the melting temperature was also stated by Ferrara et al. [135]. However, as it was observed for the Ti(-Nb)-Zr-Si system, a decrease of the nanocrystalline volume fraction occurs when increasing the overheating temperature. So it seems that the sensitivity to a variation of the cooling rate is not pronounced. Consequently, the results strongly suggest that a more homogenized melt and therefore, a lower fraction of heterogeneous nucleation sites is the main factor determining the microstructural differences when the overheating temperature is varied.

Summary: The $Ti_{75}Zr_{10}Si_{15}$ and $Ti_{60}Zr_{10}Nb_{15}Si_{15}$ melt-spun ribbons with thickness values of 30-50 μm exhibit a nanocomposite structure of β-Ti nanocrystals being embedded in a glassy matrix. In contrast, their crystalline counterparts obtained by casting with slower cooling rate (4 mm diameter rod samples) have crystalline multiphase microstructures. In case of the ternary alloy, the microstructure of a crystalline rod consists of the S1 $((Ti,Zr)_5Si_3)$ intermetallic phase and an eutectic of S1 and α-Ti phase. The Nb addition in case of the quaternary alloy yields a microstructure comprising the S1 $((Ti,Zr,Nb)_5Si_3)$ phase and an eutectic of S1 and β-Ti(Nb) phase.

Concerning the melt-spun ribbons, the results reflect also a cooling-rate-dependent microstructural gradient over the ribbon cross-section. Nanocrystalline β-Ti is mainly precipitated in the glassy matrix at the air-side due to the local lower cooling rate. Increasing the overheating temperature results in an increase of the amorphous phase fraction over the ribbon cross-section. Adding Nb to create the $Ti_{60}Zr_{10}Nb_{15}Si_{15}$ alloy increases the glass-forming ability of the system, as expressed in an increase of the amorphous phase fraction at both sides of the ribbon. A a maximum overheating temperature of 2053 K, a nearly fully glassy structure is obtained. From the thermodynamic and structural point of view [16] the $Ti_{75}Zr_{10}Si_{15}$ and the $Ti_{60}Zr_{10}Nb_{15}Si_{15}$ alloys have the ability to stabilize a fully glassy state. But the experimental conditions of the real melt-spinning process, in particular, the maximum realizable temperature of the melt, that determines its homogeneity, limits a reproducible adjustment of a fully glassy state. It supports precipitation of nanocrystalline phase fractions which are embedded in a glass-matrix. Therefore, these melt-spun alloys are described in the following as "nanocomposite" alloys.

4.2 Mechanical characterization of crystalline and nanocomposite alloys

The mechanical properties of cast microcrystalline $Ti_{75}Zr_{10}Si_{15}$ and $Ti_{60}Zr_{10}Nb_{15}Si_{15}$ samples were investigated by means of compression testing, acoustic measurements and nanoindentation testing [131].
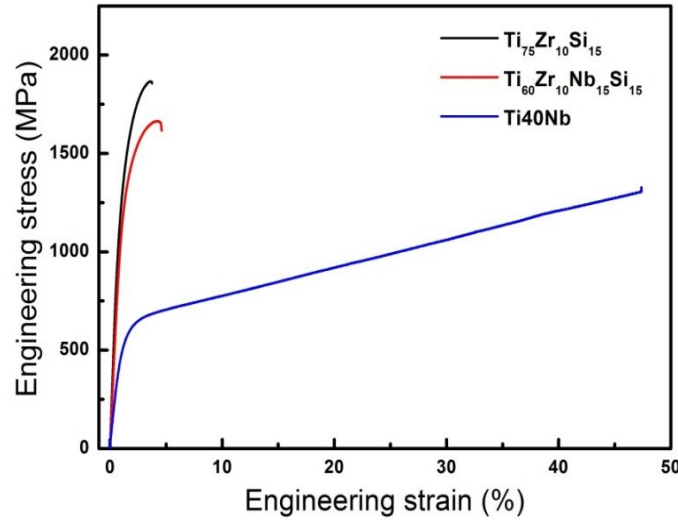

Figure 4.7: Representative room temperature compression engineering stress-engineering strain curves for cast crystalline $Ti_{75}Zr_{10}Si_{15}$ and $Ti_{60}Zr_{10}Nb_{15}Si_{15}$ alloy samples; reference cast β-type Ti-40Nb.

Table 4.1: Experimental data of Young's modulus (E), Yield Strength (σ_y), compressive strength (σ_{db}) and plastic elongation (ε_p) for compression tests of $Ti_{75}Zr_{10}Si_{15}$, $Ti_{60}Zr_{10}Nb_{15}Si_{15}$ and β-type Ti-40Nb.

	E (GPa)	σ_y (MPa)	σ_{db} (MPa)	ε_p (%)
$Ti_{75}Zr_{10}Si_{15}$- Rod	150 ± 15	1231 ± 41	1871 ± 6.3	2.7 ± 0.1
$Ti_{60}Zr_{10}Nb_{15}Si_{15}$- Rod	120 ± 7	1185 ± 32	1684 ± 27	3 ± 0.2
Ti-40Nb ($Ti_{74.4}Nb_{25.6}$)	62 ± 7	544 ± 66	1070 ± 190	28 ± 7

Mean values of Young's modulus, ultimate stress and plastic elongation obtained by means of compression tests are summarized in Table 4.1, and representative curves are shown in Fig. 4.7. β-type Ti-40Nb was employed as reference material due to its desirable characteristics for biomedical implant applications.

Both investigated crystalline alloys exhibit a similar high yield strength (around 1200 MPa), which is much higher than that of Ti-40Nb measured under similar conditions and which is

desirable for specific load-bearing implant applications. Besides, a high ultimate stress, i.e. over 1800 MPa for the ternary alloy and over 1600 MPa for the Nb-containing alloy, is obtained. With the addition of Nb, Young's modulus decreases from about 150 GPa to a value comparable to that of the commercial (α+β)-type Ti-based implant alloy Ti-6Al-4V which is about 120 GPa [136]. Nevertheless, the obtained value is much higher than the Young's modulus of β-type Ti-based alloys such as Ti-40Nb ($Ti_{74.4}Nb_{25.6}$) with about 60 GPa.

However, the addition of Nb to the ternary alloy does not significantly affect the compressive plasticity, which is considerably lower than that of Ti-40Nb. Ultrasonic measurements were performed to provide more accurate values of Young's modulus for the crystalline alloys, as compared to those from compression tests. It is due to the fact that the elastic regime during compressive loading is often identified only with difficulty. Besides, if the surfaces are not perfectly flat and parallel, a curvature or changes in the slope of the compression test curve in the linear elastic part can occur. These effects may cause a relatively large error to be around ±10 GPa. For the crystalline alloys a good agreement is observed between Young's modulus obtained from both methods. Interestingly, similar to the compression test results, adding Nb decreases Young's modulus significantly from 155.7 ± 1.5 GPa for $Ti_{75}Zr_{10}Si_{15}$ to 116.8 ± 2.5 GPa for $Ti_{60}Zr_{10}Nb_{15}Si_{15}$.

Nanoindentation tests were carried out to measure the mechanical properties of the melt-spun ribbons as well as the crystalline counterparts under the same conditions in order to be able to compare the results. In addition, the mechanical properties of the single phases constituting the microstructure of the rods have been investigated. The average value of hardness calculated from a series of nanoindentation tests on a sample cross-section is larger for the $Ti_{75}Zr_{10}Si_{15}$ alloy than that for the $Ti_{60}Zr_{10}Nb_{15}Si_{15}$ alloy (see Table 4.2).

Table 4.2: Hardness, reduced modulus and H/ E_r results, measured by nanoindentation

	H (hardness, GPa)	E_r (reduced modulus, GPa)	H/ E_r
$Ti_{75}Zr_{10}Si_{15}$- rod	12.2 ± 0.2	176.6 ± 1.1	0.069
$Ti_{75}Zr_{10}Si_{15}$- ribbon 2053 K	10.2 ± 0.1	123.1 ± 0.5	0.083
$Ti_{75}Zr_{10}Si_{15}$- ribbon 1923 K	8.98 ± 0.5	117.5 ± 4.6	0.076
$Ti_{60}Zr_{10}Nb_{15}Si_{15}$- rod	8.9 ± 0.3	143.6 ± 2.9	0.062
$Ti_{60}Zr_{10}Nb_{15}Si_{15}$- ribbon 2053 K	8.8 ± 0.2	108.01 ± 1.4	0.084
$Ti_{60}Zr_{10}Nb_{15}Si_{15}$- ribbon 1923 K	8.52 ± 0.1	113.0 ± 1.9	0.075
Ti-40Nb ($Ti_{74.4}Nb_{25.6}$)	2.8 ± 0.1	77.8 ± 4.6	0.036

This is in agreement with the results from macroscopic compression tests in which the yield stress indicates the same trend. With the Nb addition, the hardness decreases which can be attributed to the presence of a larger fraction of bcc β-type phase in the $Ti_{60}Zr_{10}Nb_{15}Si_{15}$ alloy, which is typically softer than the hexagonal α-phase due to the larger number of slip planes and slip directions. In addition, Young's modulus is usually lower for a β-phase than for an α-phase, which is in agreement with the obtained results (Tables 4.1 and 4.2, Fig. 4.7). The reduced Young's modulus of the $Ti_{60}Zr_{10}Nb_{15}Si_{15}$ alloy is larger than that of Ti-40Nb, but the hardness of the latter is considerably lower. Furthermore, in the single-phase nanoindentation analysis the presence of Nb in the intermetallic S1 phase of the crystalline $Ti_{60}Zr_{10}Nb_{15}Si_{15}$ alloy was found to decrease E_r locally as compared to the value for S1 in the $Ti_{75}Zr_{10}Si_{15}$ sample (see Table 4.3). This is to some extent expected since the Young's modulus of Nb is lower than that of Ti.

Table 4.3: Hardness, reduced modulus and H/ E_r measured by nanoindentation in the intermetallic phase and the eutectic matrix of crystalline $Ti_{75}Zr_{10}Si_{15}$ and $Ti_{60}Zr_{10}Nb_{15}Si_{15}$ alloy samples.

	$Ti_{75}Zr_{10}Si_{15}$		$Ti_{60}Zr_{10}Nb_{15}Si_{15}$	
	Intermetallic S1 phase	Eutectic	Intermetallic S1 phase	Eutectic
H (hardness, GPa)	13.7 ± 1.6	11.8 ± 0.37	8.85 ± 1.9	8.1± 0.63
E_r (reduced modulus, GPa)	215 ± 11.2	172.7 ± 2.3	156.1 ± 7.7	129.4 ± 3.9
H/ E_r	0.064	0.068	0.057	0.063

Figure 4.8 exemplarily shows the load-displacement (P-h) nanoindentation curves for the intermetallic phase and the eutectic regions of a cast $Ti_{75}Zr_{10}Si_{15}$ sample and of selected regions of the nanocomposite structure at the cross-section of its ribbons produced at overheating temperatures at 1923 K and 2053 K. The curves related to the ribbons are serrated by a series of discrete steps (pop-ins). These pop-ins in the P-h curve correspond to shear band nucleation and propagation during the indentation as previously suggested [137,138].
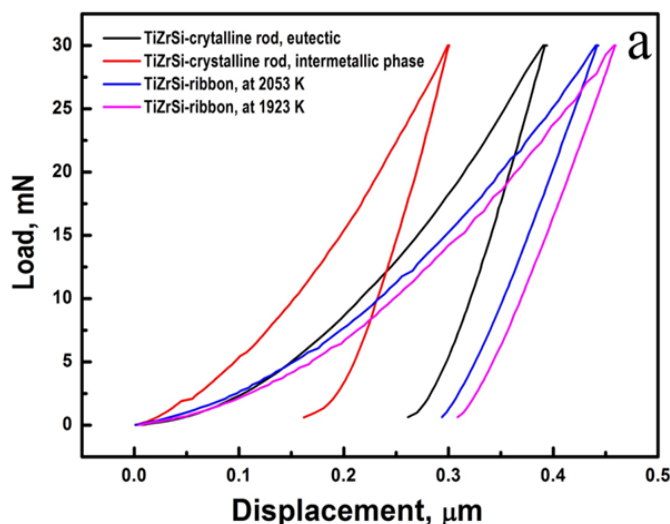
Figure 4.8: Representative load-displacement nanoindentation curves measured for $Ti_{75}Zr_{10}Si_{15}$ samples: the intermetallic and eutectic regions of the crystalline rod and a selected region of nanocomposite ribbons prepared using two overheating temperatures.

Concerning the ribbons, their H and E_r values are lower than for the rods with the same composition, reaching Young's modulus values of about 123 GPa for $Ti_{75}Zr_{10}Si_{15}$ and of about 108 GPa for $Ti_{60}Zr_{10}Nb_{15}Si_{15}$, which are similar to those of commercial cp-Ti (~112 GPa) and Ti-6Al-4V (~120 GPa [139]). Instead, hardness values are three times larger than those of commercial reference materials (Ti≈2.7 GPa, Ti6Al4V≈4 GPa [37]) (see Table 4.2). This is ascribed to the presence of the glassy structure in the matrix of the ribbons as it has been shown that metallic glasses often exhibit lower Young's modulus values than the crystalline materials with analogous compositions [140-142]. Evidence for a reduction of the elastic constant accompanying the loss of long-range order was also reported during amorphisation of a Zr_3Al glass by ion irradiation [143] or in Pd-based, Zr-based or rare-earth metallic glasses when compared to their fully crystallized counterparts [140-142]. This effect has been referred to as "elastic softening", which has been attributed to static atomic displacements and anharmonic vibrations resulting from the chemical and topological disorder of the metallic glass as well as to quenched-in free volume in the glass structure [141]. Although the difference in the H and E_r for the different investigated ribbons is not very pronounced, there is a clear trend, particularly for the H values, to increase with higher overheating temperature. This can be due to the reduction of the fraction of soft β-phase in the ribbons when prepared at a higher overheating temperature. An effect of the Nb addition on the nano-mechanical properties of the melt-spun ribbons could not be clearly identified in the error limit of the method, despite the finding that Nb tends to improve the glass-forming ability.

Summary: Mechanical property investigations revealed that Nb has the main effect of decreasing Young's modulus of the crystalline formula alloy as well as its hardness which is due to the stabilization of a significant fraction of a β-type phase. For the melt-spun ribbons the only possible mechanical testing method, nanoindentation, has been applied. It reveals that, while their Young's modulus values are similar to those of commercial cp-Ti and Ti-6Al-4V, their hardness values are three times larger.

Finally, the ratio H/E_r, which gives an indirect assessment of the wear resistance [144-146], is much larger for all the investigated alloys as compared to this ratio for commercial cp-Ti or Ti-40Nb (Table 4.2). Particularly large values of H/E_r are obtained for the glassy ribbons. All these combinations of mechanical properties, i.e. large H, relatively low E_r and high H/E_r ratio, indicate the potential of the investigated alloys to be used for specific biomedical applications under load-bearing conditions.

4.3 Electrochemical behavior

4.3.1 Cyclic voltammetry

Cyclic voltammetry (CV) has been applied in order to acquire qualitative information about principal anodic oxidation reactions. The cyclic voltammograms (CVs) for $Ti_{75}Zr_{10}Si_{15}$ and $Ti_{60}Zr_{10}Nb_{15}Si_{15}$ alloys, the metallic constituent elements and Ti-40Nb are measured. All measurements were carried out in Ringer solution at 37°C with a potential scan rate of 20 mV/sec in the range from -1.5 to 4 V vs. SCE. Although the potential of 4 V is far from the expected potential in a biomedical application, the potential range has been expanded beyond the water stability limit (~1.2 V) in order to explore the electron permeability of the forming passive film. After the establishment of the OCP, the samples were firstly cathodically polarized up to -1.5 V for a pre-reduction of the electrode surface. In Fig. 4.9, CV curves for Ti, Zr, Nb and Ti-40Nb are summarized.
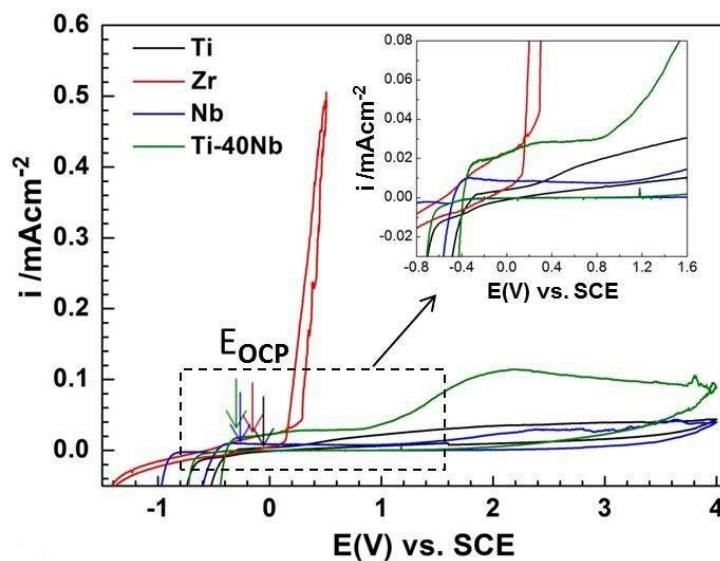
Figure 4.9: Anodic sections of cyclic voltammograms of a) Ti, Zr and Nb and β-type Ti-40Nb ($Ti_{74.4}Nb_{25.6}$) recorded in Ringer solution (pH 7.4, T = 37°C), at ν = 20 mVsec^{-1} and ω = 2000 min^{-1}.

The behavior of the Ti in simulated body fluids is well studied [147,148]. Also, Nb and Zr were investigated to better understand the alloy behavior. The OCP values for Ti and Nb adjust at -0.274 V and -0.276 V vs. SCE, respectively. Ti and Nb show the same trend. Even in Ringer solution with high chloride concentration both elements exhibit a typical valve-metal behavior in a wide potential range, i.e. a very low anodic reactivity due to a formation of barrier-type passive films [120]. After pre-reduction of Ti and Nb surfaces, a slight increase of the current density in the anodic regime at about -0.6 V up to ~9 μA/cm^2 occurs. Then another rise of the current density to a plateau value of ~19 μA/cm^2 follows at ~0.4 V vs. SCE for Ti and at ~1.2 V vs. SCE for Nb. For Ti a current increase at − 0.6 V vs. SCE can be associated with the formation of Ti^{3+}-species as films of TiOOH and Ti_2O_3. Also, the initial anodic current increase may be attributable to the oxidation of adsorbed hydrogen at the metal surface that can have formed during cathodic pre-polarization. With a further increase of the potential to 0.4 V vs. SCE and higher, the surface film composition changes from Ti^{3+}- to Ti^{4+}- species corresponding to TiO_2 formation. A nearly constant current density level up to 1.5 V vs. SCE refers to a thickening of the film consisting of TiO_2 and Ti_2O_3 [147].

The anodic behavior of Nb is initially governed by the formation of NbO (Nb^{2+}) and NbO_2 (Nb^{4+}) oxides at -0.6 V vs. SCE (besides possible hydrogen oxidation). Upon further polarization to 1.2 V vs. SCE these sub-oxides partially transform to Nb_2O_5 (Nb^{5+}) which has been identified to be highly disordered [149,150]. A further slight rise of the anodic current

density from around 1.5 V vs. SCE observed for both Ti and Nb indicate a weak reactivity for water decomposition which can be due to limited electron transfer through the rapidly grown defective thin oxide films. However, sweeping to higher anodic potentials results also in further surface film growth.

Unlike Ti and Nb, Zr shows a limited corrosion resistance in Ringer solution. The OCP value establishes at -0.194 V vs. SCE and after pre-reduction only a short region of anodic passivity is observed before it undergoes active dissolution at around 0.2 V with a sudden increase of the current density [151] which is a typical behavior of pitting events.

The CV of Ti-40Nb is quite similar to that of Ti and Nb in the measured potential range. The anodic polarization leads to the formation of sub-oxides of Ti and Nb. These sub-oxides are then partly transformed to oxides with a more stable higher valence state at about 0.2 V vs. SCE. The anodic step starting at ~1.2 V vs. SCE is attributed to a limited oxygen evolution from water-decomposition. Metikos-Hukovic et al. [152] stated that an addition of Nb to a Ti alloy instead of V leading to ($\alpha+\beta$) Ti6Al6Nb improved markedly the passive film stability. The beneficial effect of Nb is attributed to an annihilation of anion vacancies in the crystal lattice of the TiO_2 passive film, which occur due to the presence of lower oxidation states (Ti^{2+}, Ti^{3+}). Thus, Nb makes the passive oxide film more stoichiometric. However, in the anodic section of the CV for Ti-40Nb at potentials >1.2 V vs. SCE a higher current density level than for the single constituents is measured. This may be attributed to a more pronounced distortion of the structure of the rapidly and inhomogeneous growing passive film on the alloy, which enables an enhanced transfer or tunneling of electrons which is needed for the water decomposition reaction.

The Pourbaix diagram of Si [54] reveals that, at a pH value of 7.4 (pH value of the Ringer solution) and at potentials up to 1.4 V (potential of the water stability), SiO_2 is stable and can therefore be present as passive film on a Si surface. Although the effect of anions such as chlorides is not included in these calculated thermodynamic diagrams, XPS results, which will be discussed later, confirm that in the Ringer solution and under anodic conditions oxidic Si species (Si^{4+}) are present in passive films on Si-containing alloy surfaces. In summary, CV studies on pure metallic constituent elements and also on Ti-40Nb used as a reference reveal that in Ringer solution under anodic conditions except for Zr, all others exhibit a very stable passive behavior in a wide potential range without any indication for pitting.

Figure 4.10 shows the cyclic voltammograms of $Ti_{75}Zr_{10}Si_{15}$ and $Ti_{60}Zr_{10}Nb_{15}Si_{15}$ prepared as multiphase micro-crystalline cast rods and as homogenized melt-spun ribbons with nearly fully glassy state. The overall electrochemical behavior of all the alloy samples is similar to that of

pure Ti and Nb as well as of β-Ti-40Nb in the potential range up to ~1.2 V, i.e. a spontaneous stable passivation due to barrier-type oxide film formation. In detail, an initial slight increase of the anodic current density due to sub-oxide formation occurs at an anodic potential of ~-0.6 V vs. SCE. Further, another slight increase of current density values at around 0.1 V vs. SCE is described as being a consequence of oxide transformations to higher valence states and thickening of the oxide film up to the potential of the water stability limit [152].
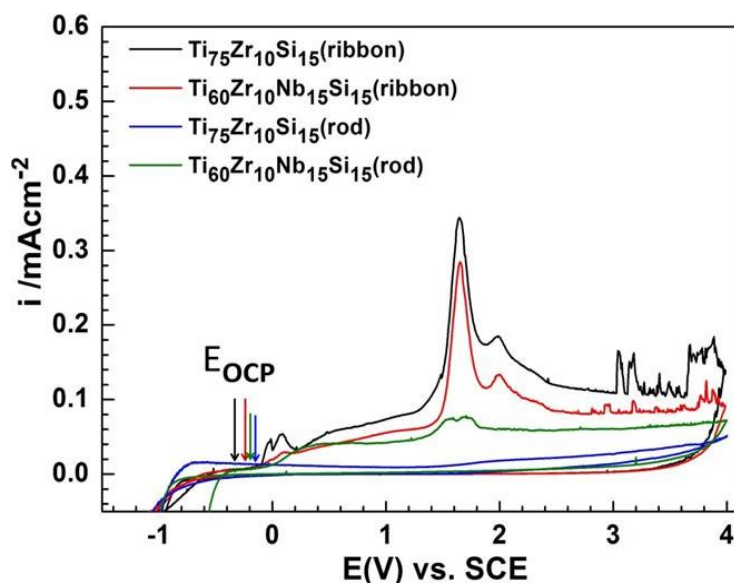
Figure 4.10: Anodic sections of cyclic voltammograms of a $Ti_{75}Zr_{10}Si_{15}$ rod, a $Ti_{60}Zr_{10}Nb_{15}Si_{15}$ rod, a $Ti_{75}Zr_{10}Si_{15}$ ribbon and a $Ti_{60}Zr_{10}Nb_{15}Si_{15}$ ribbon, recorded in Ringer solution (pH 7.4, T= 37°C), at $v = 20mVsec^{-1}$ and $\omega = 2000\ min^{-1}$.

The additionally observed small peaks for a $Ti_{75}Zr_{10}Si_{15}$ ribbon at ~0.1 V vs. SCE, which are at the same potential range as the initial pitting potential of Zr, can be attributed to temporary pitting initiation due to the Zr fraction in the alloy. But those events appear to be further suppressed by growing the oxide film layer.

In the curve of the crystalline $Ti_{60}Zr_{10}Nb_{15}Si_{15}$ alloy a small peak of the current density at about 1.5 V is caused by a limited temporary electron-transfer for the water decomposition. But upon further increasing the potential, the current density establishes itself at another low plateau indicating a further stable film growth [152]. Under the conditions of a CV measurement, the anodic behavior of the multiphase $Ti_{60}Zr_{10}Nb_{15}Si_{15}$ alloy is very similar to that of the single-phase β-type Ti-40Nb reference alloy (with 25.6 at.-% Nb). Melt-spun ribbons of $Ti_{60}Zr_{10}Nb_{15}Si_{15}$ show a similar anodic behavior like the ternary alloy but a lower overall

current density level, indicating enhanced corrosion protection. As it has been discussed before, the addition of Nb to a Ti alloy can improve the corrosion stability.

Further characteristic features in the anodic regimes of the CVs of the melt-spun ribbons are sharp peaks at ~1.6 V vs. SCE and subsequent smaller peaks at ~2 V vs. SCE. In the measurements on the cross sections of the crystalline counterpart rods these peaks are not so pronounced. They are attributed to a possibly beginning electron-transfer reaction that enables water decomposition under oxygen evolution which is, upon further polarization, inhibited by an enhanced oxide growth. Also, for measurements on ribbon samples, current density fluctuations are observed at potentials above 3 V, which suggest a metastable breakdown of passivity. It is reasonable to assume that these features are artifacts that must be attributed to the sample geometry. The thin ribbons have sharp edges which cause a very inhomogeneous distribution of the electric field lines at the electrode surface that is exposed to the solution with a densification of the field lines at the sample edges. In addition, passive film formation at those sharp edges is quite difficult. Both aspects give rise to the enhanced reactivity at those edge regions with consequences for the integral response of the whole electrode. Further insight into the composition of the anodic oxide films has been gained by XPS studies which will be discussed later.

4.3.2 Potentiodynamic polarization

Quasistatic linear polarization curves were recorded in Ringer solution at 37°C (Fig. 4.11). For the different materials tested in this study, one representative curve was selected after many repeated measurements. All investigated Ti-based systems show spontaneous passivity even in a highly concentrated chloride solution (Ringer solution) at a near neutral pH value (7.4). The corrosion potential establishes itself during pre-exposure under OCP conditions and the polarization curve doesn't exhibit an active-passive transition. This low reactivity makes free corrosion and anodic conditions corresponding to an overall very low current density level. At this level, fluctuations of the curves observed in repeated measurements must be mainly attributed to (manual) sample handling prior to the electrochemical measurements. Cp-Ti and single-phase β-Ti-40Nb have been selected as references. For cp-Ti, the free corrosion potential established at about -0.25 V vs. SCE and a rather low corrosion current density of only ~45 nA/cm^2 is observed. This transfers into a spontaneous passivation of the surface in the anodic potential regime corresponding to a plateau-like behavior at a current density level of ~3.4 µA/cm^2 below 1 V vs. SCE. A very similar behavior is observed for Ti-40Nb, it exhibits a very

low corrosion current density of ~4 nA/cm^2 and transfers spontaneously to a stable passive regime at a current density level of ~2.5 µA/cm^2 up to 1 V vs. SCE.
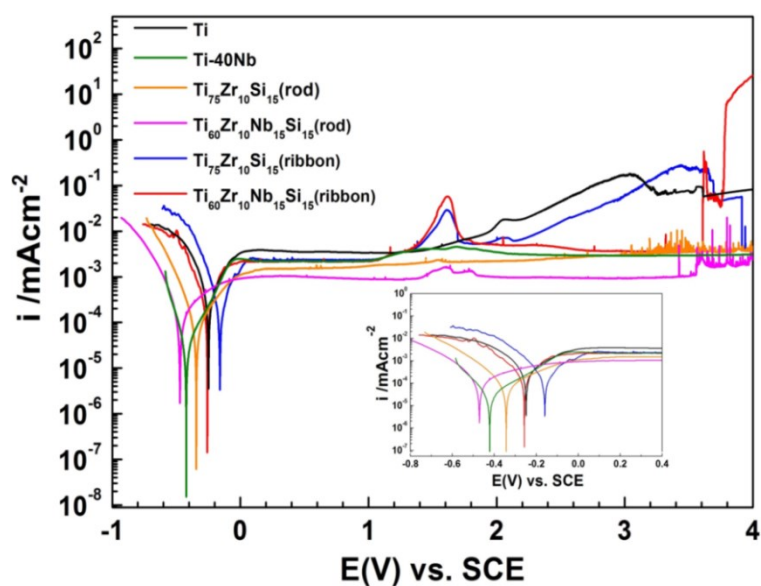

Figure 4.11: Potentiodynamic anodic polarization curves of cp-Ti, β-type Ti-40Nb (Ti$_{74.4}$Nb$_{25.6}$), Ti$_{75}$Zr$_{10}$Si$_{15}$, Ti$_{60}$Zr$_{10}$Nb$_{15}$Si$_{15}$ cast rods and of Ti$_{75}$Zr$_{10}$Si$_{15}$, Ti$_{60}$Zr$_{10}$Nb$_{15}$Si$_{15}$ melt-spun ribbons recorded in Ringer solution at 37°C; inset: higher resolved curve sections close to the free corrosion potential.

In addition, quasistatic polarization measurements of Nb and Zr have been conducted in order to better understand the alloy behavior (Fig. 4.12). Nb exhibits a similar low corrosion rate and very stable passivity like Ti. Zr shows also a low free corrosion activity, but a sudden increase of the current density at ~0.25 V vs. SCE due to passivity breakdown and pitting occurred confirming the observations from the CV analysis.

The anodic polarization curves for Ti$_{75}$Zr$_{10}$Si$_{15}$ and Ti$_{60}$Zr$_{10}$Nb$_{15}$Si$_{15}$ rods and ribbons are shown in Fig. 4.11. In case of the crystalline alloy states, similar as for Ti-40Nb, adding alloying elements (Zr, Si, Nb) to Ti shifts the corrosion potential to more negative values and slightly lowers the corrosion rate corresponding to a slight reduction of the corrosion current density (as can be seen in the inset of Fig. 4.11).
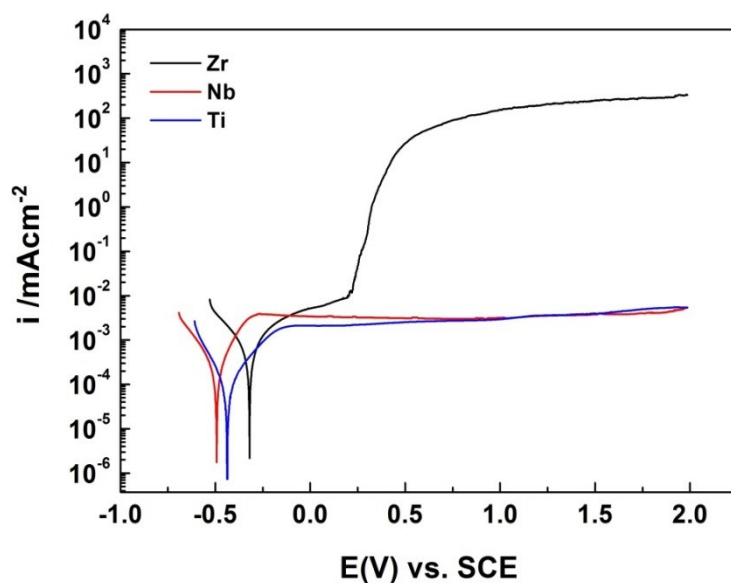
Figure 4.12: Potentiodynamic anodic polarization curves of Zr, Nb and Ti
recorded in Ringer solution at 37°C

The anodic polarization curves for $Ti_{75}Zr_{10}Si_{15}$ and $Ti_{60}Zr_{10}Nb_{15}Si_{15}$ rods and ribbons are shown in Fig. 4.11. In case of the crystalline alloy states, similar as for Ti-40Nb, adding alloying elements (Zr, Si, Nb) to Ti shifts the corrosion potential to more negative values and slightly lowers the corrosion rate corresponding to slight reduction of the corrosion current density (as can be seen in the inset of Fig. 4.11). Upon anodic polarization up to ~1.2 V vs. SCE, both crystalline alloys spontaneously passivate. Considering the reproducibility limits of these sensitive polarization systems, the passive current densities are of comparable level as for cp-Ti and Ti-40Nb. For both multiphase alloys, there is no passive layer breakdown in this potential range. Moreover, beyond the water stability potential range both alloys remain passive up to about 3 V vs. SCE, above which some metastable pitting is possible (current fluctuations).

At least for the ternary crystalline alloy, this is different from the behavior observed during fast potential sweeping in the CV measurements. It suggests that, under quasistatic conditions, also the ternary alloy can form stable protective barrier-type passive films in a wide potential range despite the enrichment of pitting-sensitive Zr in its phases.

Homogenization of the microstructural state of Ti-Zr-(Nb)-Si alloys by melt-spinning does not significantly change the polarization behavior under quasistatic conditions. The corrosion potentials are slightly shifted to more positive values, but the corrosion current density remains at a similar very low level. Upon anodic polarization, spontaneous passivation occurs and a passive current density level similar to that measured for the crystalline counterparts is

maintained in the potential range of water stability (up to ~1.2 V vs. SCE). For both nearly fully glassy alloys, pitting was not observed upon further polarization (>1.2 V vs. SCE). Some typical features, "water decomposition peaks", occur which must be ascribed to the problematic geometry of the ribbon samples that was discussed before.

Similar as for cp-Ti, the melt-spun ternary alloy exhibits a gradual increase of the current during the high polarization regime. This is an indication for certain electron permeability of the growing oxide film, which is for Ti known to be due to the semi-conductive properties of the film. The melt-spun $Ti_{60}Zr_{10}Nb_{15}Si_{15}$ alloy shows stable passivity in this high polarization regime with some weak indication for metastable pitting at >3 V vs. SCE (similar as the crystalline counterpart).

Similar investigations have been done by Qin et al. [45] for glass-forming Ti-Zr-Cu-Pd-Sn alloys and by Oak et al. [8,85] for Ti-Zr-Ta-Si alloys in body simulated fluids at 37°C. They conducted quasistatic polarization measurements up to 1.5 V vs. SCE.

For Cu-containing alloys certain passivity breakdowns and pitting events occur at defined potentials less than 1.5 V vs. SCE, but the Ti-Zr-Ta-Si alloy system demonstrates a similar stable behavior as that of our alloys up to 1.5 V vs. SCE. In comparison, in the present study it was proved, a very high stability of the passive state in a wider anodic potential range for melt-spun $Ti_{75}Zr_{10}Si_{15}$ and $Ti_{60}Zr_{10}Nb_{15}Si_{15}$, i.e. even beyond the water stability limit [8,45,85].

4.3.3 Potentiostatic polarization

Potentiostatic polarization measurements were conducted in order to study the anodic passive film growth mechanism in more detail. Anodic current density transients were recorded for $Ti_{75}Zr_{10}Si_{15}$ and $Ti_{60}Zr_{10}Nb_{15}Si_{15}$ melt-spun ribbons and are shown in the double-logarithmic plot in Fig. 4.13. Measurements have been carried by stepping the potential from a stable OCP to two different anodic potentials, one in the range of the stable passive region, i.e. at 0.5 V vs. SCE, and another one in the high polarization regime, i.e. at 4 V vs. SCE. As reference material the single-phase Ti-40Nb was employed here, as it exhibits very precisely the characteristic anodic behavior of valve metals [7].

In the case of Ti-40Nb, when stepping the potential to 0.5 V vs. SCE, the measurable current density transient is clearly linear with a slope of m = -1 after an initial period. This is indicative for a high-field-controlled passive film growth, i.e. a migration of film-forming ionic species through an already existing oxide film under control of a high electric field across the film cross-section [120]. When stepping the potential to a much higher value of 4 V vs. SCE, a

similar linear behavior at a higher current density level is observed. This demonstrates the rapid formation of a barrier-type passive film with no or very low permeability for electric charges (electrons) even under this extreme polarization condition. Compared to this nearly ideal behavior of Ti-40Nb, for both melt-spun Ti-(Nb)-Zr-Si alloys the current transients obtained when stepping the potential to 0.5 V vs. SCE are very similar.
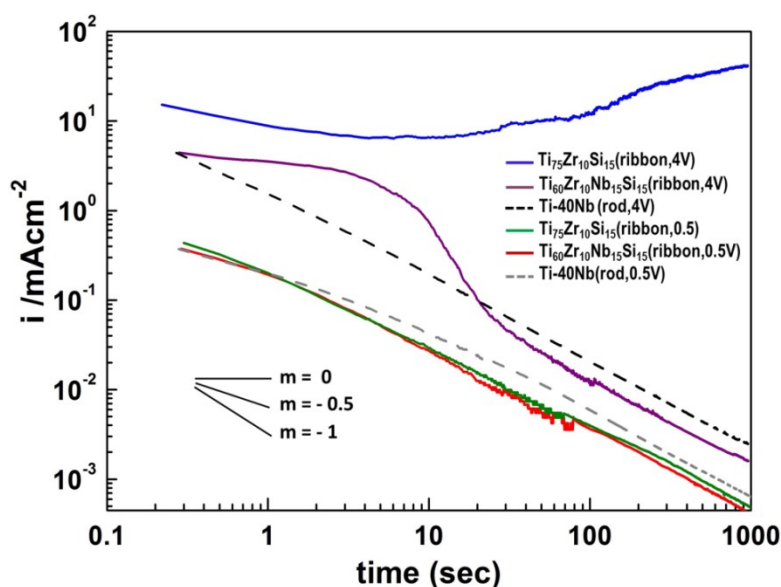

Figure 4.13: Current density transients recorded upon potentiostatic anodic polarization of the β-type Ti-40Nb and $Ti_{75}Zr_{10}Si_{15}$ and $Ti_{60}Zr_{10}Nb_{15}Si_{15}$ ribbons in Ringer Solution at 37°C at selected potentials: 0.5V and 4V vs. SCE.

This confirms that also for these nearly fully glassy alloy samples this mechanism holds. There is no significant difference between the Nb-free and the Nb-containing alloy.

In contrast, when stepping the potential to the high polarization regime (4 V vs. SCE) a deviation from the ideal behavior occurs for both glassy alloys. In repeated measurements, for the melt-spun $Ti_{75}Zr_{10}Si_{15}$ alloy current density transients were measured at rather high levels with a mean slope m~0. Those are characteristic for metal dissolution which will in this case superimpose the limited water decomposition reaction (that was detected in quasistatic polarization experiments). An additional SEM analysis of ribbon samples after the transient measurements (Fig. 4.14) revealed local corrosion damage which was initiated at various defect sites of a ribbon surface. The images clearly show a quite uniform propagation of the corrosion front leading to a nearly spherical damage. This confirms a monotonic rate of the corrosion reaction in the metastable nearly single-phase glassy material. Current transients recorded for

melt-spun $Ti_{60}Zr_{10}Nb_{15}Si_{15}$ samples comprise an initial period of dominant corrosion followed by a transfer into stable passive film growth similar as to what has been observed for Ti-40Nb.
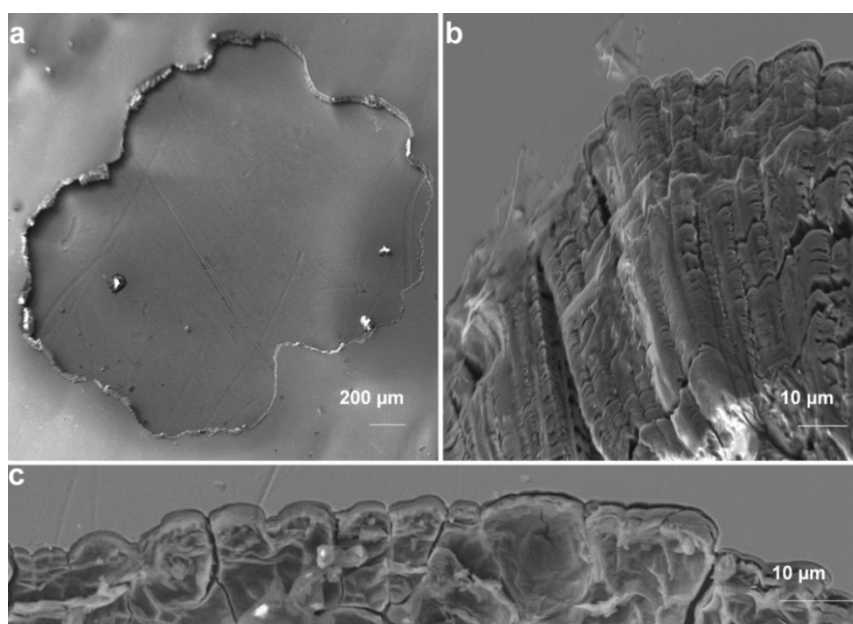

Figure 4.14: SEM images of corroded areas of a $Ti_{75}Zr_{10}Si_{15}$ ribbon sample observed after potentiostatic polarization at 4V vs. SCE in Ringer solution, a) corrosion damage-overview, b, c) rim regions of the corrosion damage showing the front of corrosion propagation.

After detecting metastable pitting at this high potential regime under quasistatic polarization conditions (Fig. 4.11), this indicates that, under potential-stepping conditions the Nb-containing glassy alloy has a certain tendency for healing its surface after a corrosion initiation event.

4.3.4 Surface analysis of passive films on melt-spun ribbons

XPS investigations: A surface analysis of $Ti_{75}Zr_{10}Si_{15}$ and $Ti_{60}Zr_{10}Nb_{15}Si_{15}$ melt-spun ribbons has been firstly done by means of XPS in order to determine elemental compositions and oxidation states of the elements in the spontaneously forming passive films. It was performed on the air-sides of ribbon samples which were polished to grit 4000 and exposed to air for 24 hours and for samples that were immersed after polishing in Ringer solution (37°C) at OCP condition for 20 hours. The high resolution spectra of all alloying elements and of oxygen are exemplarily shown for air-exposed states for $Ti_{75}Zr_{10}Si_{15}$ and $Ti_{60}Zr_{10}Nb_{15}Si_{15}$ ribbons in Fig. 4.15.
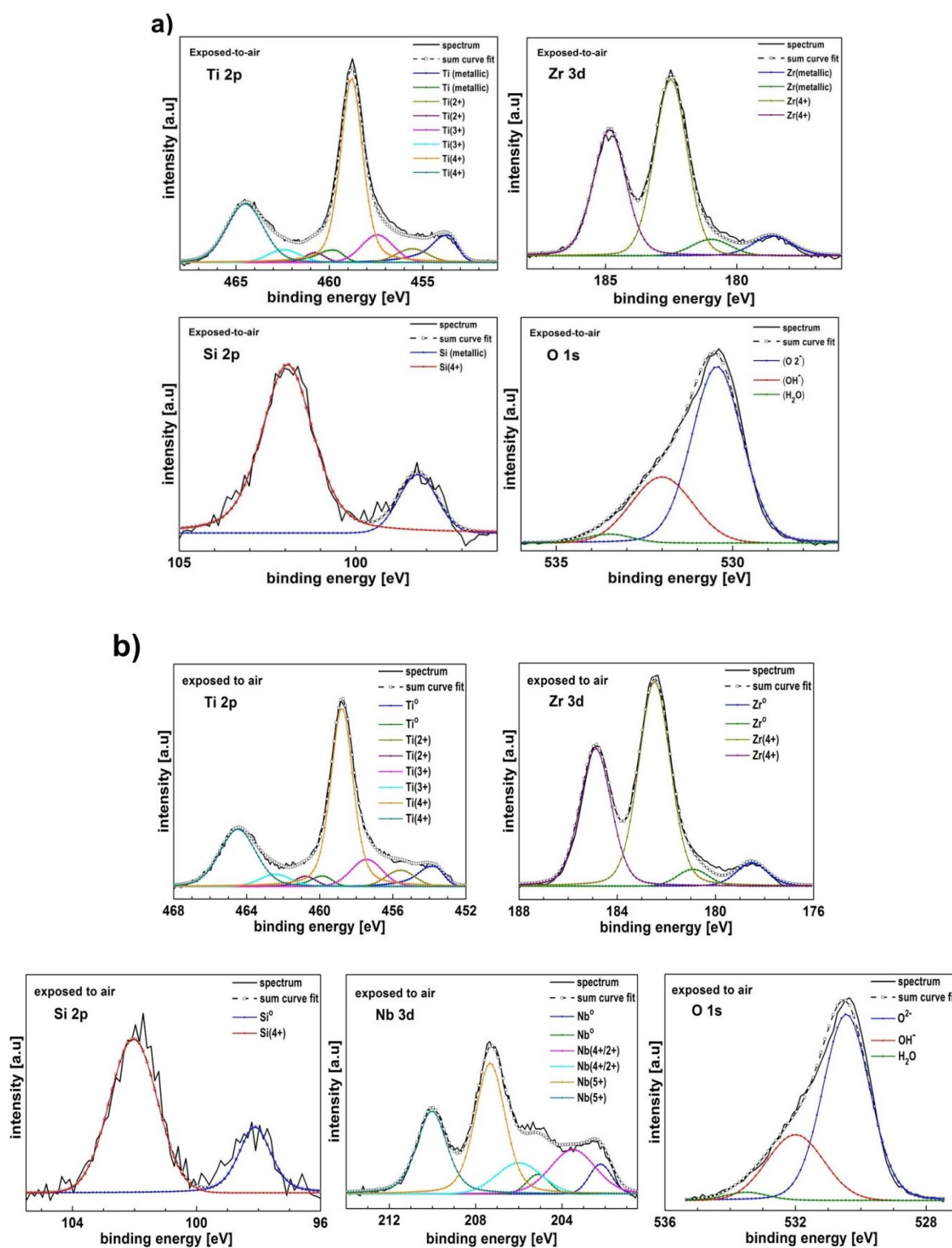
Figure 4.15: XPS analysis of a) $Ti_{75}Zr_{10}Si_{15}$ and b) $Ti_{60}Zr_{10}Nb_{15}Si_{15}$ ribbon
surface exposed to air measured and fitted core level spectra of Ti 2p, Zr 3d,
Nb 3d, Si 2p and O 1s

Several literature sources have been used for indexing the peaks of all observed chemical states

[121,153-155]. According to this, peak fits for the appropriate components were perfomed and

are presented in Fig. 4.15(a). For both alloys, peaks of all alloying elements in the metal state (Me°) are present which reveals that the spontaneously formed passive films are very thin. In the spectra of Ti 2p three doublets are observed corresponding to Ti^{2+}, Ti^{3+} and Ti^{4+} with a main presence of the Ti^{4+} peaks [7,156]. For Zr 3d, a doublet of $3d_{5/2}$ and $3d_{3/2}$ peaks from the Zr^{4+} state is identified at 182.5 and 184.8 eV, besides detectable Zr^0 peaks. The binding energy of Si 2p at 102 eV exhibits the presence of the Si^{4+} state and the peak at 98 eV is demonstrating Si^0. In case of $Ti_{60}Zr_{10}Nb_{15}Si_{15}$, in addition, for Nb 3d multiple valence states are detected. The dominating doublet at 207.3 eV and 210 eV is ascribed to the Nb^{5+} main state while beside some residuals of the Nb^0 state (202.2 eV and 205.1 eV) weaker peaks at 203.5 and 206 eV can be related to sub-oxides with states of Nb^{4+} (NbO_2) or Nb^{2+} (NbO). All O 1s spectra comprise a main peak of the O^{2-} state at 530.5 eV. Therefore, it can be concluded that the passive film on the ternary alloy is mainly composed of TiO_2, ZrO_2, SiO_2 and that on the quaternary alloy comprises in addition Nb_2O_5. Also, formation of mixed oxides of the constituents may be considered. Besides that the O 1s spectra comprise two lower peaks at 532.0 and 533.5 eV which are attributed to oxygen states in OH^- and adsorbed H_2O.

A direct comparison of the detailed spectra measured for air-exposed samples and for samples immersed in Ringer solution for $Ti_{60}Zr_{10}Nb_{15}Si_{15}$ melt-spun ribbons is shown in   Fig. 4.16. It reveals for all alloying elements a decrease of the peak intensities of the lower valence oxide states and of the metallic state after immersion in Ringer solution. This is the consequence of an accelerated passive film growth in the aqueous medium based on the formation of oxides corresponding to the higher valence states of the alloy constituents. An increase of the OH^- and H_2O shoulders in the O 1s spectrum for the Ringer immersed samples is consistent with the raise of hydroxides and adsorbed H_2O on the surface of sample after immersion in an aqueous medium. It can be concluded that on both alloy surfaces, all alloying elements in both systems contribute to the passive film growth in air and in Ringer solution under OCP condition. These natural passive films comprise mainly oxides with higher valence states, but there is also some evidence for residuals with lower valence oxide states of Ti and Nb.
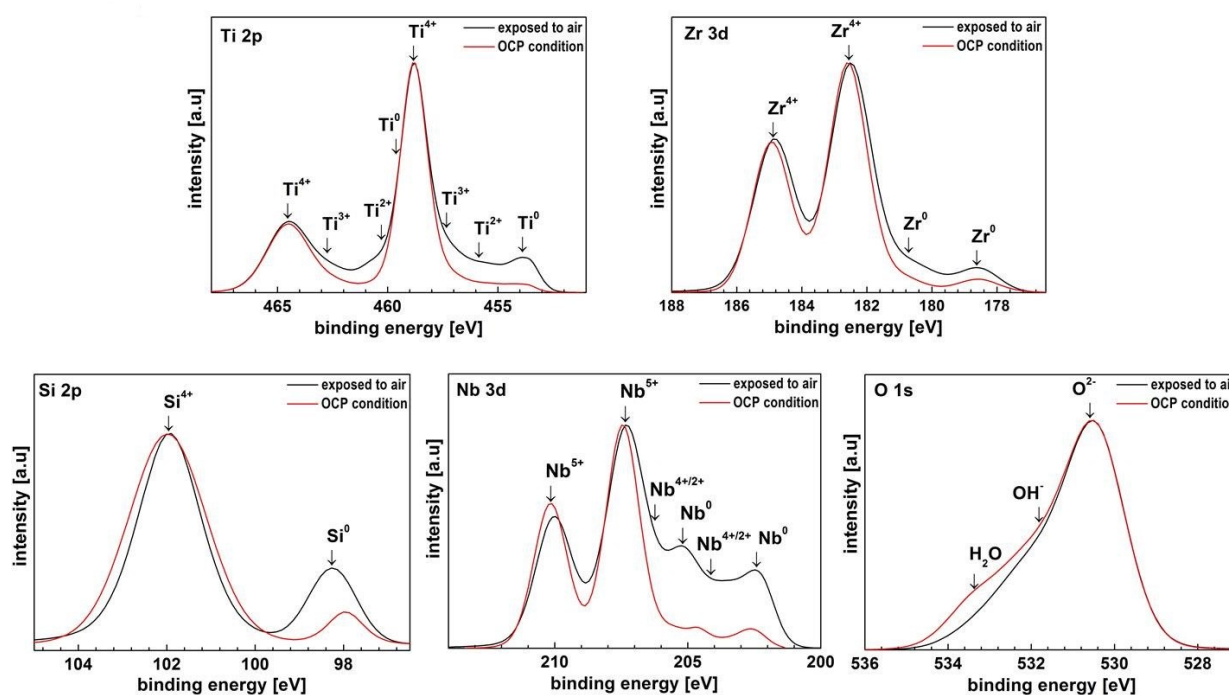
Figure 4.16: Comparison of XPS analysis of $Ti_{60}Zr_{10}Nb_{15}Si_{15}$ ribbon surfaces exposed to air and immersed in Ringer solution under OCP condition for 20 hours; measured core level spectra of Ti 2p, Zr 3d, Nb 3d, Si 2p and O 1s.

AES investigations: For a further detailed characterization of the passive films which form on the glass-forming Ti(-Nb)-Zr-Si alloys in simulated body fluids, sputter depth-profiling was conducted. As pre-investigations revealed, the AES method was identified as being the favorable method in comparison with XPS for this purpose because of the higher sputtering rates and the well-defined measuring area selection [123].

For this study, melt-spun sample surfaces (air-side) naturally passivated during air exposure were employed as reference state. Further, sample surfaces which were not only immersed in Ringer solution under OCP condition, but which were also anodically polarized at 0.5 V and 4 V vs. SCE were analyzed. Figure 4.17 summarizes exemplary depth profiles obtained by AES sputter depth profiling of $Ti_{60}Zr_{10}Nb_{15}Si_{15}$ sample surfaces. The AES profile of the surface region of the naturally passivated sample (Fig. 4.17(a)) reveals that the oxygen concentration gradually decreases within the first ~100 seconds of sputter time which corresponds to an oxide thickness of below 10 nm.
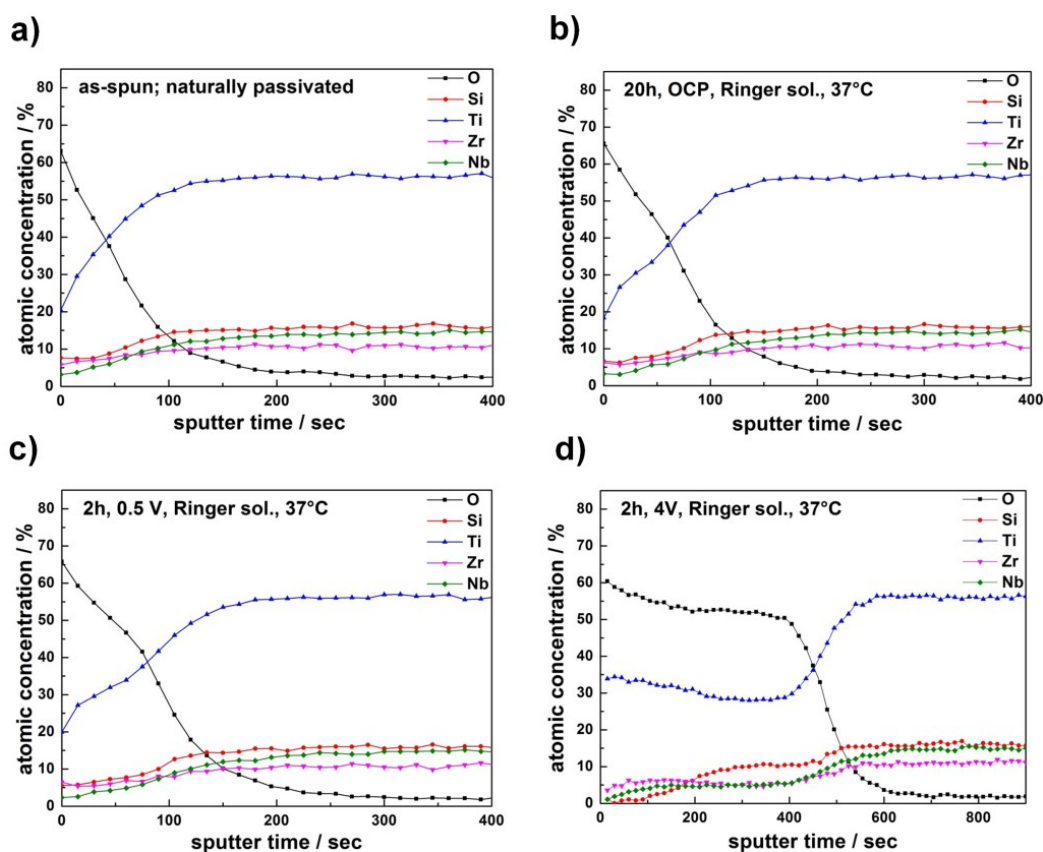
Figure 4.17: Elemental concentration depth profiles obtained from AES measurements at surfaces (airside) of $Ti_{60}Zr_{10}Nb_{15}Si_{15}$ ribbons a) naturally passivated in air, b) immersed in Ringer solution at 37°C for 20 hours under OCP condition, c) after potentiostatic polarization at 0.5 V vs. SCE for 2 hours, d) after potentiostatic polarization at 4 V vs. SCE for 2 hours.

Correspondingly, the concentrations of the alloying element species Ti, Zr, Nb and Si gradually increase up to a plateau level. This plateau is indicative for the surface region of the metallic state with the nominal concentration of the alloying elements. The initial sputter time period, at which the elemental concentrations including O gradually decay, is the passive film region. More strictly, the sputter time, at which the oxygen signal decayed to the half width value between maximum and minimum value, was defined as oxide/metal interface.

The AES analysis confirms that all constituent element species are present in the oxide film, whereby the Ti oxide species fraction dominates. The depth profiles of samples immersed in Ringer solution under OCP conditions and polarized at 0.5 V vs. SCE (Fig. 4.17(b, c)) are very similar showing only a gradual expansion of the surface oxide region. Polarization at 4 V vs. SCE (Fig. 4.17(d)) strongly enhances the passive film growth. The oxygen concentration remains at a plateau level within the first ~400 sec of sputtering and only then steeply decreases reflecting the oxide/metal interface region. Accordingly, the Ti concentration decayed only

marginally in the oxide layer region with a slight trend to deplete towards the inner interface. From the concentration profiles of the other constituent elements a two-zone nature of the passive film can be derived. In the outermost zone (<200 sec sputter time) Si species are strongly depleted (close to 0%) relative to Zr and Nb species, whereby Si is relatively enriched in the inner oxide film zone (~200-400 sec).

From the half width values of the oxygen concentration profiles thickness values of the passive films were estimated considering a reference sputter time of the AES system in SiO_2 of 4.7 nm/min. Results of this estimation for both alloys are summarized in Fig. 4.18. It is evident that the addition of Nb to the nearly fully glassy $Ti_{75}Zr_{10}Si_{15}$ alloy does not significantly change the passive film thickness. Immersion in Ringer solution or anodization at 0.5 V vs. SCE leads to a slight increase of the film thickness, but values remain small, i.e. <10 nm. Polarization at 4 V vs. SCE results in a marked thickness rise by about 5 times.
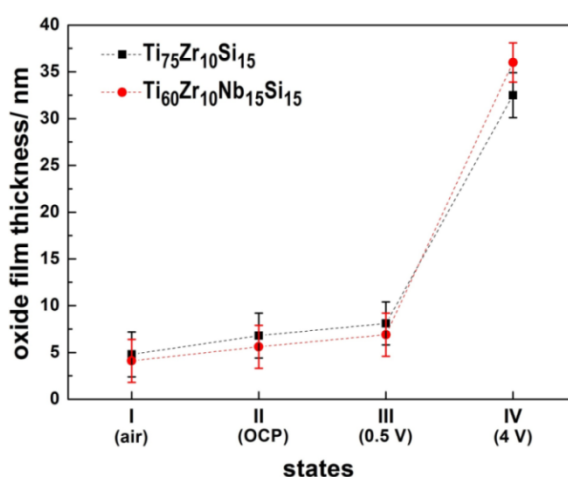

Figure 4.18: Thickness data of the passive films formed on melt-spun $Ti_{75}Zr_{10}Si_{15}$ and $Ti_{60}Zr_{10}Nb_{15}Si_{15}$ ribbon surfaces after I) exposure to air for 20 hours, II) immersion in Ringer solution at 37°C for 20hours, III) after anodic polarization at 0.5 V vs. SCE for 2hours, IV) after anodic polarization at 4 V vs. SCE for 2 hours. Data were obtained from AES depth profiles (Fig. 4.18), i.e. from an analysis of the oxygen concentration change.

Summary: The corrosion and passivation behavior of glass-forming $Ti_{75}Zr_{10}Si_{15}$ and $Ti_{60}Zr_{10}Nb_{15}Si_{15}$ alloys in simulated body fluid (Ringer solution) at 310 K was assessed. Cyclic voltammetry indicated that all alloy constituents participate in the anodic passive film formation. Zr is the critical element that can induce pitting when non-homogeneously distributed in the $Ti_{75}Zr_{10}Si_{15}$ alloy (multiphase crystalline state). The addition of 15 at.-% Nb as partial substitution of Ti as well as the homogenization of the structural alloy state by rapid

quenching towards a mainly glassy state significantly improves the anodic passive layer stability even beyond the water stability limit. Under quasi-static polarization conditions, both alloys show in the multiphase crystalline state as well as in the homogenized mainly glassy state very low corrosion rates and stable anodic passivity in the potential range of water stability and only some metastable pitting at high polarization, i.e. >3 V vs. SCE. Thus, their anodic stability is superior to that of Cu-containing metallic glasses and comparable to that of glassy Ti-Zr-Ta-Si alloys and β-type Ti-40Nb. The anodic passive film formation follows a high-field growth mechanism which is typical for valve metals and which is ideally reflected by the β-type Ti-40Nb reference alloy. However, potentiostatic polarization of melt-spun samples at high potentials (4 V vs. SCE) reveals a destabilization of passivity towards pitting in case of the ternary alloy and towards delayed passivation in the case of the quaternary alloy. Detailed surface-analytical studies by means of XPS and AES confirmed the participation of all alloy constituents in the surface passivation at conditions of air exposure as well as of immersion and anodic polarisation in Ringer solution. Passive films are very thin, i.e. <10 nm, and are mainly comprised of the constituent oxides with the highest valence states. A strong thickness increase occurs when polarizing the samples at 4 V vs. SCE. This is accompanied by a non-homogeneous distribution of constituent oxides, in particular with an enrichment of silicon oxide in the inner zone of the passive layer.

4.4 Thermal oxidation of melt-spun ribbons

As described in sections 2.2.3 and 2.3.4, surface modifications are carried out in order to provide metallic implant surfaces with improved topographical, physical and chemical properties with the aim that bone-implant bonding processes can be stimulated and optimized. Besides that the corrosion and wear resistance can be improved.

One of the noticeable reasons why Ti and Ti-based alloys are widely used as medical implant materials is the spontaneously forming passive oxide film (mainly TiO_2) on the surface. This native oxide film which is about 4-6 nm thick can offer good corrosion resistance. But the poor mechanical properties of the native form of TiO_2 can lead to fracture of the film already under very low stresses, such as by rubbing the implant against soft tissues [72] and the resulting wear debris and the metal ions can lead to adverse tissue reactions [157].

Thermal oxidation is one of the cost-effective surface modification methods to generate a thicker barrier-type oxide layer on a Ti alloy surface to improve the surface characteristics.

During the thermal oxidation process, Ti can easily react with air due to its affinity to oxygen and induce a formation of a thicker oxide layer with changes in the grain size and morphology of the oxides and consequently increasing the surface roughness. It has been shown that for crystalline Ti and Ti-based alloys, at a temperature above 200°C, a crystalline oxide film can be promoted [158]. The crystalline oxide can be a mixture of anatase and rutile forms while increasing the temperature leads to the rutile dominating the oxide structure. The rutile structure is more preferable due to its better inertness to bacterial attack [159], having a high hardness and a low friction coefficient, which can better reduce wear as compared to the anatase structure [160]. It has been reported that formation of this thick oxide film which is mechanically more stable and chemically resistant enhances hardness, corrosion and wear resistance of Ti and its crystalline alloys [72-75,161-165]. In addition, the increase of the surface roughness improves surface wettability and provides a better cell adhesion. Higher wettability enhances the cellular response through improved protein absorption and apatite formation [166].

In the thermal oxidation process, varying the temperature and the exposure time results in remarkable effects on the oxide film characteristics. Some studies reveal that the surface roughness increases with an increase of oxidation time [167] and it is reported that, at higher temperatures, the oxide layer is non-adherent [72,168]. This raises the necessity of optimizing the oxidation temperature and time.

In this study, a thermal oxidation analysis has been performed for glass-matrix nano-composite $Ti_{75}Zr_{10}Si_{15}$ and $Ti_{60}Zr_{10}Nb_{15}Si_{15}$ melt-spun ribbons. Their oxidation behavior has been investigated at different temperatures by means of DSC, dynamic and isothermal TG analysis and by characterization of oxidized sample surfaces with XRD and SEM. Exemplarily, the sample heated at 550°C has been further studied in more detail by TEM, AES and AFM methods. Other tests as microhardness and wettability have been carried out and finally the in-vitro bioactivity of the modified surfaces has been examined by SBF testing.

4.4.1 Thermal stability of melt-spun ribbons

DSC measurements have been performed to study the crystallization behavior of the melt-spun ribbons under inert gas atmosphere. Figure 4.19 shows characteristic DSC curves of $Ti_{75}Zr_{10}Si_{15}$ and $Ti_{60}Zr_{10}Nb_{15}Si_{15}$ ribbons.
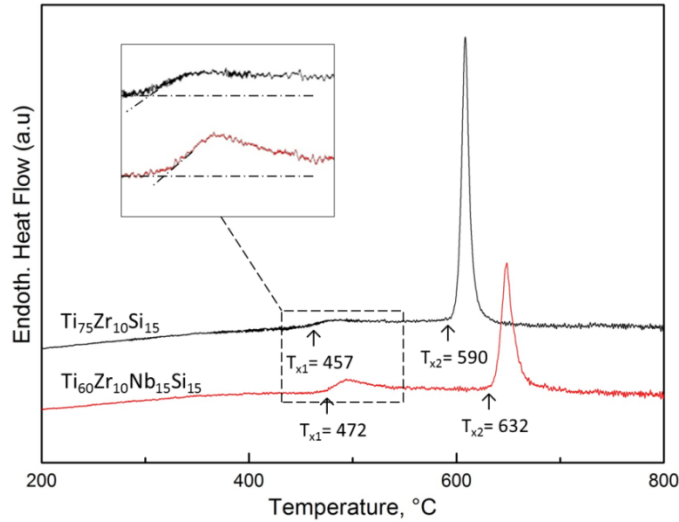
Figure 4.19: DSC curves of $Ti_{75}Zr_{10}Si_{15}$ and $Ti_{60}Zr_{10}Nb_{15}Si_{15}$ melt-spun ribbons recorded at a constant heating rate of 10 K min^{-1} in argon atmosphere.

For both alloys a glass transition (T_g) is not detectable, but two exothermic peaks are observed. The onsets of the first and the second crystallization peaks are T_{x1} = 457, T_{x2} = 472 for $Ti_{75}Zr_{10}Si_{15}$ and T_{x1} = 590, T_{x2} = 632 for $Ti_{60}Zr_{10}Nb_{15}Si_{15}$ ribbons. The onset of the second crystallization peaks exhibits the maximum temperature until that the ampurphous phase is stable in each composition.

Post-annealing treatments at temperatures closely after the two crystallization peaks of the $Ti_{60}Zr_{10}Nb_{15}Si_{15}$ alloy were exemplarily performed to identify the associated phase transformation reactions. The XRD patterns and the TEM results are summerized by Calin et al. [16] and reveal, for a sample heated up to 590°C, a composite structure consisting of nano-sized spherical particles dispersed in a glassy matrix. Therefore, the first exothermic peak is associated with the formation and growth of bcc β-Ti(Nb) nanocrystals embedded in a residual glassy matrix as a primary crystallization phase. The formation of bcc nanocrystals may be due to "quenched-in" nuclei which are not bypassed during the melt-spinning and which can act as heterogeneous nucleation sites during subsequent heating. The sample heated up to 720°C exhibited the formation of a multi-phase ultrafine crystalline structure at the nano-size level comprising the intermetallic $(Ti,Zr,Nb)_5Si_3$ phase and the bcc β-Ti(Nb) phase (the same phases as those defined in the crystalline counterpart, see section 4.1.1).

4.4.2 Thermal oxidation of melt-spun ribbons

Thermogravimetry (TG) has been applied to investigate the oxidation behavior of the alloys in a synthetic air environment. The TG is used to complement the DSC by measuring mass changes of a sample as a function of temperature or time. In this study, the oxidation behavior of the samples is studied using dynamic TG and isothermal TG. Figure 4.20 displays characteristic dynamic TG curves of $Ti_{75}Zr_{10}Si_{15}$ and $Ti_{60}Zr_{10}Nb_{15}Si_{15}$ ribbons recorded at a continuous heating rate of 10 K min^{-1}. The curves can be divided into 4 regions according to their trend. The first region is up to 400°C and no significant mass change can be observed, which means that oxidation is not establishing, yet. The second region from 400°C to 650°C shows mass increase and indicates the beginning of oxidation with rising temperature. At the higher temperature level of this second region the surface oxidation is superimposed to the main crystallization events (as indicated by DSC). Obviously, internal intermetallic transformation triggers the surface oxidation. Therefore, there is a short third region from ~650°C to ~720°C in which the slope of the mass change curve is reduced. The last region (IV) of the mass change curves up to 1000°C is characterized by a sharp increase of the slope for the $Ti_{75}Zr_{10}Si_{15}$ alloy and a less pronounced increase for the $Ti_{60}Zr_{10}Nb_{15}Si_{15}$ alloy. Both are indicative for an enhanced oxidation. Comparing the response of the ternary alloy with that of the quaternary one, it can be concluded that addition of Nb to the alloy results in a decreasing oxidation rate. This can be seen in relation to the described effect of Nb on improving the passive film stability at room temperature as stated in section 4.3.1.
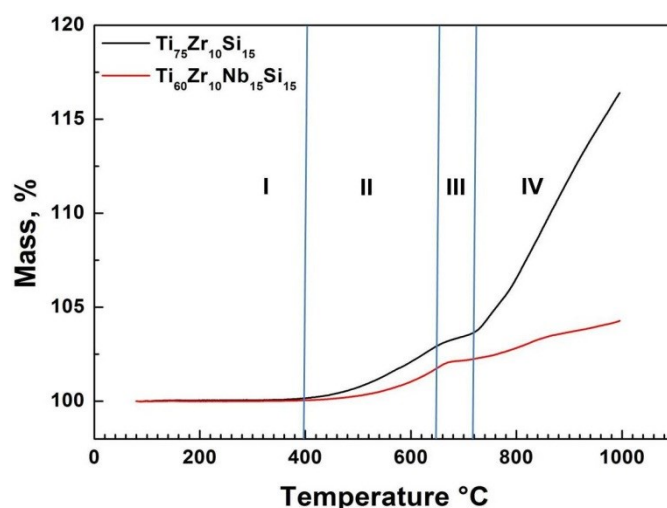

Figure 4.20: Dynamic TG curves of $Ti_{75}Zr_{10}Si_{15}$ and $Ti_{60}Zr_{10}Nb_{15}Si_{15}$ melt-spun ribbons recorded at a constant heating rate of 10 K min^{-1} in synthetic air.

To better understand the oxidation behavior, isothermal measurements have been carried out for certain temperatures. Figure 4.21 shows a representative isothermal measurement

procedure for $Ti_{75}Zr_{10}Si_{15}$ in synthetic air. The whole procedure comprises 4 steps starting with an initial fast dynamic heating with 40 K min^{-1} up to a temperature of 100°C below the isothermal annealing temperature. This is followed by a further slower dynamic heating with 10 K min^{-1} up to the isothermal annealing temperature. Isothermal annealing was conducted at a selected temperature for 3 hours and finally, a cooling step followed with a cooling rate of 40 K min^{-1}. The key step for the analysis is the isothermal annealing step 3.
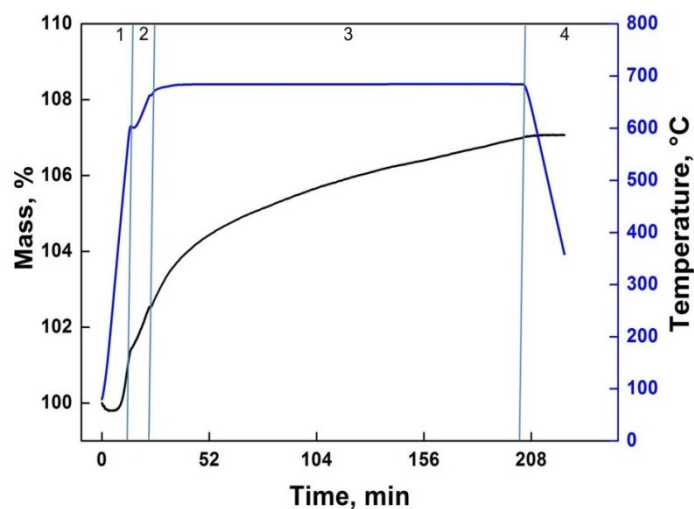

Figure 4.21: Isothermal TG procedure applied to $Ti_{75}Zr_{10}Si_{15}$ melt-spun ribbons in synthetic air. The key step is the isothermal step 3 corresponding to an annealing at 700°C for 3 hours.

Typical data from the third step, which displays the mass change of the samples as a function of time at defined temperatures, is shown in Figs. 4.22 and 4.23 for both alloys. The temperatures for isothermal annealing have been selected from regions II, III and IV of the dynamic TG curves. For both alloys, isothermal TG curves at 550°C, 700°C and 800°C have been measured. In all cases the trend for a parabolic oxidation rate law can be derived. Different oxide growth rate laws have been described in section 3.6 and their related curves were shown. When comparing them with the curves in Figs. 4.22 and 4.23, it can be concluded that both alloys display a parabolic growth rate which is indicative for a diffusion controlled oxidation mechanism. By increasing the annealing temperature the mass change and consequently, the oxidation rate grows.
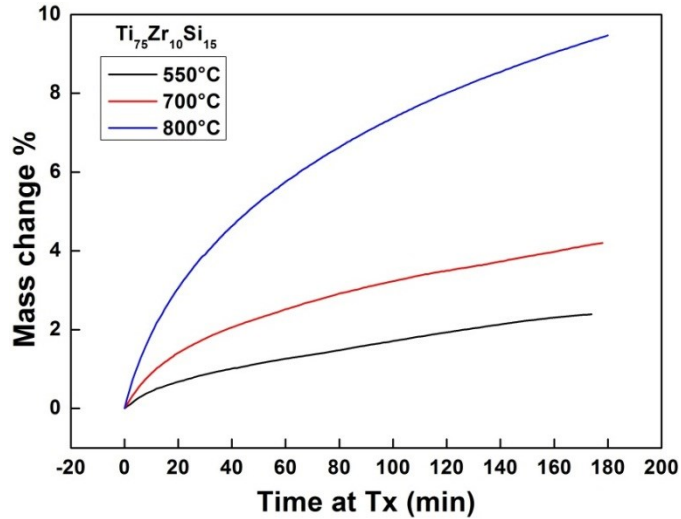
Figure 4.22: Isothermal TG curves of $Ti_{75}Zr_{10}Si_{15}$ melt-spun ribbons recorded at different temperatures for 3 hours in synthetic air.
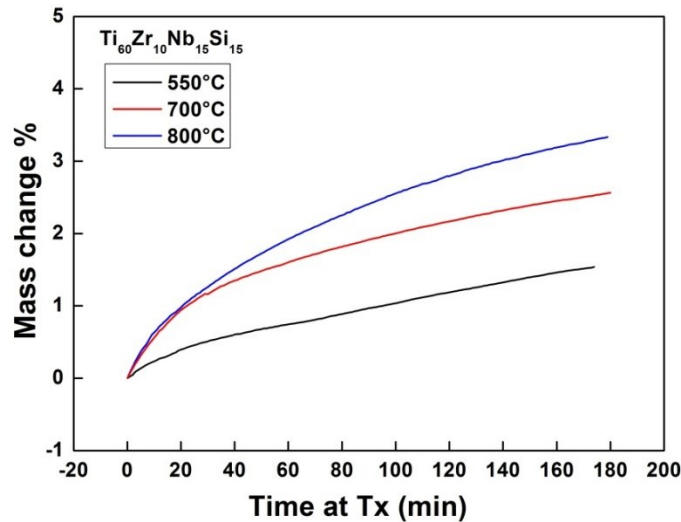

Figure 4.23: Isothermal TG curves of $Ti_{60}Zr_{10}Nb_{15}Si_{15}$ melt-spun ribbons recorded at different temperatures for 3 hours in synthetic air.

Comparing the responses of the $Ti_{60}Zr_{10}Nb_{15}Si_{15}$ samples (Fig. 4.23) with those of the $Ti_{75}Zr_{10}Si_{15}$ (Fig. 4.22) samples reveals that the quaternary alloy shows a lower mass change than the ternary alloy at all temperatures. This trend is in good agreement with the dynamic TG curves and indicates that Nb retards the oxidation process. This effect is also obvious in Fig. 4.24, in which the final mass changes of both alloys after isothermal treatment at certain temperatures for 3 hours are comparatively summarized.
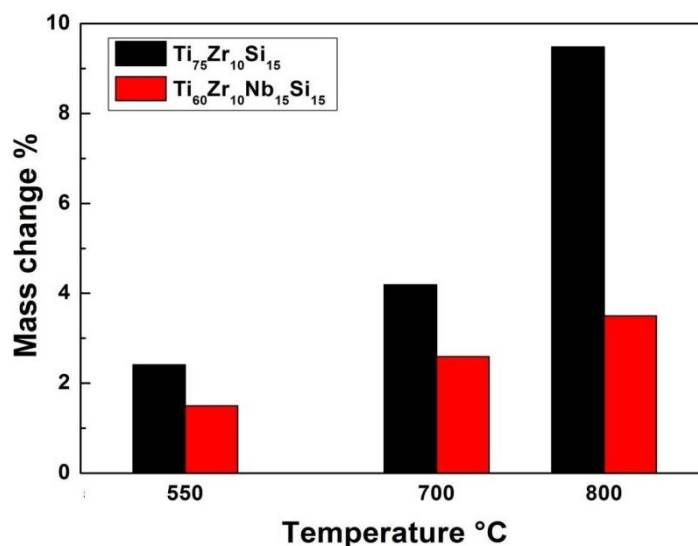
Figure 4.24: Mass change of Ti$_{75}$Zr$_{10}$Si$_{15}$ and Ti$_{60}$Zr$_{10}$Nb$_{15}$Si$_{15}$ melt-spun ribbons after 3 hours treatment in synthetic air at 550°C, 700°C and 800°C.

Although a full understanding of the effect of Nb is still missing, there are some proposed mechanisms that may partially explain it. Reported results of other studies about the effect of Nb on the oxidation of Ti and some Ti-based alloys can be shortly stated as: (1) Nb enhances the formation of a Ti-rich nitride layer at the interface between alloy and oxide layer which results in the inhibition of the diffusion of titanium and oxygen ions [169-171]. (2) Nb decreases the solubility of oxygen in the alloy due to the better protective oxide layer formed [172]. (3) Doping of Ti with Nb and partially replacing Ti^{4+} with Nb^{5+} ions in the lattice leads to a decrease of the number of oxygen vacancies, which consequently slows down the diffusion of oxygen [152,169,173].

X-ray diffraction patterns of samples which were isothermally treated for 3 hours at temperatures which were selected from each region of the dynamic TG curves (Fig. 4.20) are shown in Fig. 4.25 and Fig. 4.26. For Ti$_{75}$Zr$_{10}$Si$_{15}$ it can be seen that patterns of samples treated at 350°C (region I) and 550°C (region II) and for Ti$_{60}$Zr$_{10}$Nb$_{15}$Si$_{15}$ patterns of samples treated at 350°C (region I), 550°C (region II) and 670°C (region III) are similar to those of the as-cast ribbons (see section 4.1.2). They are composed of a sharp peak at ~45° superimposed on a diffuse halo. Therefore, it is concluded that they have a similar microstructure, i.e. a nanocrystalline phase identified as bcc β-Ti(Nb), dispersed within a glassy matrix phase
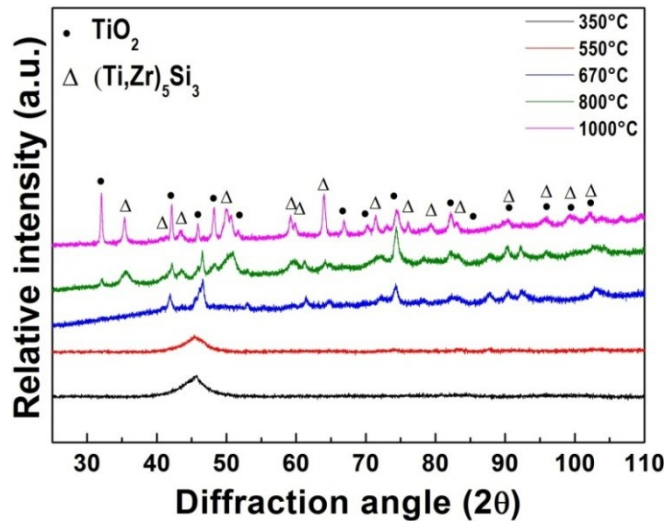
Figure 4.25: XRD patterns corresponding to $Ti_{75}Zr_{10}Si_{15}$ melt spun ribbons prepared by applying isothermal TG treatments at 350°C, 550°C, 670°C, 800°C and 1000°C.

The patterns after treatment for the ternary alloy at 670°C and for the quaternary alloy after treatment at 800°C reveal the beginning of crystallization. By increasing the temperature to 1000°C a multi-phase crystalline structure evolves. The XRD pattern of $Ti_{75}Zr_{10}Si_{15}$ consists of reflections of the intermetallic phase $(Ti,Zr)_5Si_3$ and of TiO_2. The pattern of $Ti_{60}Zr_{10}Nb_{15}Si_{15}$ is composed of reflections of $(Ti,Zr,Nb)_5Si_3$, TiO_2 and β-Ti(Nb). The defined phases except the oxide phase are similar to those identified for crystalline rod samples (see section 4.1.1). For the quaternary alloy crystallization takes place at higher temperatures than for the ternary alloy. As it is described by Calin et al. [16], the addition of Nb, which is a β-stabilizer, results in primary nanocrystallization of the bcc β-Ti(Nb) phase with a high particle density. The high particle density may cause rapid diffusion impaction which inhibits nanocrystal growth. In addition, Si shows a reduced solid solubility in the bcc β-Ti(Nb) phase. A rejection of it at the nanocrystal-amorphous matrix interface may delay the nuclation of secondary intermetallic phases.
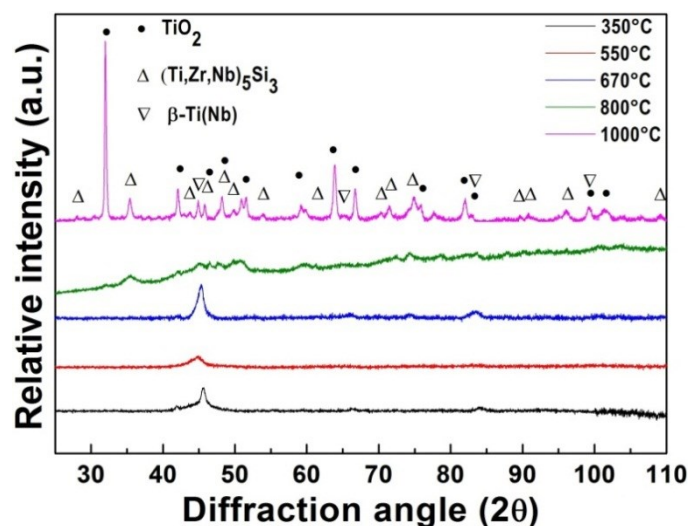
Figure 4.26: XRD patterns corresponding to $Ti_{60}Zr_{10}Nb_{15}Si_{15}$ melt spun ribbons prepared by applying isothermal TG treatments at 350°C, 550°C, 670°C, 800°C and 1000°C.

Figure 4.27 shows SEM micrographs of the sample surface after oxidation at 550°C, 700°C and 800°C for 3 hours in synthetic air. For both alloys, at 550°C the oxide film is not well-pronounced in the SEM image due to the small grain size of the oxides. A thin oxide scale, which is relatively smooth, is formed. By increasing the temperature to 700°C the oxide grains grow and the film thickens. After a treatment at 800°C, the surface is covered with larger oxide islands and the oxide grain growth rises dramatically for the ternary alloy. This is in good agreement with the results of the TG analysis which revealed a rapid increase in mass at temperatures ≥800°C. These features are less pronounced for the quaternary alloy. It shows a more retarded oxide grain growth which is also in accordance with TG results revealing a retarded mass gain due to oxidation. The Nb effect was discussed above and is confirmed here again. This surface morphology study suggests that once the samples are in contact with oxygen at elevated temperatures, the nucleation of oxides occurs throughout the whole surface. An initial formation of a thin rather smooth oxide scale is followed by agglomeration processes and growth of single oxide grains which cover the surface at the end completely. The kinetics of oxide film thickening and grain growth is not only determined by the annealing temperature but also by the alloy composition.
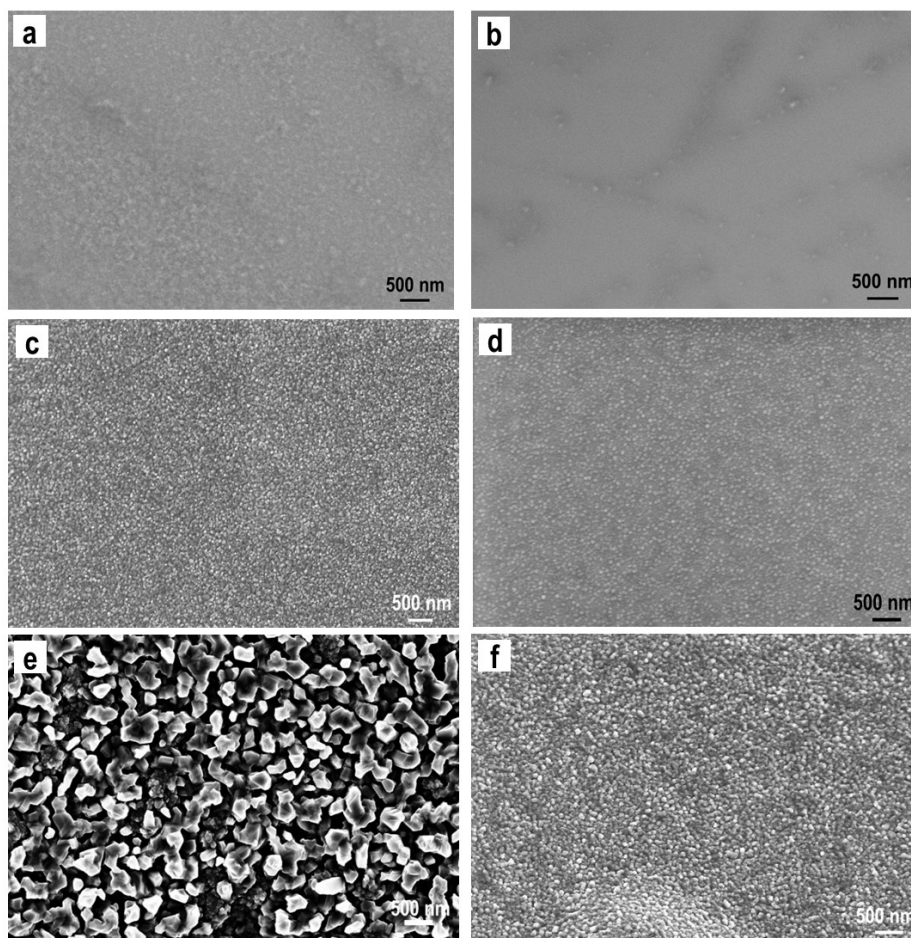
Figure 4.27: Scanning electron micrographs showing surface morphologies of Ti$_{75}$Zr$_{10}$Si$_{15}$ (a, c, e) and Ti$_{60}$Zr$_{10}$Nb$_{15}$Si$_{15}$ (b, d, f) melt-spun ribbons oxidized at 550°C (a, b), 700 °C (c, d) and 800°C (e, f) for 3 hours in synthetic air.

Similar explanations have been reported by Garcia-Alonso et al. [165] for the Ti6Al4V alloy thermally oxidized at 700°C for 1 h and by Kumar et al. [174] for cp-Ti, which was oxidized at 500, 650 and 800°C for 24 h.

4.4.3 Detailed investigation of melt-spun ribbons oxidized at 550°C for 3 hours

As has been mentioned before (see section 2.2.3), surface modification techniques are used to improve the compatibility between living tissue and implant. Surface properties could control the amount and quality of cell adhered to the implant and, therefore, the tissue growth. Thermal treatment is affecting the surface morphology by forming rough and porous surface oxides which is expected to increase the bone tissue ingrowth [70]. It has been shown that a suitable surface roughness can lead to a successful osseointegration of Ti-based implants and affect the

osteoblast differentiation, proliferation and matrix production [175,176]. In the present study, the metastable Ti(-Nb)-Zr-Si alloys were found to preserve their glass-matrix nanocomposite microstructure without any significant crystallization only at temperatures below the onset of the second crystallization event, i.e. below 590°C (see DSC data). Therefore, for applications only thermal oxidation treatments below this temperature limit are useful, despite the fact that the oxide growth is rather slow. In the following, the initial oxidation states on the melt-spun ternary and quaternary alloy surfaces, obtained after thermal treatment at 550°C for 3 hours in synthetic air were characterized in more detail using high resolution methods.

Atomic force microscopy (AFM): AFM has been applied to study the surface morphology and to analyze the surface roughness of the treated alloy samples. In Fig. 4.28, typical AFM images of melt-spun ribbons (as-prepared state) and of thermally treated samples (at 550°C for 3 hours in synthetic air) of $Ti_{75}Zr_{10}Si_{15}$ and $Ti_{60}Zr_{10}Nb_{15}Si_{15}$ are shown.
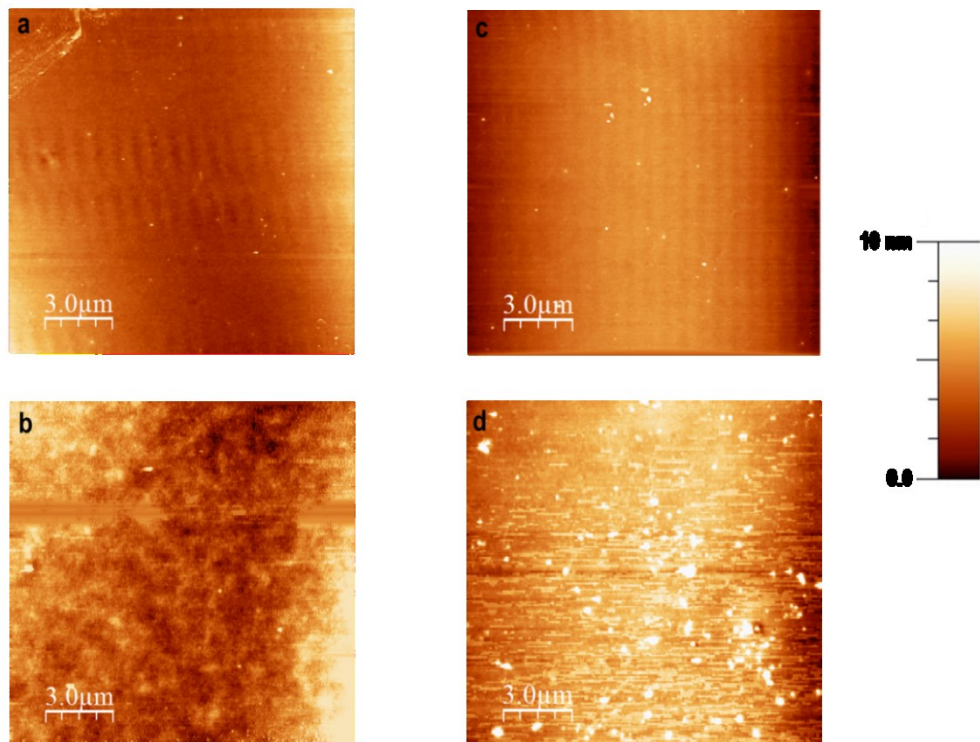

Figure 4.28: AFM images of a) as-spun and, b) thermally treated ribbon samples of $Ti_{75}Zr_{10}Si_{15}$; c) as-spun and, d) thermally treated ribbon samples of $Ti_{60}Zr_{10}Nb_{15}Si_{15}$ (air-sides).

Results and discussion

On the air-side of the ribbon samples probe areas of 15 μm × 15 μm were chosen. The surface roughness of the treated sample $Ti_{75}Zr_{10}Si_{15}$ is increased in comparison with the untreated (melt-spun) one, which suggests that it is nearly homogeneously oxidized and the general oxide particle size is below 3 nm. In contrast, a treated $Ti_{60}Zr_{10}Nb_{15}Si_{15}$ sample is non-homogeneously oxidized with a particle size up to 30 nm. This may be a consequence of the lower oxidation rate of the quaternary alloy (see section 4.4.1).

The statistical analysis which gives r.m.s. (root mean squared) roughness values are reported in Table 4.4. The roughness values of surfaces of the as-spun samples and of the thermally treated ones are in the same nanometer range. The presence of the metal oxides on the treated surfaces increases the roughness in comparison with the untreated ribbons by a factor of almost 2.

Table 4.4: r.m.s. roughness values for as-spun and thermally treated $Ti_{75}Zr_{10}Si_{15}$ and $Ti_{60}Zr_{10}Nb_{15}Si_{15}$ samples (air-sides), obtained by AFM (scanned area: 15 μm × 15 μm).

	r.m.s. roughness (nm)	
sample	as-spun	treated
$Ti_{75}Zr_{10}Si_{15}$	1.35 ± 0.2	2.43 ± 0.2
$Ti_{60}Zr_{10}Nb_{15}Si_{15}$	1.03 ± 0.2	2.03 ± 0.2

The amount of the formed nuclei and the growth rate of the oxide grains define the values of the available surface area (surface roughness) of the oxidized samples. In case of the $Ti_{60}Zr_{10}Nb_{15}Si_{15}$ sample, according to the lower oxidation rate due to the presence of Nb, the applied duration (3h) seems to be not sufficient to completely cover the surface as it is achieved in the case of the $Ti_{75}Zr_{10}Si_{15}$ sample. This corresponds well to results of the SEM imaging (see Fig. 4.27).

TEM studies: The oxide film thickness and structure has been investigated by TEM and energy dispersive X-ray (EDX) spectroscopy. In Fig. 4.29, STEM and high resolution images of cross sectional regions of thermally oxidized $Ti_{75}Zr_{10}Si_{15}$ (a, b) and $Ti_{60}Zr_{10}Nb_{15}Si_{15}$ (c, d) surfaces are shown. In STEM images of both alloy samples, three regions are observed. The EDX results reveal that the dark regions correspond to the oxides and the bright region to the alloy substrate. The average chemical composition of the oxide layers measured by EDX for the treated $Ti_{75}Zr_{10}Si_{15}$ ribbon is Ti = 30 at.-%, O = 61 at.-%, Zr = 4 at.-%, Si = 5 at.-% for region (I) and

Ti = 35 at.-%, O = 48 at.-%, Zr = 7 at.-%, Si = 10 at.-% for region (II). According to the EDX analysis, the outer region of the oxide mainly consists of TiO_2, while in the inner region a decreasing O/Ti ratio can indicate the presence of TiO or Ti_2O_3 as well. In addition, the existence of other alloying element species in the oxide layers is identified. The film thickness is estimated as ~560 nm for $Ti_{75}Zr_{10}Si_{15}$ and ~460 nm for $Ti_{60}Zr_{10}Nb_{15}Si_{15}$. The oxide layers have been investigated by high resolution TEM and representative images are shown in Fig. 4.30(b, d). The oxide layers exhibit mainly an amorphous structure (confirmed by SAED diffraction pattern, inset of Fig 4.29(b, d)).
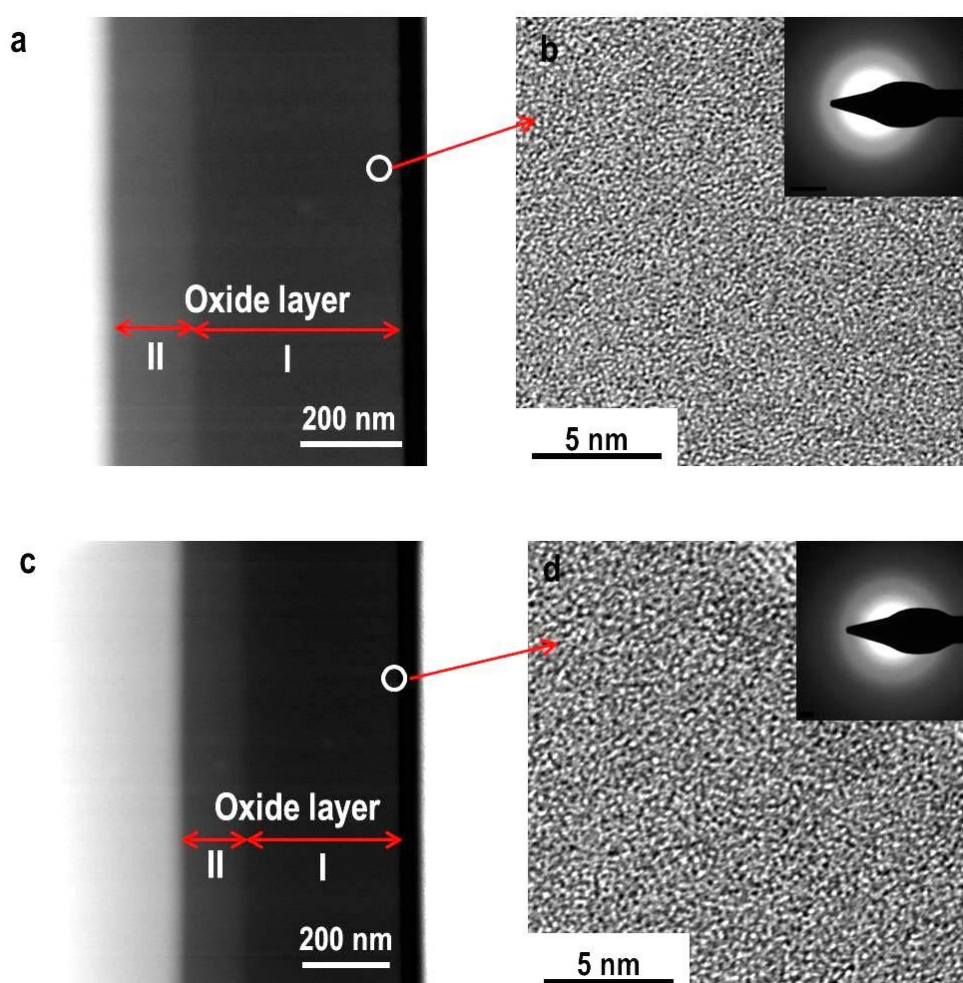

Figure 4.29: : a) STEM, b) high resolution TEM micrograph of a $Ti_{75}Zr_{10}Si_{15}$ and c) STEM, d) high resolution TEM micrograph of a $Ti_{60}Zr_{10}Nb_{15}Si_{15}$ ribbon; the ribbons are thermally oxidized at 550°C for 3 hours.

AES investigations: For a further detailed compositional characterization of the oxide films that form on the glass-forming Ti(-Nb)-Zr-Si alloys under thermal oxidation conditions, AES sputter depth-profiling was conducted. Figure 4.30 summarizes exemplary depth profiles of $Ti_{75}Zr_{10}Si_{15}$ and $Ti_{60}Zr_{10}Nb_{15}Si_{15}$ sample surfaces thermally oxidized at 550°C for 3 hours. Due to the high thickness of the oxide film, two sputtering rates have been applied. For the first 3 to 5 min, a sputter rate of 6.6 nm/min was used (Fig. 4.30(a, c)). Then, for the following 90 min, a sputter rate of 17 nm/min in silicon oxide (Fig. 4.30(b, d)) was used. The AES profiles of the surface regions of both alloy samples (Fig. 4.30) reveal that all constituent element species are present in the oxide layers. They consist mainly of Ti oxide with some contribution of the other elements.
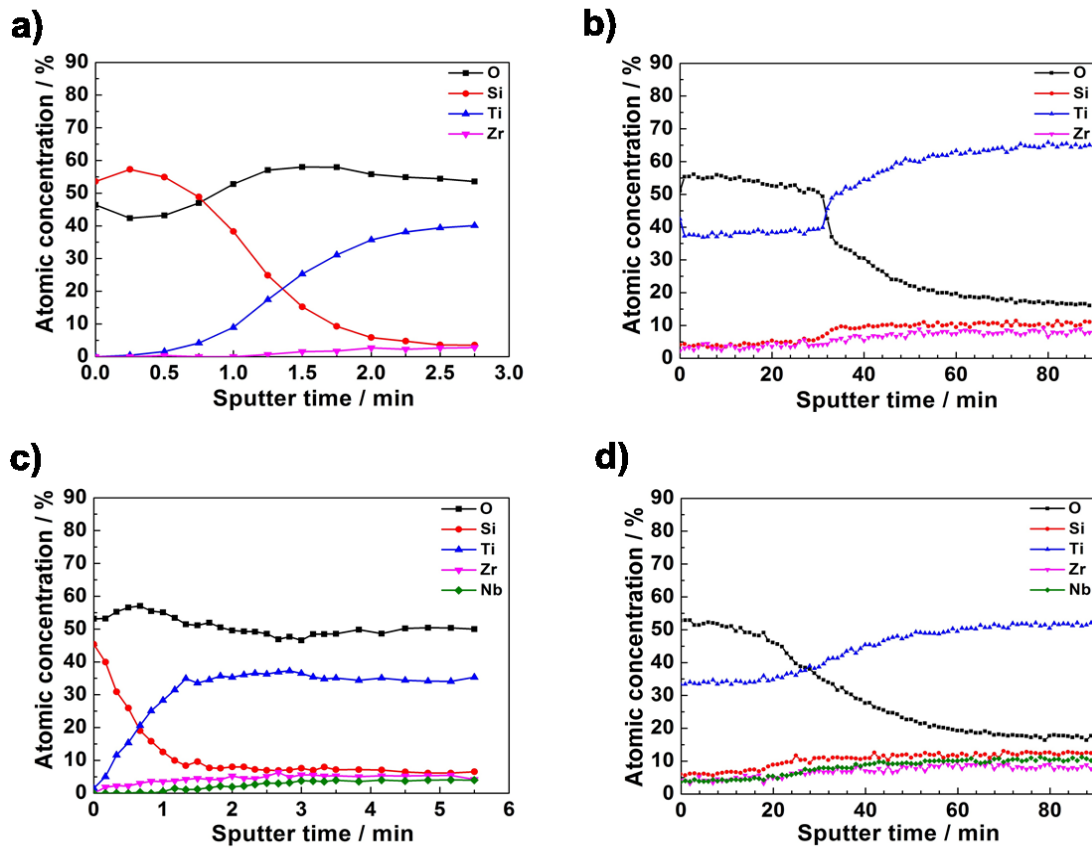
Figure 4.30: Elemental concentration sputter depth profiles obtained from AES measurements at surfaces (airside) of $Ti_{75}Zr_{10}Si_{15}$ divided by different sputter rates in a surface region (a – first 2.7 min sputtering = 18 nm depth) and the subsequent bulk-near region (b - following 90 min sputtering = 1500 nm). For $Ti_{60}Zr_{10}Nb_{15}Si_{15}$ ribbons similar results are shown for the first 36 nm (c) and the following 1500 nm (d).

Within the first 60 seconds of sputtering the silicon concentration is higher than that of other elements, which indicates the presence of a very thin silicon oxide layer (about 6.6 nm) in the outermost zone. According to the thermodynamic aspect, SiO_2 has a less negative heat of formation in comparison with the other oxides so the driving force of oxide formation is smaller for SiO_2 but its growth kinetics is faster [177].

By increasing the sputter time to about 35 min, the oxygen signal decays to the half width value between maximum and minimum value which was defined as oxide/metal interface. Considering the different sputter rates and the corresponding times, the oxide thickness on the ternary alloy is estimated to be ~560 nm. For the quaternary alloy sample, the film thickness decreases. The film consists of the silicon oxide layer of about 3 nm on the outer surface and the oxide film layer of about 465 nm. It can be seen that the determined film thickness values for $Ti_{75}Zr_{10}Si_{15}$ and $Ti_{60}Zr_{10}Nb_{15}Si_{15}$ are in good agreement with those estimated from TEM results. No sharp decay of the oxygen concentration can be perceived for the $Ti_{60}Zr_{10}Nb_{15}Si_{15}$ sample, which points to a higher roughness of the oxide in the investigated region.

Microhardness: A high hardness of implant surfaces is demanding to reduce wear rates especially in articulation joint applications. The measured microhardness values of as-spun and thermally oxidized samples (airside of ribbons) are given in Table 4.5. The lowest load of 10 gf (which provides a depth of about 1 μm) has been applied to be able to evaluate mainly the effect of the surface oxide layer (~500-600 nm) on the hardness. The microhardness values of as-spun samples of $Ti_{75}Zr_{10}Si_{15}$ and $Ti_{60}Zr_{10}Nb_{15}Si_{15}$ are 690 and 691 $H_{V0.01}$, respectively. The thermally oxidized samples reveal a significant increase in hardness by about two times due to the formation of harder oxide layers. The higher scattering of values for treated samples may be due to the formation of oxide islands, and in consequence, to lateral inhomogeneities and to an increased surface roughness.

Table 4.5: Results of surface microhardness testing (Vickers indenter: 10 gf applied load) of as-spun and thermally treated $Ti_{75}Zr_{10}Si_{15}$ and $Ti_{60}Zr_{10}Nb_{15}Si_{15}$ ribbons (air-sides) at 550°C for 3 hours.

sample	microhardness ($H_{V0.01}$)	
	as-spun	treated
$Ti_{75}Zr_{10}Si_{15}$	602 ± 21	1285 ± 89
$Ti_{60}Zr_{10}Nb_{15}Si_{15}$	601 ± 36	1287 ± 91

Wettability: The wettability describes the tendency of a liquid to spread out on a solid surface. When a biomaterial is implanted into a biological system, the first and the foremost event is the wetting of the implant material by the physiological fluids. This further determines the degree and confirmation of specific proteins which in turn influence recruitment and activation of cells and stimulation of new tissue development [178].

Topography and chemistry play an important role in the wettability of solid surfaces. The presence of metal oxides on the surface of modified samples affects both parameters and, as a consequence, the wettability of the samples. The surface contact angles of the samples are evaluated by sessile drop measurements of distilled water at room temperature and the results are summarized in Table 4.6. It can be seen that contact angles for as-spun samples and for the treated ones are in the same range which is in good agreement with surface roughness results. The oxides formed thermally on the sample surfaces reduce the contact angle values to about 73°. It can be concluded that the thermal treatment increases the hydrophilicity of the modified sample surfaces. Oxidized surfaces result in more OH groups and water molecules adsorbed, which can positively contribute to the interactions with proteins and cells.

Table 4.6: Contact angle (CA) values measured on as-spun and thermally treated $Ti_{75}Zr_{10}Si_{15}$ and $Ti_{60}Zr_{10}Nb_{15}Si_{15}$ ribbons (air-sides).

sample	CA (°)	
	as-spun	treated
$Ti_{75}Zr_{10}Si_{15}$	$85° \pm 2°$	$73° \pm 2°$
$Ti_{60}Zr_{10}Nb_{15}Si_{15}$	$92° \pm 2°$	$74° \pm 2°$

4.4.4 SBF test (apatite-forming ability)

The analysis of hydroxyapatite formation on a material in a simulated body fluid (SBF) may be used as a preliminary in vitro assessment of the bone forming bioactivity of that material [130]. Therefore, the ability of the melt-spun $Ti_{75}Zr_{10}Si_{15}$ and $Ti_{60}Zr_{10}Nb_{15}Si_{15}$ alloys to generate hydroxyapatite at their surface (air-side of ribbon samples) was tested and compared with that of cp-Ti. Samples of those three materials were immersed in the SBF solution for 10, 20 and 30 days. Subsequently, their surface was investigated by SEM and EDX. Selected SEM images are shown in Fig. 4.30. Highly porous layers developed by overlapping of

hemispherical growth centres. EDX analysis (spectra not shown here) revealed the presence of both Ca and P in those layers indicating that they consist of hydroxyapatite. The growth of the hydroxyapatite layer appears to occur at similar rates on cp-Ti and on the melt-spun $Ti_{75}Zr_{10}Si_{15}$ alloy: after 10 days they show a similar morphology of the hydroxyapatite layer (see Fig. 4.31(a, b)). However, the growth rate on the $Ti_{60}Zr_{10}Nb_{15}Si_{15}$ alloy is significantly lower. As Fig. 4.31(c) shows, after 10 days of exposure to the SBF solution, only a few small porous growth centres were detected (this is similar after 20 days). Nevertheless, after 30 days (see Fig. 4.31(d)) the $Ti_{60}Zr_{10}Nb_{15}Si_{15}$ alloy also forms a thick layer of hydroxyapatite.

It is concluded, that the melt-spun $Ti_{75}Zr_{10}Si_{15}$ alloy has an apatite-forming ability which is similar to that of cp-Ti. For the melt-spun $Ti_{60}Zr_{10}Nb_{15}Si_{15}$ alloy, the formation of hydroxyapatite is retarded, suggesting that additions of Nb inhibit the apatite-forming ability of Ti-based alloys. This is in agreement with previous studies on β-phase alloys which also revealed a reduced rate of the apatite-forming ability when adding 45 wt.-% Nb to pure Ti [179].

In addition, SBF tests have been conducted on $Ti_{75}Zr_{10}Si_{15}$ and $Ti_{60}Zr_{10}Nb_{15}Si_{15}$ ribbons which were thermally oxidized at 550°C for 3 hours in order to investigate the hydroxyapatite forming ability. Similarly to untreated ribbons, samples were immersed in SBF solution for 10 or 20 days and their surface was investigated by SEM and EDX. In Fig. 4.32 selected SEM images are shown. SEM images and the EDX analysis reveal that sample surfaces in the thermally treated state in comparison with the untreated surface state are covered with a relatively compact hydroxyapatite layer already after 10 days. Further, for $Ti_{60}Zr_{10}Nb_{15}Si_{15}$ the thermal oxidation treatment results in a higher growth (Fig. 4.32(c, d)).

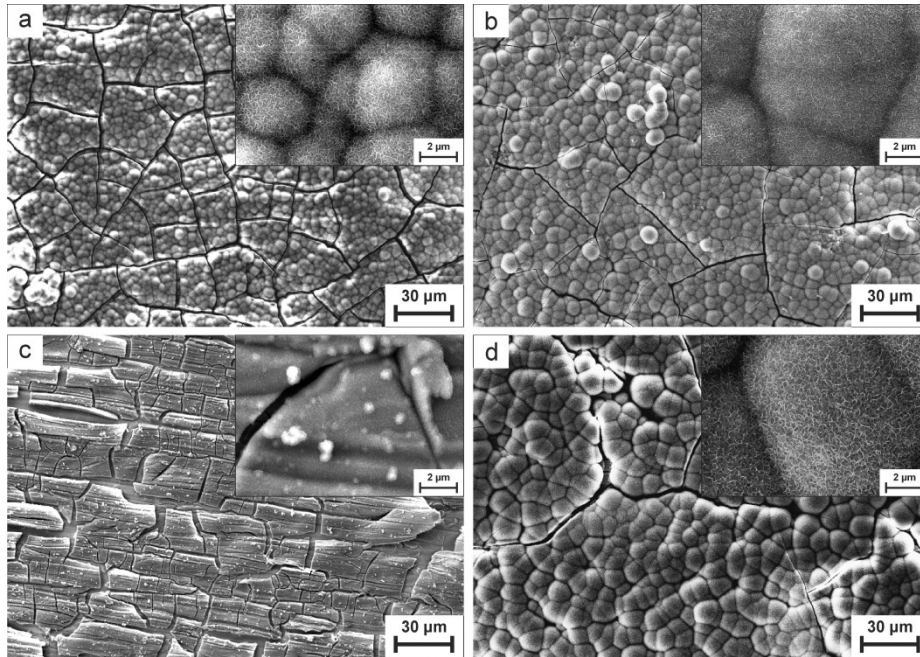Figure 4.31: SEM images of surfaces of cp-Ti, $Ti_{75}Zr_{10}Si_{15}$ and $Ti_{60}Zr_{10}Nb_{15}Si_{15}$ ribbon samples (air-side) treated with NaOH and immersed in SBF solution for different durations: (a) cpTi /10 days, (b) $Ti_{75}Zr_{10}Si_{15}$ /10 days, (c) $Ti_{60}Zr_{10}Nb_{15}Si_{15}$ /10 days, and (d) $Ti_{60}Zr_{10}Nb_{15}Si_{15}$ / 30 days.
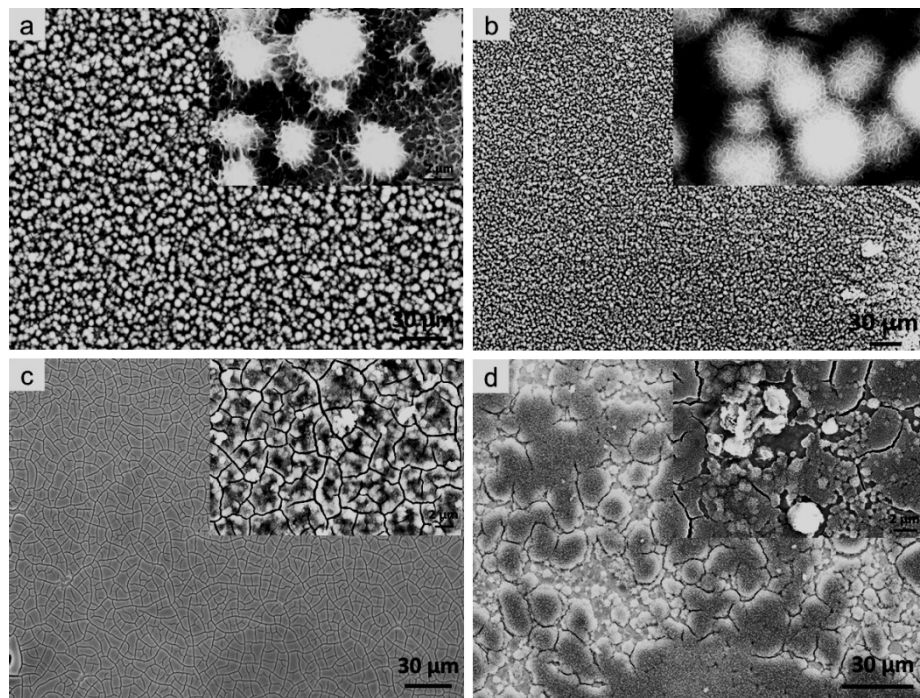
Figure 4.32: SEM images of surfaces of untreated and thermally oxidized $Ti_{75}Zr_{10}Si_{15}$ and $Ti_{60}Zr_{10}Nb_{15}Si_{15}$ ribbon smaples (air-side) treated with NaOH and immersed in SBF solution for 10 days: (a) $Ti_{75}Zr_{10}Si_{15}$ (b) thermally oxidized $Ti_{75}Zr_{10}Si_{15}$ (c) $Ti_{60}Zr_{10}Nb_{15}Si_{15}$ and (d) thermally oxidized $Ti_{60}Zr_{10}Nb_{15}Si_{15}$.

Results and discussion

Summary: It has been demonstrated that thermal oxidation which is one of the simple and cost-effective surface modification methods could be well applied to $Ti_{75}Zr_{10}Si_{15}$ and $Ti_{60}Zr_{10}Nb_{15}Si_{15}$ melt-spun ribbons. Oxidation rates significantly increase at temperatures $\geq$ 400°C, where oxidation follows a parabolic growth law. Substitution of Ti by Nb in the alloy composition retards the oxidation process at a given temperature. At temperatures higher than 590°C surface oxidation superimposes significant crystallization events. Therefore, surface modification by thermal oxidation is only feasible in a temperature window of 400°C< $T_{oxidation}$ <590°C.

In first tests, ribbon samples of the ternary and the quaternary alloy which were oxidized at 550°C in synthetic air showed suitable fundamental properties for implant applications, i.e. high hardness, good wettability and hydroxyapatite-forming ability after 10 days.

5 Summary and outlook

Ti-based metallic glass-forming alloys are currently attracting increasing interest to be used in biomedical applications due to their superior mechanical properties such as very high strength (1800–2500 MPa), relatively low Young's modulus (80-110 GPa), low density and higher wear resistance relative to their crystalline counterparts and to conventional Ti-based materials [20,82,85]. However, a biomedical application of these alloys is restricted by the presence of cytotoxic or allergic elements such as Al, Ni, Be and Cu [15,16] in their composition which could be released as ions or metal particles from metal implants into the body tissue [5]. Consequently, the use of non-toxic elements which support stable passivity must have priority in the development of new glass-forming biomaterials.

In this work, new glass-forming Ti-Zr-(Nb)-Si alloys, which are completely free of cytotoxic elements, have been developed. Effects of the cooling rate on the microstructure evolution of $Ti_{75}Zr_{10}Si_{15}$ and $Ti_{60}Zr_{10}Nb_{15}Si_{15}$ cast rods and melt-spun ribbons have been investigated. The effects of Nb addition on the phase formation and the mechanical properties have been assessed. In the case of $Ti_{75}Zr_{10}Si_{15}$, slow cooling provides fully crystalline rods consisting of the S1 intermetallic phase and an eutectic of S1 and α-Ti phase. The Nb addition yields a microstructure comprising the S1 phase and an eutectic of S1 and β-Ti(Nb) phase. Rapidly quenched ribbons of the ternary alloy exhibit a nanocomposite structure of β-Ti nanocrystals being embedded in a glassy matrix. Results reflect also a cooling-rate-dependent microstructural gradient over the ribbon cross-section. Nanocrystalline β-Ti is mainly precipitated at the air-side due to the local lower cooling rate. Increasing the overheating temperature results in an increase of the amorphous phase fraction over the ribbons cross-section. Adding Nb to create the $Ti_{60}Zr_{10}Nb_{15}Si_{15}$ alloy increases the glass-forming ability of the system, as expressed in an increase of the amorphous phase fraction at both sides of the ribbon. At an overheating temperature of 2053 K, a nearly fully glassy structure is obtained. Mechanical property investigations revealed that Nb has the main effect of decreasing Young's modulus of the crystalline alloy as well as its hardness, which is due to the stabilization of a significant fraction of a β-type phase.

For long-term use as implant material in the human body, it is essential to assess the corrosion properties of those new alloys in comparison to other potential materials, i.e. single phase α-Ti or β-Ti-40Nb. Therefore, the corrosion and passivation behavior of glass-forming $Ti_{75}Zr_{10}Si_{15}$

and $Ti_{60}Zr_{10}Nb_{15}Si_{15}$ alloys in simulated body fluid (Ringer solution) at 310 K was studied. The results exhibit that glass-forming $Ti_{75}Zr_{10}Si_{15}$ and $Ti_{60}Zr_{10}Nb_{15}Si_{15}$ alloys appear to be very good candidates for long-term biomedical applications due to their proven high stability of their passive states in a simulated body fluid. A homogeneous constituent distribution in the melt-spun alloy states with a mainly glassy matrix and a few embedded β-Ti nanocrystals is beneficial for preserving a uniform passivity. The addition of Nb does not only improve the glass-forming ability and the mechanical properties but also supports a high pitting resistance even under extreme anodic polarization conditions. Thus, with regard to the corrosion properties the Nb-containing nearly single-phase glassy alloy can compete with the single-phase β-type Ti-40Nb alloy.

Finally, in order to improve the biological properties of alloys as potential biomaterials, an appropriate surface modification (thermal oxidation) has been applied. Thermal oxidation treatment aims for providing a Ti oxide layer on the surface of the alloys to increase hardness, wear resistance, surface roughness and wettability. The accomplished studies reveal that a temperature window of 400°C< $T_{oxidation}$ <590°C is suitable for thermal oxidation. Although the Nb addition retards the oxidation process at a given temperature, an optimized exposure time could be a feasible way to accomplish an effective thermal oxidation process. The modified surfaces not only exhibit higher hardness, surface roughness and wettability of both alloys but also increase the growth rate of hydroxyapatite on the surface of the Nb-containing alloy.

Glass-forming $Ti_{75}Zr_{10}Si_{15}$ and $Ti_{60}Zr_{10}Nb_{15}Si_{15}$ alloys, which are free of toxic elements appear to be very good candidates for long-term biomedical applications due to their interesting combination of mechanical properties, corrosion behavior and surface modification sufficiency.

Outlook

1) This study reveals that the glass-forming ability of those valve metal Si-based alloy systems will remain limited and restricts their production to melt metallurgical processing technologies with high cooling rates like melt-spinning or splat quenching. That limits their applicability. The following perspectives are suggested:

- Ti(-Nb)-Zr-Si alloys with glassy or nanocomposite structure may be produced as sputter-deposited thin films with high wear and corrosion resistance on cp-Ti or Ti-6Al-4V implant surfaces to improve their durability.

- Ti(-Nb)-Zr-Si alloys may be produced as amorphous powders by means of gas atomization or mechanical alloying. Those alloy powders can be used as starting materials for the production of porous bodies (SLM processing, hot pressing and/or sintering with space holder phase) with a significantly reduced elastic modulus and with great potential for osseointegration.

2) So far, mechanical properties of the Ti(-Nb)-Zr-Si alloys have been only assessed under static load. For implant applications the properties under dynamic load, e.g. fatigue behavior, are decisive. This should be in the focus of future investigations with appropriate sample qualities.

3) Up to present, the biological compatibility of the new glass-forming alloys was only evaluated by SBF testing. Much more work in this regard is needed in terms of statistically relevant cell biological in vitro studies and in final consequence, of in vivo studies.

4) Early studies on commercial Ti-based implant materials revealed a broad spectrum of surface modification techniques for an improvement of the bone forming activity and of the anchoring between implant and bone tissue. For glass-forming materials only first attempts in this direction were done. Of particular interest are modifications at the nano-scale, as this matches with the micro structural features of the new alloys. For example, oxide nanotube formation was successfully demonstrated and should be continued.

Acknowledgements

References

[1] M. Niinomi, *Recent metallic materials for biomedical applications*, Metall. Mater. Trans. A, **33** (2002) 477-486.

[2] F. Variola, F. Vetrone, L. Richert, P. Jedrzejowski, J.H. Yi, S. Zalzal, S. Clair, A. Sarkissian, D.F. Perepichka, J.D. Wuest, F. Rosei, A. Nanci, *Improving biocompatibility of implantable metals by nanoscale modification of surfaces: an overview of strategies, fabrication methods, and challenges.*, Small., **5** (2009) 996–1006.

[3] M. Niinomi, *Metals for Biomedical Devices*, CRC Press, 2010.

[4] M. Geetha, A.K. Singh, R. Asokamani, A.K. Gogia, *Ti based biomaterials, the ultimate choice for orthopaedic implants – A review*, Prog. Mater. Sci. **54** (2009) 397-425.

[5] Y. Okazaki, E. Gotoh, *Comparison of metal release from various metallic biomaterials in vitro*, Biomaterials, **26** (2005) 11-21.

[6] S. Hanada, H. Matsumoto, S. Watanabe, *Mechanical compatibility of titanium implants in hard tissues*, Int. Congr. Ser., 1284 (2005) 239-247.

[7] A. Helth, P.F. Gostin, S. Oswald, H. Wendrock, U. Wolff, U. Hempel, S. Arnhold, M. Calin, J. Eckert, A. Gebert, *Chemical nanoroughening of Ti40Nb surfaces and its effect on human mesenchymal stromal cell response*, J. Biomed. Mater. Res. B, **102** (2014) 31-34.

[8] J.J. Oak, D.V. Louzguine-Luzgin, A. Inoue, *Investigation of glass-forming ability, deformation and corrosion behavior of Ni-free Ti-based BMG alloys designed for application as dental implants*, Mater. Sci. Eng. C-Mater. Biol. Appl., **29** (2009) 322-327.

[9] J.J. Oak, D.V. Louzguine-Luzgin, A. Inoue, *Fabrication of Ni-free Ti-based bulk-metallic glassy alloy having potential for application as biomaterial, and investigation of its mechanical properties, corrosion, and crystallization behavior*, J. Mater. Res., **22** (2007) 1346-1353.

[10] S.L. Zhu, X.M. Wang, F.X. Qin, A. Inoue, *A new Ti-based bulk glassy alloy with potential for biomedical application*, Mat. Sci. Eng. A-Struct., **459** (2007) 233-237.

[11] J.J. Oak, A. Inoue, *Formation, mechanical properties and corrosion resistance of Ti–Pd base glassy alloys*, J. Non-cryst. Solids, **354** (2008) 1828-1832.

[12] A. Inoue, A. Takeuchi, *Recent development and application products of bulk glassy alloys*, Acta Mater., **59** (2011) 2243-2267.

[13] J.M. Park, G. Wang, S. Pauly, N. Mattern, D.H. Kim, J. Eckert, *Ductile Ti-Based Bulk Metallic Glasses with High Specific Strength*, Metall. Mater. Trans. A, **42** (2011) 1456-1462.

[14] S.L. Zhu, X.M. Wang, F.X. Qin, M. Yoshimura, A. Inoue, *Effects of Si addition on the glass-forming ability, glass transition and crystallization behaviors of $Ti_{40}Zr_{10}Cu_{36}Pd_{14}$ bulk glassy alloy*, Intermetallics, **16** (2008) 609-614.

[15] W.M. Elshahawy, I. Watanabe, P. Kramer, *In vitro cytotoxicity evaluation of elemental ions released from different prosthodontic materials*, Dent. Mater., **25** (2009) 1551-1555.

[16] M. Calin, A. Gebert, A.C. Ghinea, P.F. Gostin, S. Abdi, C. Mickel, J. Eckert, *Designing biocompatible Ti-based metallic glasses for implant applications*, Mater. Sci. Eng. C-Mater. Biol. Appl., **33** (2013) 875-883.

References

[17] M. Atapour, A.L. Pilchak, G.S. Frankel, J.C. Williams, *Corrosion behavior of beta titanium alloys for biomedical applications*, Mater. Sci. Eng. C-Mater. Biol. Appl., **31** (2011) 885-891.

[18] S. Yang, D.C. Zhang, M. Wei, H.X. Su, W. Wu, J.G. Lin, *Effects of the Zr and Mo contents on the electrochemical corrosion behavior of Ti22Nb alloy*, Mater. Corros., **64** (2013) 402-407.

[19] B.L. Wang, Y.F. Zheng, L.C. Zhao, *Effects of Hf content and immersion time on electrochemical behavior of biomedical Ti-22Nb-xHf alloys in 0.9% NaCl solution*, Mater. Corros., **60** (2009) 330-335.

[20] C. Suryanarayana, A. Inoue, *Bulk Metallic Glasses*, CRC Press, United States of America, 2011.

[21] D.B. Miracle, T. Egami, K.M. Flores, K.F. Kelton, *Structural Aspects of Metallic Glasses*, MRS Bulletin, 32 (2007) 629-634.

[22] A.L. Greer, E. Ma, *Bulk Metallic Glasses: At the Cutting Edge of Metals Research*, MRS Bull., **32** (2007) 611-619.

[23] J.D. Bernal, *Geometry of the Structure of Monatomic Liquids*, Nature, **185** (1960) 68-70.

[24] P.H. Gaskell, *A new structural model for amorphous transition metal silicides, borides, phosphides and carbides*, J. Non-cryst. Solids, **32** (1979) 207-224.

[25] D.B. Miracle, *A structural model for metallic glasses*, Nat Mater, 3 (2004) 697-702.

[26] H.W. Sheng, W.K. Luo, F.M. Alamgir, J.M. Bai, E. Ma, *Atomic packing and short-to-medium-range order in metallic glasses*, Nature, 439 (2006) 419-425.

[27] D. Turnbull, *Under what conditions can a glass be formed?*, Contemp. Phys., **10** (1969) 473-488.

[28] R. W Cahn, P. Haasen, *PHYSICAL METALLURGY*, Elsevier Science B.V., 1996.

[29] T. Egami, Y. Waseda, *Atomic size effect on the formability of metallic glasses*, J. Non-cryst. Solids, **64** (1984) 113-134.

[30] T. Egami, *Universal criterion for metallic glass formation*, Mat. Sci. Eng. A-Struct., **226–228** (1997) 261-267.

[31] D.B. Miracle, *The efficient cluster packing model – An atomic structural model for metallic glasses*, Acta Mater., **54** (2006) 4317-4336.

[32] Z.P. Lu, C.T. Liu, *A new glass-forming ability criterion for bulk metallic glasses*, Acta Mater., 50 (2002) 3501-3512.

[33] J. Eckert, J. Das, S. Pauly, C. Duhamel, *Processing routes, microstructure and mechanical properties of metallic glasses and their composites*, Adv. Eng. Mater., **9** (2007) 443-453.

[34] U. Kühn, N. Mattern, A. Gebert, M. Kusy, M. Boström, U. Siegel, L. Schultz, *Nanostructured Zr- and Ti-based composite materials with high strength and enhanced plasticity*, J. Appl. Phys., **98** (2005).

[35] H. Choi-Yim, R.D. Conner, F. Szuecs, W.L. Johnson, *Processing, microstructure and properties of ductile metal particulate reinforced $Zr_{57}Nb_5Al_{10}CU_{15.4}Ni_{12.6}$ bulk metallic glass composites*, Acta Mater., **50** (2002) 2737-2745.

[36] A. Gebert, U. Kuehn, S. Baunack, N. Mattern, L. Schultz, *Pitting corrosion of zirconium-based bulk glass-matrix composites*, Mat. Sci. Eng. A-Struct., **415** (2006) 242-249.

[37] K.R. Lim, J.M. Park, S.S. Jee, S.Y. Kim, S.J. Kim, E.S. Lee, W.T. Kim, A. Gebert, J. Eckert, D.H. Kim, *Effect of thermal stability of the amorphous substrate on the amorphous oxide growth on Zr–Al–(Cu,Ni) metallic glass surfaces*, Corros. Sci., **73** (2013) 1-6.

References

[38] M. Kusy, U. Kühn, A. Concustell, A. Gebert, J. Das, J. Eckert, L. Schultz, M.D. Baro, *Fracture surface morphology of compressed bulk metallic glass-matrix-composites and bulk metallic glass*, Intermetallics, **14** (2006) 982-986.

[39] F. Spaepen, *A microscopic mechanism for steady state inhomogeneous flow in metallic glasses*, Acta Metall., **25** (1977) 407-415.

[40] H.J. Leamy, T.T. Wang, H.S. Chen, *Plastic flow and fracture of metallic glass*, Metall. Trans., **3** (1972) 699-708.

[41] W.J. Wright, R. Saha, W.D. Nix, *Deformation mechanisms of the $Zr_{40}Ti_{14}Ni_{10}Cu_{12}Be_{24}$ bulk metallic glass*, Mater. Trans., **42** (2001) 642-649.

[42] B. Yang, C.T. Liu, T.G. Nieh, M.L. Morrison, P.K. Liaw, R.A. Buchanan, *Localized heating and fracture criterion for bulk metallic glasses*, J. Mater. Res., **21** (2006) 915-922.

[43] H. Guo, J. Wen, N.M. Xiao, Z.F. Zhang, M.L. Sui, *The more shearing, the thicker shear band and heat-affected zone in bulk metallic glass*, J. Mater. Res., **23** (2008) 2133-2138.

[44] S. Scudino, B. Jerliu, K.B. Surreddi, U. Kuhn, J. Eckert, *Effect of cold rolling on compressive and tensile mechanical properties of $Zr_{52.5}Ti_5Cu_{18}Ni_{14.5}Al_{10}$ bulk metallic glass*, J. Alloy. Compd., **509** (2011) S128-S130.

[45] F.X. Qin, X.M. Wang, G.Q. Xie, S.L. Zhu, A. Kawashima, K. Asami, A. Inoue, *Microstructure and corrosion resistance of Ti-Zr-Cu-Pd-Sn glassy and nanocrystalline alloys*, Mater. Trans., **48** (2007) 167-170.

[46] F. Qin, X. Wang, S. Zhu, A. Kawashima, K. Asami, A. Inoue, *Fabrication and Corrosion Property of Novel Ti-Based Bulk Glassy Alloys without Ni*, Mater. Trans., **48** (2007) 515-518.

[47] Latanision R.M., J.C. Turn J., C. C.R., *The corrosion resistance of metallic glasses*, In Miller K. J. & Smith R. F (eds.) ICM3, vol. 2 of International Series on the Strength and Fracture of Materials and Structures (1979) 475-483.

[48] R.S. Dutta, R.T. Savalia, G.K. Dey, *Corrosion behaviour of rapidly solidified $Zr_{76}Ni_{16}Fe_8$ alloy in chloride environments*, Scripta Metall. Mater., **32** (1995) 207-212.

[49] A. Gebert, J. Eckert, L. Schultz, *Effect of oxygen on phase formation and thermal stability of slowly cooled $Zr_{65}Al_{7.5}Cu_{17.5}Ni_{10}$ metallic glass*, Acta Mater., **46** (1998) 5475-5482.

[50] B. Vishwanadh, G. Abraham, Jagannath, S. Neogy, R.S. Dutta, G.K. Dey, *Effect of Structural Defects, Surface Irregularities, and Quenched-In Defects on Corrosion of Zr-Based Metallic Glasses*, Metall. Mater. Trans. A, **40** (2009) 1131-1141.

[51] A. Concustell, N. Mattern, H. Wendrock, U. Kuehn, A. Gebert, J. Eckert, A.L. Greer, J. Sort, M.D. Baró, *Mechanical properties of a two-phase amorphous Ni–Nb–Y alloy studied by nanoindentation*, Scripta Mater., **56** (2007) 85-88.

[52] A. Gebert, P.F. Gostin, M. Uhlemann, J. Eckert, L. Schultz, *Interactions between mechanically generated defects and corrosion phenomena of Zr-based bulk metallic glasses*, Acta Mater., **60** (2012) 2300-2309.

[53] A. Gebert, A. Concustell, A.L. Greer, L. Schultz, J. Eckert, *Effect of shot-peening on the corrosion resistance of a Zr-based bulk metallic glass*, Scripta Mater., **62** (2010) 635-638.

[54] M. Pourbaix, *Atlas of Electrochemical Equilibria in Aqueous Solutions*, Pergamon Press, Oxford, 1966.

[55] M. Geetha, A.K. Singh, R. Asokamani, A.K. Gogia, *Ti based biomaterials, the ultimate choice for orthopaedic implants - A review*, Prog. Mater. Sci., **54** (2009) 397-425.

References

[56] J. Black, G. Hastings, *Handbook of biomaterials properties*, Chapman and Hall, London UK, 1998.

[57] D.F. Williams, *On the mechanisms of biocompatibility*, Biomaterials, **29** (2008) 2941-2953.

[58] N.J. Hallab, S. Anderson, T. Stafford, T. Glant, J.J. Jacobs, *Lymphocyte responses in patients with total hip arthroplasty*, J. Orthopaed. Res., **23** (2005) 384-391.

[59] B.F. Miller, K. C.B., *Encyclopedia & dictionary of medicine, nursing, & allied health*, Philadelphia, 1992.

[60] M. Viceconti, R. Muccini, M. Bernakiewicz, M. Baleani, L. Cristofolini, *Large-sliding contact elements accurately predict levels of bone–implant micromotion relevant to osseointegration*, J. Biomech., **33** (2000) 1611-1618.

[61] M.J. Yaszemski, D.J. Trantolo, K.-U. Lewandrowski, V. Hasirci, D.E. Altobelli, D.L. Wise, *Biomaterials in Orthopedics*, CRC Press, 2003.

[62] G. Sjögren, G. Sletten, J.E. Dahl, *Cytotoxicity of dental alloys, metals, and ceramics assessed by Millipore filter, agar overlay, and MTT tests*, J. Prosthet. Dent., **84** (2000) 229-236.

[63] S.H. Teoh, *Fatigue of biomaterials: a review*, Int. J. Fatigue, **22** (2000) 825-837.

[64] S. Nag, R. Banerjee, H.L. Fraser, *Microstructural evolution and strengthening mechanisms in Ti–Nb–Zr–Ta, Ti–Mo–Zr–Fe and Ti–15Mo biocompatible alloys*, Mater. Sci. Eng. C-Mater. Biol. Appl., **25** (2005) 357-362.

[65] U. Zwicker, *Investigations on the TiAl5Fe2.5 alloy as implant material*, Z. Metallkd., **77** (1986) 714-720.

[66] J.J. Polmear, *Titanium alloys, in: Light Alloys*, Edward Arnold Publications, London, 1981.

[67] F. Variola, J.B. Brunski, G. Orsini, P.T. de Oliveira, R. Wazen, A. Nanci, *Nanoscale surface modifications of medically relevant metals: state-of-the art and perspectives*, Nanoscale, **3** (2011) 335-353.

[68] X. Liu, P.K. Chu, C. Ding, *Surface modification of titanium, titanium alloys, and related materials for biomedical applications*, Mat. Sci. Eng. R, **47** (2004) 49-121.

[69] S. Minagar, C.C. Berndt, J. Wang, E. Ivanova, C. Wen, *A review of the application of anodization for the fabrication of nanotubes on metal implant surfaces*, Acta Biomater., **8** (2012) 2875-2888.

[70] T. Hanawa, *Research and development of metals for medical devices based on clinical needs*, Sci. Technol. Adv. Mat., **13** (2012).

[71] S. Kumar, T.S.N.S. Narayanan, S.G.S. Raman, S.K. Seshadri, *Thermal oxidation of CP-Ti: Evaluation of characteristics and corrosion resistance as a function of treatment time*, Mater. Sci. Eng. C-Mater. Biol. Appl., **29** (2009) 1942-1949.

[72] S. Kumar, T.S.N.S. Narayanan, S.G.S. Raman, S.K. Seshadri, *Thermal oxidation of Ti6Al4V alloy: Microstructural and electrochemical characterization*, Mater. Chem. Phys., **119** (2010) 337-346.

[73] S. Kumar, T.S.N.S. Narayanan, S.G.S. Raman, S.K. Seshadri, *Surface modification of CP-Ti to improve the fretting-corrosion resistance: Thermal oxidation vs. anodizing*, Mater. Sci. Eng. C-Mater. Biol. Appl., **30** (2010) 921-927.

[74] M.F. Lopez, J.A. Jimenez, A. Gutierrez, *Corrosion study of surface-modified vanadium-free titanium alloys*, Electrochim. Acta, **48** (2003) 1395-1401.

[75] H. Ahn, D. Lee, K.M. Lee, K. Lee, D. Baek, S.W. Park, *Oxidation behavior and corrosion resistance of Ti–10Ta–10Nb alloy*, Surf. Coat. Tech., **202** (2008) 5784-5789.

[76] X.H. Lin, W.L. Johnson, *Formation of Ti-Zr-Cu-Ni bulk metallic glasses*, J. Appl. Phys., **78** (1995) 6514-6519.

[77] T. Zhang, A. Inoue, *Thermal and mechanical properties of Ti-Ni-Cu-Sn amorphous alloys with a wide supercooled liquid region before crystallization*, Mater. Trans., **39** (1998) 1001-1006.

[78] T. Zhang, A. Inoue, *Preparation of Ti-Cu-Ni-Si-B amorphous alloys with a large supercooled liquid region*, Mater. Trans., **40** (1999) 301-306.

[79] Y.C. Kim, W.T. Kim, D.H. Kim, *Glass forming ability and crystallization behavior in amorphous $Ti_{50}Cu_{32-x}Ni_{15}Sn_3Be_x$ (x = 0, 1, 3, 7) alloys*, Mater. Trans., **43** (2002) 1243-1246.

[80] C.L. Ma, S. Ishihara, H. Soejima, N. Nishiyama, A. Inoue, *Formation of new Ti-based metallic glassy alloys*, Mater. Trans., **45** (2004) 1802-1806.

[81] J. A. Helsen, H. J. Breme, *Metals as Biomaterials*, Wiley, Chichester 1998.

[82] J.J. Oak, H. Kimura, A. Inoue, *Effects of Additional Elements on Structure, Mechanical Strength and Chemical Properties of Ni-Free Ti-Based Bulk Metallic Glasses for Biomaterials*, Adv. Mater. Res., **26-28** (2007) 785-788.

[83] G.Q. Xie, F.X. Qin, S.L. Zhu, *Recent Progress in Ti-Based Metallic Glasses for Application as Biomaterials*, Mater. Trans., **54** (2013) 1314-1323.

[84] C.H. Lin, C.H. Huang, J.F. Chuang, J.C. Huang, J.S. Jang, C.H. Chen, *Rapid screening of potential metallic glasses for biomedical applications*, Mater. Sci. Eng. C-Mater. Biol. Appl., **33** (2013) 4520-4526.

[85] J.J. Oak, A. Inoue, *Attempt to develop Ti-based amorphous alloys for biomaterials*, Mat. Sci. Eng. A-Struct., **449–451** (2007) 220-224.

[86] A. Inoue, H.M. Kimura, T. Masumoto, C. Suryanarayana, A. Hoshi, *Superconductivity of ductile Ti-Nb-Si amorphous-alloys*, J. Appl. Phys., **51** (1980) 5475-5482.

[87] A. Inoue, T. Masumoto, C. Suryanarayana, A. Hoshi, *Superconductivity of ductile Titanium-Niobium-based amorphous-alloys*, J. Phys. Colloques, **41** (1980) C8-758.

[88] O.B. Tarasova, L.S. Smirnov, L.E. Fykin, *A study of short-range order in amorphous Ti-Zr-Si alloys*, Phys. Met. Metallogr., **73** (1992) 177-180.

[89] S.N. Ishmaev, L.S. Smirnov, G.F. Syrykh, A.S. Ivanov, J. Stride, M.G. Zemlyanov, P.P. Parshin, *Vibrational spectra of Ti–Zr–Si metallic glasses*, Phys. B, **350** (2004) E1107-E1110.

[90] S.L. Zhu, X.M. Wang, F.X. Qin, M. Yoshimura, A. Inoue, *New TiZrCuPd quaternary bulk glassy alloys with potential of biomedical applications*, Mater. Trans., **48** (2007) 2445-2448.

[91] S.L. Zhu, X.M. Wang, A. Inoue, *Glass-forming ability and mechanical properties of Ti-based bulk glassy alloys with large diameters of up to 1 cm*, Intermetallics, **16** (2008) 1031-1035.

[92] S.L. Zhu, X.M. Wang, F.X. Qin, A. Inoue, *Glass-forming ability and thermal stability of Ti-Zr-Cu-Pd-Si bulk glassy alloys for biomedical applications*, Mater. Trans., **48** (2007) 163-166.

[93] F.X. Qin, X.M. Wang, G.Q. Xie, A. Inoue, *Distinct plastic strain of Ni-free Ti-Zr-Cu-Pd-Nb bulk metallic glasses with potential for biomedical applications*, Intermetallics, **16** (2008) 1026-1030.

[94] F.X. Qin, X.M. Wang, A. Inoue, *Effects of Ta on microstructure and mechanical property of Ti-Zr-Cu-Pd-Ta alloys*, Mater. Trans., **48** (2007) 2390-2394.

[95] J.C. Hornez, A. Lefèvre, D. Joly, H.F. Hildebrand, *Multiple parameter cytotoxicity index on dental alloys and pure metals*, Biomol. Eng., **19** (2002) 103–117.

References

[96] P.G. Laing, A.B. Ferguson, E.S. Hodge, *Tissue reaction in rabbit muscle exposed to metallic implants*, J. Biomed. Mater. Res., **1** (1967) 135–149.

[97] K.L. Wapner, *Implications of metallic corrosion in total knee arthroplasty*, Clin. Orthop. Rel. Res., **271** (1991) 12-20.

[98] P.M.E. In: C. Leyens, *Titanium and Titanium Alloys: Fundamentals and Applications*, Wiley-VCH Verlag GmbH & Co. KGaA, Weinheim, 2003.

[99] A. Takeuchi, A. Inoue, *Classification of bulk metallic glasses by atomic size difference, heat of mixing and period of constituent elements and its application to characterization of the main alloying element*, Mater. Trans., **46** (2005) 2817-2829.

[100] D. Kuroda, M. Niinomi, M. Morinaga, Y. Kato, T. Yashiro, *Design and mechanical properties of new β type titanium alloys for implant materials*, Mat. Sci. Eng. A-Struct., **243** (1998) 244-249.

[101] R. Jugdaohsingh, *Silicon and bone health*, J. Nutr. Health Aging, **11** (2007) 99-110.

[102] O.N. Senkov, D.B. Miracle, *Effect of the atomic size distribution on glass forming ability of amorphous metallic alloys*, Mater. Res. Bull., **36** (2001) 2183-2198.

[103] T. Massalski, *Binary Alloy Phase Diagrams*, 2nd ed. ASM International ed., 1990.

[104] M. Bulanova, S. Firstov, I. Gornaya, D. Miracle, *The melting diagram of the Ti-corner of the Ti–Zr–Si system and mechanical properties of as-cast compositions*, J. Alloy. Compd., **384** (2004) 106-114.

[105] F. Qin, Z. Dan, X. Wang, G. Xie, A. Inoue, *Ti-Based Bulk Metallic Glasses for Biomedical Applications, Biomedical Engineering, Trends in Materials Science*, Mr Anthony Laskovski (Ed.), ISBN: 978-953-307-513-6 ed., 2011.

[106] J.J. Oak, H. Kimura, A. Inoue, *Effects of Additional Elements on Structure, Mechanical Strength and Chemical Properties of Ni-Free Ti-Based Bulk Metallic Glasses for Biomaterials*, Adv. Mat. Res., **26-28** (2007) 785-788.

[107] G.Q. Xie, F.X. Qin, S.L. Zhu, D.V. Louzguine-Lugzin, *Corrosion behaviour of porous Ni-free Ti-based bulk metallic glass produced by spark plasma sintering in Hanks' solution*, Intermetallics, **44** (2014) 55-59.

[108] F.X. Qin, X.M. Wang, T. Wada, G.Q. Xie, K. Asami, A. Inoue, *Formation of Hydroxyapatite on Ti-Coated Ti-Zr-Cu-Pd Bulk Metallic Glass*, Mater. Trans., **50** (2009) 605-609.

[109] F.X. Qin, G.Q. Xie, X.M. Wang, T. Wada, M. Song, K. Furuya, M. Yoshimura, M. Tsukamoto, A. Inoue, *Microstructure and Electrochemical Properties of PVD TiN, (Ti, Al) N-Coated Ti-Based Bulk Metallic Glasses*, Mater. Trans., **50** (2009) 1313-1317.

[110] F.X. Qin, K. Wada, X.J. Yang, X.M. Wang, M. Yoshimura, K. Asami, A. Inoue, *Bioactivity of a Ni-Free Ti-Based Metallic Glass*, Mater. Trans., **51** (2010) 529-534.

[111] Y. Fukushima, K. Katsumata, S.L. Zhu, G.Q. Xie, M. Niinomi, K. Okada, N. Matsushita, *Solution Process for Synthesizing Bioactive Nano-Mesh Layer on Ti-Based Bulk Metallic Glasses*, Mater. Trans., **54** (2013) 1343-1346.

[112] T. Onoki, X. Wang, S. Zhu, Y. Hoshikawa, N. Sugiyama, M. Akao, E. Yasuda, M. Yoshimura, A. Inoue, *Bioactivity of titanium-based bulk metallic glass surfaces via hydrothermal hot-pressing treatment*, J. Ceram. Soc. Jpn., **116** (2008) 115-117.

[113] S.L. Zhu, X.J. Yang, Z.D. Cui, *Formation of Ca-P layer on the Ti-based bulk glassy alloy by chemical treatment*, J. Alloy. Compd., **504** (2010) S168-S171.

References

[114] B.D. Cullity, *Elements of X-ray diffraction*, Addison-Wesley Publishing Company, Boston, 1978.

[115] H.M. Rietveld, *A profile refinement method for nuclear and magnetic structures*, J. Appl. Crystallogr., **2** (1969) 65-&.

[116] A.P. Hammersley, S.O. Svensson, M. Hanfland, A.N. Fitch, D. Hausermann, *Two-dimensional detector software: From real detector to idealised image or two-theta scan*, High Pressure Res., **14** (1996) 235-248.

[117] W.C. Oliver, G.M. Pharr, *An improved technique for determinig hardness and elastic-modulus using load and displacement sensing indentation experiments*, J. Mater. Res., **7** (1992) 1564-1583.

[118] A. Fischer-Cripps, *Nanoindentation*, Springer-Verlag, New York, 2004.

[119] K. Tostmann, *Korrosion: Ursachen und Vermeidung*, Wiley-VCH, Germany, 2001.

[120] M.M. Lohrengel, *Thin anodic oxide layers on aluminum and other valve metals-high-field regime*, Mater. Sci. Eng. R-Rep., **11** (1993) 243-294.

[121] J.F. Moulder, W.F. Stickle, P.E. Sobol, K.D. Bomben, *Handbook of X-ray Photoelectron Spectroscopy*, Physical Electronics Inc., Eden Prarie, 1995.

[122] J. Watts, J. Wolstenholme, *An Inroduction to Surface Analysis by XPS and AES*, Wiley, 2003.

[123] S. Oswald, P. F. Gostin, A. Helth, S. Abdi, L. Giebeler, H. Wendrock, M. Calin, J. Eckert, A. Gebert, *XPS and AES sputter-depth profiling at surfaces of biocompatible passivated Ti-based alloys: Concentration quantification considering chemical effects*, Surf. Interface Anal., 46 (2014) 683-688.

[124] B.E. Deal, A.S. Grove, *General Relationship for the Thermal Oxidation of Silicon*, J. Appl. Phys., **36** (1965) 3770-3778.

[125] P. Gabbott, *Principles and Applications of Thermal Analysis*, Blackwell Publishing Ltd, UK, 2008.

[126] K. Keunjoo, L. Young Hee, A. Myung Hwan, S. Moon Suhk, Y. Chang Joo, L. Kee Bang, L. Hyung Jae, *Growth law of silicon oxides by dry oxidation*, Semicond. Sci. Tech., **11** (1996) 1059.

[127] H. Exner, *Physical Metallurgy, chap. Qualitative and Quantitative Surface Microscopy*, 4th ed., 1996.

[128] W. Heckel, O. Marti, *Atomic Force Microscopy*, 1st Ed. ed., John Wiley & Sons Ltd, 1998.

[129] K.Y. Law, *Definitions for Hydrophilicity, Hydrophobicity, and Superhydrophobicity: Getting the Basics Right*, J. Phys. Chem. Lett., **5** (2014) 686-688.

[130] T. Kokubo, H. Takadama, *How useful is SBF in predicting in vivo bone bioactivity?*, Biomaterials, **27** (2006) 2907-2915.

[131] S. Abdi, M.S. Khoshkhoo, O. Shuleshova, M. Bönisch, M. Calin, L. Schultz, J. Eckert, M.D. Baró, J. Sort, A. Gebert, *Effect of Nb addition on microstructure evolution and nanomechanical properties of a glass-forming Ti–Zr–Si alloy*, Intermetallics, **46** (2014) 156-163.

[132] N.H. Salpadoru, H.M. Flower, *Phase equilibria and transformations in a Ti-Zr-Si system*, MMTA, 26 (1995) 243-257.

[133] K. Laws, B. Gun, M. Ferry, *Influence of Casting Parameters on the Critical Casting Size of Bulk Metallic Glass*, Metall. Mater. Trans. A, **40** (2009) 2377-2387.

[134] V.I. Tkatch, A.I. Limanovskii, S.N. Denisenko, S.G. Rassolov, *The effect of the melt-spinning processing parameters on the rate of cooling*, Mat. Sci. Eng. A-Struct., **323** (2002) 91-96.

References

[135] E. Ferrara, A. Stantero, P. Tiberto, M. Baricco, D. Janickovic, L. Kubicar, P. Duhaj, *Magnetic properties and surface roughness of $Fe_{64}Co_{21}B_{15}$ amorphous ribbons quenched from different melt temperatures*, Mat. Sci. Eng. A-Struct., **226–228** (1997) 326-330.

[136] R. Boyer, G. Welsch, E.W. Collings, *Materials Properties Handbook: Titanium Alloys*, ASM International, Materials Park, OH, 1994.

[137] B.G. Yoo, J.Y. Kim, J.I. Jang, *Influence of Indenter Geometry on the Deformation Behavior of $Zr_{60}Cu_{30}Al_{10}$ Bulk Metallic Glass during Nanoindentation*, Mater. Trans., **48** (2007) 1765-1769.

[138] C.A. Schuh, T.G. Nieh, *A survey of instrumented indentation studies on metallic glasses*, J. Mater. Res., **19** (2004) 46-57.

[139] F.C. Barbieri, C. Otani, C.M. Lepienski, W.I. Urruchi, H.S. Maciel, G. Petraconi, *Nanoindentation study of Ti6Al4V alloy nitrided by low intensity plasma jet process*, Vacuum, **67** (2002) 457-461.

[140] B. Golding, B.G. Bagley, F.S.L. Hsu, *Soft Transverse Phonons in a Metallic Glass*, Phys. Rev. Lett., **29** (1972) 68-70.

[141] W.H. Wang, H.Y. Bai, J.L. Luo, R.J. Wang, D. Jin, *Supersoftening of transverse phonons in $Zr_{41}Ti_{14}Cu_{12.5}Ni_{10}Be_{22.5}$ bulk metallic glass*, Phys. Rev. B, **62** (2000) 25-28.

[142] J. Fornell, S. Suriñach, M.D. Baró, J. Sort, *Unconventional elastic properties, deformation behavior and fracture characteristics of newly developed rare earth bulk metallic glasses*, Intermetallics, **17** (2009) 1090-1097.

[143] L.E. Rehn, P.R. Okamoto, J. Pearson, R. Bhadra, M. Grimsditch, *Solid-State Amorphization of Zr_{3}Al: Evidence of an Elastic Instability and First-Order Phase Transformation*, Phys. Rev. Lett., **59** (1987) 2987-2990.

[144] A. Leyland, A. Matthews, *On the significance of the H/E ratio in wear control: a nanocomposite coating approach to optimised tribological behaviour*, Wear, **246** (2000) 1-11.

[145] E. Pellicer, A. Varea, S. Pané, B.J. Nelson, E. Menéndez, M. Estrader, S. Suriñach, M.D. Baró, J. Nogués, J. Sort, *Nanocrystalline Electroplated Cu–Ni: Metallic Thin Films with Enhanced Mechanical Properties and Tunable Magnetic Behavior*, Adv. Funct. Mater., **20** (2010) 983-991.

[146] C. Rebholz, A. Leyland, J.M. Schneider, A.A. Voevodin, A. Matthews, *Structure, hardness and mechanical properties of magnetron-sputtered titanium–aluminium boride films*, Surf. Coat. Tech., **120–121** (1999) 412-417.

[147] M. Pankuch, R. Bell, C.A. Melendres, *Composition and structure of the anodic films on titanium in aqueous solutions*, Electrochim. Acta, **38** (1993) 2777-2779.

[148] J.A. Harrison, D.E. Williams, *A note on the passive active transition of titanium in sulfuric-acid*, Electrochim. Acta, **27** (1982) 891-895.

[149] K.E. Heusler, M. Schulze, *Electron-transfer reactions at semiconducting anodic niobium oxide films*, Electrochim. Acta, **20** (1975) 237-244.

[150] M.B.J.G. Freitas, L.O.S. Bulhoes, *Breakdown and crystallization processes in niobium oxide films in oxalic acid solution*, J. Appl. Electrochem., **27** (1997) 612-615.

[151] N.T. Oliveira, S.R. Biaggio, R.C. Rocha-Filho, N. Bocchi, *Electrochemical studies on zirconium and its biocompatible alloys Ti-50Zr at.-% and Zr-2.5Nb wt.% in simulated physiologic media*, J. Biomed. Mater. Res. A, **74** (2005) 397-407.

[152] M. Metikoš-Huković, A. Kwokal, J. Piljac, *The influence of niobium and vanadium on passivity of titanium-based implants in physiological solution*, Biomaterials, **24** (2003) 3765-3775.

References

[153] C. Sittig, M. Textor, N.D. Spencer, M. Wieland, P.H. Vallotton, *Surface characterization of implant materials c.p. Ti, Ti-6Al-7Nb and Ti-6Al-4V with different pretreatments*, J. mater. Sci.- Mater. M, **10** (1999) 35-46.

[154] I. Milošev, T. Kosec, H.H. Strehblow, *XPS and EIS study of the passive film formed on orthopaedic Ti–6Al–7Nb alloy in Hank's physiological solution*, Electrochim. Acta, **53** (2008) 3547-3558.

[155] V.V. Atuchin, I.E. Kalabin, V.G. Kesler, N.V. Pervukhina, *Nb 3d and O 1s core levels and chemical bonding in niobates*, J. Electron Spectrosc., **142** (2005) 129-134.

[156] Y. Tsutsumi, D. Nishimura, H. Doi, N. Nomura, T. Hanawa, *Difference in surface reactions between titanium and zirconium in Hanks' solution to elucidate mechanism of calcium phosphate formation on titanium using XPS and cathodic polarization*, Mater. Sci. Eng. C-Mater. Biol. Appl., **29** (2009) 1702-1708.

[157] P.A. Dearnley, *A review of metallic, ceramic and surface-treated metals used for bearing surfaces in human joint replacements*, Proc. Inst. Mech. Eng. Part H-J. Eng. Med., **213** (1999) 107-135.

[158] M. Jamesh, T. Narayanan, P.K. Chu, *Thermal oxidation of titanium: Evaluation of corrosion resistance as a function of cooling rate*, Mater. Chem. Phys., **138** (2013) 565-572.

[159] A. Bloyce, P.Y. Qi, H. Dong, T. Bell, *Surface modification of titanium alloys for combined improvements in corrosion and wear resistance*, Surf. Coat. Tech., **107** (1998) 125-132.

[160] D.S.R. Krishna, Y. Sun, *Thermally oxidised rutile-TiO2 coating on stainless steel for tribological properties and corrosion resistance enhancement*, Appl. Surf. Sci., **252** (2005) 1107-1116.

[161] D. Velten, V. Biehl, F. Aubertin, B. Valeske, W. Possart, J. Breme, *Preparation of TiO₂ layers on cp-Ti and Ti6Al4V by thermal and anodic oxidation and by sol-gel coating techniques and their characterization*, J. Biomed. Mater. Res., **59** (2002) 18-28.

[162] H. Guleryuz, H. Cimenoglu, *Effect of thermal oxidation on corrosion and corrosion-wear behaviour of a Ti-6A1-4V alloy*, Biomaterials, **25** (2004) 3325-3333.

[163] S. Kumar, T.S.N.S. Narayanan, S.G.S. Raman, S.K. Seshadri, *Thermal oxidation of CP-Ti: Evaluation of characteristics and corrosion resistance as a function of treatment time*, Mater. Sci. Eng. C-Mater. Biol. Appl., **29** (2009) 1942-1949.

[164] C. Munuera, T.R. Matzelle, N. Kruse, M.F. López, A. Gutiérrez, J.A. Jiménez, C. Ocal, *Surface elastic properties of Ti alloys modified for medical implants: A force spectroscopy study*, Acta Biomater., **3** (2007) 113-119.

[165] M.C. Garcia-Alonso, L. Saldana, G. Valles, J.L. Gonzalez-Carrasco, J. Gonzalez-Cabrero, M.E. Martinez, E. Gil-Garay, L. Munuera, *In vitro corrosion behaviour and osteoblast response of thermally oxidised Ti6Al4V alloy*, Biomaterials, **24** (2003) 19-26.

[166] S.B. Patel, A. Hamlekhan, D. Royhman, A. Butt, J. Yuan, T. Shokuhfar, C. Sukotjo, M.T. Mathew, G. Jursich, C.G. Takoudis, *Enhancing surface characteristics of Ti-6Al-4V for bio-implants using integrated anodization and thermal oxidation*, J. Mater. Chem. B, **2** (2014) 3597-3608.

[167] A. Climent-Font, A. Gutiérrez, J.A. Jiménez, M.F. López, F. Pászti, *Comparative study of the oxide scale thermally grown on titanium alloys by ion beam analysis techniques and scanning electron microscopy*, J. Mater. Res., **23**(2008) 2245-2253.

[168] A.R. Rastkar, T. Bell, *Characterization and tribological performance of oxide layers on a gamma based titanium aluminide*, Wear, **258** (2005) 1616-1624.

References

[169] P. Perez, V.A.C. Haanappel, M.F. Stroosnijder, *The effect of niobium on the oxidation behaviour of titanium in N-2/20% O-2 atmospheres*, Mat. Sci. Eng. A-Struct., **284** (2000) 126-137.

[170] T.K. Roy, R. Balasubramaniam, A. Ghosh, *Effect of nitrogen on the oxidation behavior of Ti3Al-based intermetallic alloys*, Metall. Mater. Trans. A-Phys. Metall. Mater. Sci., **27** (1996) 4003-4010.

[171] H.R. Jiang, M. Hirohasi, Y. Lu, H. Imanari, *Effect of Nb on the high temperature oxidation Ti-(0-50 at.-%)Al*, Scripta Mater., **46** (2002) 639-643.

[172] W.J. Quadakkers, P. Schaaf, N. Zheng, A. Gil, E. Wallura, *Beneficial and detrimental effects of nitrogen on the oxidation behaviour of TiAl-based intermetallics*, Mater. Corros., **48** (1997) 28-34.

[173] T.K. Roy, R. Balasubramaniam, A. Ghosh, *High-temperature oxidation of Ti3Al-based titanium aluminides in oxygen*, Metall. Mater. Trans. A-Phys. Metall. Mater. Sci., **27** (1996) 3993-4002.

[174] S. Kumar, T.S.N.S. Narayanan, S.G.S. Raman, S.K. Seshadri, *Thermal oxidation of CP Ti - An electrochemical and structural characterization*, Mater. Charact., **61** (2010) 589-597.

[175] J.I. Rosales-Leal, M.A. Rodríguez-Valverde, G. Mazzaglia, P.J. Ramón-Torregrosa, L. Díaz-Rodríguez, O. García-Martínez, M. Vallecillo-Capilla, C. Ruiz, M.A. Cabrerizo-Vílchez, *Effect of roughness, wettability and morphology of engineered titanium surfaces on osteoblast-like cell adhesion*, Colloid Surfac A, **365** (2010) 222-229.

[176] J.Y. Martin, Z. Schwartz, T.W. Hummert, D.M. Schraub, J. Simpson, J. Lankford, Jr., D.D. Dean, D.L. Cochran, B.D. Boyan, *Effect of titanium surface roughness on proliferation, differentiation, and protein synthesis of human osteoblast-like cells (MG63)*, J. Biomed. Mater. Res., **29** (1995) 389-401.

[177] J. Cox, *Key values for thermodynamics*, New York: Hemisphere Publishing Co., 1989.

[178] J. Nychka, M. Gentleman, *Implications of wettability in biological materials science*, JOM, **62** (2010) 39-48.

[179] P.F. Gostin, A. Helth, A. Voss, R. Sueptitz, M. Calin, J. Eckert, A. Gebert, *Surface treatment, corrosion behavior, and apatite-forming ability of Ti-45Nb implant alloy*, J. Biomed. Mater. Res., **101B** (2013) 269-278.

List of publications

1. M. Calin, A. Gebert, A.C. Ghinea, P.F. Gostin, S. Abdi, C. Mickel, J. Eckert, *Designing biocompatible Ti-based metallic glasses for implant applications*, Mater. Sci. Eng. C-Mater. Biol. Appl., **33** (2013) 875-883.

2. S. Oswald, P. F. Gostin, A. Helth, S. Abdi, L. Giebeler, H. Wendrock, M. Calin, J. Eckert, A. Gebert, *XPS and AES sputter-depth profiling at surfaces of biocompatible passivated Ti-based alloys: Concentration quantification considering chemical effects*, Surf. Interface Anal., **46** (2014) 683-688.

3. A. Gebert, P.F. Gostin, R. Sueptitz, S. Oswald, S. Abdi, M. Uhlemann, J. Eckert, *Polarization Studies of Zr-Based Bulk Metallic Glasses for Electrochemical Machining*, J. Electrochem. Soc., **161** (2014) E66-E73.

 Parts of this work were published in the following publications:

4. S. Abdi, M.S. Khoshkhoo, O. Shuleshova, M. Bönisch, M. Calin, L. Schultz, J. Eckert, M.D. Baró, J. Sort, A. Gebert, *Effect of Nb addition on microstructure evolution and nanomechanical properties of a glass-forming Ti–Zr–Si alloy*, Intermetallics, **46** (2014) 156-163.

5. S. Abdi, S. Oswald, P.F. Gostin, A. Helth, M. Calin, L. Schultz, J. Eckert, M.D. Baró, J. Sort, A. Gebert, Designing new biocompatible glass-forming $Ti_{75-x}Zr_{10}Nb_xSi_{15}$ (x = 0, 15) alloys: corrosion, passivity and apatite formation, J. Biomed. Mater. Res., Part B, accepted.

Schriftliche Erklärung gemäß Promotionsordnung Fakultät Maschinenwesen / TU Dresden

Hiermit versichere ich, dass ich die vorliegende Arbeit ohne unzulässige Hilfe Dritter und ohne Benutzung anderer als der angegebenen Hilfsmittle angefertigt habe; die aus fremden Quellen direkt oder indirekt übernommenen Gedanken sind als solche kenntliche gemacht.

Weitere Personen waren an der geistigen Herstellung der vorliegenden Arbeit nicht beteiligt. Inbesondere habe ich nicht die Hilfe eines kommerziellen Promotionsberaters in Anspruch genommen. Dritte haben vom mir keine geldwerten Leistungen für Arbeiten erhalten, die in Zusammenhang mit dem Inhalt der vorgelegten Dissertation stehen.

Die Arbeit wurde bisher weder im Inland noch im Ausland in gleicher oder ähnlicher Form einer anderen Prüfungsbehörde vorgelegt und ist auch noch nicht veröffentlicht worden. Die Promotionsordnung wird anerkannt.

Somayeh Abdi